RESURFACING ASTEROIDS & THE CREATION RATE OF ASTEROID PAIRS

A Dissertation

Submitted to the Faculty

of

Purdue University

by

Kevin Graves

In Partial Fulfillment of the

Requirements for the Degree

of

Doctor of Philosophy

December 2018

Purdue University

West Lafayette, Indiana

THE PURDUE UNIVERSITY GRADUATE SCHOOL
STATEMENT OF DISSERTATION APPROVAL

Dr. David Minton, Chair

Department of Earth, Atmospheric, and Planetary Sciences

Dr. Jim Richardson

Planetary Science Institute

Dr. H. Jay Melosh

Department of Earth, Atmospheric, and Planetary Sciences

Dr. Michelle Thompson

Department of Earth, Atmospheric, and Planetary Sciences

Dr. Francesca DeMeo

Massachusetts Institute of Technology, Department of Earth, Atmospheric, and Planetary Sciences

Approved by:

Dr. Darryl Granger

Head of the Graduate Program

ACKNOWLEDGMENTS

I have been very blessed to have so many amazing people who have supported and encouraged me. Before I can mention anyone else, I want to thank my parents, Charles and Kathryn Graves. To my mother, I thank you for always pushing me to work hard and succeed in and out of school. To my father, I thank you for sharing your love for science with me from a young age. I thank Jim Richardson for first taking me on as a graduate student, and helping me through my first year of graduate school. The demonstration of your impact cratering code when I visited Purdue got me excited about the opportunities for computational research in planetary science. I especially thank, my advisor, David Minton for his guidance and advice over these last few years. Thank you for helping me to stand as an independent scientist. I thank all of my fellow students that tackled graduate school with me, and a special thanks to my fellow lab mates in Hampton Hall 2263 for being fun, supportive, and incredibly good looking.

To my baby girl, Rae, your infectious laugh always cheers me up. I love watching you grow and learn new things about the world. To my unborn baby, I can't wait to meet you. Finally, to my wife, Alex, thank you for always being there for me. Thank you for moving to Indiana so that I could chase this dream. I don't think I would have stayed sane without your love and support, and I am eager to take on the future with you.

TABLE OF CONTENTS

Page

LIST OF TABLES

LIST OF FIGURES

Figure Page

Figure Page

SYMBOLS

q	Perihelion Distance (Chapters 2-5)
	Mass ratio between members of asteroid pair (Chapter 6)
Q	Aphelion Distance
H	Absolute Magnitude
D	Diameter
S	Spectral Slope (or gri-slope in Chapter 4)
ω	Rotational Speed
$\dot{\omega}$	Rotational Acceleration
B	Lambertian Scattering Coefficient
G_1	Solar Radiation Constant
ρ	Density
a	Semimajor Axis
	Crack Size (§5.5.2)
e	Eccentricity
i	Inclination
Ω	Longitude of Ascending Node
ω	Argument of Perihelion
f	True Anomaly
R	Radius
C_y	YORP Coefficient
b/a	Aspect Ratio
τ_{SW}	Space Weathering Timescale
$\tau_{Q\rightarrow S}$	Q-type Removal Timescale
P	Orbital Period
R_{pl}	Planetary Radii

τ_R	Resurfacing Timescale
k	Thermal Resurfacing Power-Law Scaling Parameter
$\Delta\sigma_s$	Change in Thermal Stress

ABBREVIATIONS

NEA	Near-Earth Asteroid
MC	Mars Crosser
CC	Carbonaceous Chondrite
OC	Ordinary Chondrite
YORP effect	Yarkovsky-O'Keefe-Radzievskii-Paddack effect
SDSS	Sloan Digital Sky Survey
RMSE	Root Mean Square Error
IMC	Intermediate-source Mars Crosser
MOID	Mean Orbital Intersection Distance
SFD	Size Frequency Distribution

ABSTRACT

Graves, Kevin PhD, Purdue University, December 2018. Resurfacing Asteroids & The Creation Rate of Asteroid Pairs. Major Professor: David Minton.

Many surface and dynamical processes affect the evolution of asteroids in our solar system today. The spectral slopes of S and Q-type asteroids are altered by the weathering of their surfaces due to solar wind interactions and micrometeorite impacts, as well as any processes that work to remove that weathered material. These processes of space weathering and asteroid resurfacing compete with each other to determine the spectral slope of each asteroid, with space weathering raising the spectral slope and resurfacing lowering it. By considering the distribution of spectral slopes with respect to orbital location and size, we can determine which potential resurfacing processes are the most dominant. I show that the distribution of spectral slopes with respect to size is present in all populations of S and Q-type asteroids in the inner solar system, regardless of orbit. I also show that the spectral slopes of S and Q-type Near-Earth Asteroids (NEAs) decrease with decreasing perihelion, but only for perihelia $q \lesssim 0.9$ AU.

By building Monte Carlo and models N-body simulations of asteroids, I test which resurfacing mechanisms are consistent with these trends in spectral slopes. I find that spin-up and failure from the Yarkovsky-O'Keefe-Radzievskii-Paddack (YORP) effect is an important resurfacing mechanism that creates the observed weathering trends with size. I also show that resurfacing asteroids due to close encounters with the terrestrial planets cannot explain the spectral slope vs. perihelion trend at $q \lesssim 0.9$ AU, but that resurfacing asteroids due to thermally induced surface degradation, by assuming a power law relationship between the resurfacing timescale and the solar distance, gives much more consistent results.

I also explore the creation rate of asteroid pairs, which are asteroids that have very similar orbits but are not gravitationally bound. The majority of pairs are formed by YORP spin-up and fission, followed by a separation of the two members. Asteroid pairs are then disassociated over time as their orbits become less similar due to chaos, resonances, and the Yarkovsky effect. I simulate both the formation of asteroid pairs in the inner main belt via YORP and their subsequent disassociation. By comparing the distribution of orbital similarity distances from observations and from our model, I estimate that asteroids fission and create an asteroid pair every $8-13$ YORP cycles, where a YORP cycle is twice the time it takes the YORP effect to change the spin rate of an asteroid from zero to its critical spin rate. I argue that the rate of fissioning via the YORP effect is not substantially limited by any stagnation or stochastic evolution, and that losing mass via rotational fission is much less effective than collisional disruption, even for small asteroids.

1 INTRODUCTION

The first four asteroids (Ceres, Pallas, Juno, and Vesta) were discovered in a relatively short period of time, from 1801-1807. Originally, these new bodies were classified as additional planets that existed between the orbits of Mars and Jupiter. However, with the advent of more accurate star charts aiding observers, many more asteroids were found starting in the 1840s and 1850s. These new observations made it clear that these "asteroids," a Greek term for "star-like," are something unique from the classical planets. Since then, ever improving telescopic observations and other remote sensing techniques have allowed us to better characterize the composition and evolution of these bodies. Asteroids provide clues to the formation of our solar system and record information on its dynamical evolution. They have a very minute but catastrophic chance of causing a impact-induced disaster on Earth, and may even provide valuable resources in the future.

While those reasons alone can make asteroid research a very intriguing and rewarding endeavor, they are not the main reason I have spent the last few years studying them. I have been primarily interested in asteroids because they present a very unique physical system to study. Their small gravity, combined with exterior interactions present in the inner solar system, generate dynamical processes which alter their surfaces, shapes, and sizes. These processes can be very non-intuitive, and only by careful observations, analysis, theory, and sometimes modeling can they be adequately understood.

In the remainder of this section, I provide a brief, simplified history of two types of asteroid observations and their relevent analysis. These observations are the foundation for the original work in this dissertation. First, observations of the colors and spectra of asteroids have made it possible to build taxonomic classifications. By comparing these observations and classifications with meteorites, we can discern the

composition of and modification present on the surface of asteroids. Additionally, asteroid orbits have been found to cluster together, suggesting a common history among the members of the cluster. By measuring the physical and dynamical attributes of these clusters, the formation and evolution of these clusters can be better understood.

1.1 Asteroid Colors and Spectroscopy

The first photometric observations to successfully categorize asteroids were from Wood and Kuiper (1963) and Chapman et al. (1971). The results from these studies were able to identify two broad categories of asteroids, later denoted "S," for their similarity to silicate or stony terrestrial rocks and meteorites, and "C," for their similarity to carbonaceous meteorites (e.g. Chapman 2004; DeMeo et al. 2009). Previous studies conducted observations using broad color filters, but were not successful in categorizing asteroids or making inferences about their compositions (e.g., Watson 1938; Kitamura 1959). In the 1980s, the Eight Color Asteroid Survey (ECAS) (Zellner et al., 1985) conducted the first large scale survey on the colors of asteroids. They observed nearly 600 asteroids in eight filters in the visible wavelengths, which allowed Tholen (1984) to construct the first widely used asteroid taxonomy. Tholen (1984) confirmed that there are two more densely populated spectral classes, denoted as the S-types and C-types. However, he also denoted a total of 14 taxonomic classes to group all observed asteroids.

With the introduction of charged-coupled devices (CCDs) in the 1980s, spectral observations of much fainter asteroids could be conducted at much higher spectral resolutions. This technology lead to the Small Main-belt Asteroid Spectroscopic Surveys (SMASSI and SMASSII) to be conducted in the 1990s (Xu et al., 1995; Bus, 1999). These surveys (especially SMASSII) led to a large set of internally consistent spectral observations in the visible wavelengths that could be used to categorize asteroids into an updated taxonomy including 26 total classes (Bus, 1999; Bus and Binzel, 2002). Most recently, DeMeo et al. (2009) extended the SMASSII taxonomy with the

addition of observations in the near-infrared wavelengths. These new near-infrared observations allowed for a more robust classification scheme, but also slightly altered some of the classifications from the SMASSII taxonomy.

One of the primary goals of the spectral classification of asteroids is to build an understanding of asteroid composition. Before the Galileo spacecraft visited asteroid (951) Gaspra in 1991, the only information available about the composition of asteroids was from spectral observations and meteorites that may have a source body located in the asteroid belt. However, by comparing the spectra of meteorites and asteroids, there is a potential to connect the detailed compositional knowledge of meteorites with different asteroid spectral classes. In a general sense, this comparison is relatively straightforward. For example, carbonaceous chondrite (CC) meteorites have relatively similar spectra to C-type asteroids, ordinary chondrite (OC) meteorites have relatively similar spectra to S-type asteroids, and iron meteorites have relatively similar spectra to the mostly featureless X-type asteroids. Naturally, the conclusion is that each of those meteorites was sourced from that particular asteroid type: CC meteorites from C-type asteroids, OC meteorites from S-type asteroids, and iron meteorites from X-type asteroids.

However, just because asteroids and meteorites have relatively similar spectra, does not mean that they have the same composition. Other types of meteorites such as stony-irons and primitive achondrites also have spectra that are relatively similar to S-type asteroids (Burbine et al., 2002). Additionally, there can be consistent differences between certain types of meteorites and asteroid classes that are otherwise very similar. An important example is that S-type asteroids and OC meteorites have very similar spectral features, with broad absorption bands at 1 and 2 μm and a feature at $\sim$1.3 μm, but nearly all S-type asteroids have relatively higher reflectances at longer wavelengths, or a higher spectral slope, and shallower absorption bands when compared to OC meteorites. This difference is very consistent and has caused many to raise the question if S-type asteroids are the source bodies of OC meteorites, since there are asteroids, called Q-types, which match the spectra of OC meteorites much

more consistently. However, the S-types are the most common type of asteroids that have orbits that cross the Earth, while Q-types are significantly less abundant, and OC meteorites are the most common type of meteorite fall. The relative abundance of both OC meteorite falls and S-type asteroids near the Earth suggests that S-type asteroids must be the source bodies of OC meteorites. These two seemingly contradictory points of evidence has been called the "S-type Conundrum" (Chapman, 2004).

Since the 1980s, a few solutions to this conundrum have been suggested. In the population of near-Earth Asteroids (NEAs), defined as those that have a perihelion $q \leq 1.3$ and aphelion $Q \geq 0.984$ (Rabinowitz, 1994), there is a significant fraction of Q-type asteroids (DeMeo et al., 2014). Some studies, such as Bell et al. (1989) and Gaffey (1993) suggested that the Q-type asteroids could be the sole progenitor of OC meteorites, and that dynamical processes could be preferentially delivering material from these types of asteroids to the Earth. However, Gaffey (1993) also showed that a fraction of S-type asteroids, which he denoted as S(IV), had the correct mineralogy to be identical to OC meteorites by closely investigating their absorption bands, even though the spectral slopes and absorption band depths of these asteroids were still different from OC meteorites. This observation of a similar minerology between S(IV) asteroids and OC meteorites led others to consider a surface modification process that could alter the spectrum of an asteroid with an OC meteorite composition to that of an S-type asteroid.

A surface modification process occurring on an airless body, such as the one suggested for S-type asteroids, is referred to as "space weathering." Lunar soils returned from the Apollo missions showed different optical properties compared to pristine lunar rocks (e.g. Fig. 1 in Chapman 2004). These optical differences resulted from the inclusion of nanophase ($\sim$ 10 nm) metallic particles in the soils that were not present in the pristine rocks. Processes such as micrometeorite impacts and solar wind irradiation can create these particles (e.g. Hapke et al. 1975; Hapke 2001; Sasaki et al. 2001), and alter the spectrum of the surface of the moon. With the

work of Gaffey (1993), this process of space weathering was more closely studied with respect to S-type asteroids. There were significant concerns as to whether lunar-like space weathering could to occur on smaller asteroids (Chapman, 1996), but through extensive laboratory work in the 1990s-2000s, more complete surveys of asteroids, and spacecraft visits to a few S-type asteroids, the process of space weathering on S-type asteroids is now generally accepted.

I will discuss the background of space weathering on S and Q-type asteroids in more depth in Chapter 2, but an important conclusion from many of these studies is that space weathering on the surface of an asteroid with an OC meteorite composition is a relatively efficient process. The lack of observed Q-type asteroids, especially in the main belt, compared to the general abundance of S-type asteroids also argues for an efficient space weathering rate. However, Q-type asteroids do exist and are relatively common in the NEAs, which raises the question, what causes Q-type asteroids to have a surface that is not altered by space weathering? As the process of space weathering only affects the upper surface of an asteroid, any process that can remove or bury that space weathered veneer can effectively change an S-type asteroid into a Q-type asteroid. In Chapters 2-5, I explore, model, and discuss the process of resurfacing S-type asteroids to create Q-types.

1.2 Asteroid Clustering

Another important set of observations that can give important insights into asteroid evolution is that the orbits of many asteroids cluster together even though they are not gravitationally bound. Hirayama (1918) first reported evidence that there were at least five clusters of asteroids in the main belt that could not be due to random chance. These clusters are known as asteroid families and are named after the asteroid in the cluster that was discovered first. Hirayama (1918) identified the families: Eos, Themis, Koronis, Flora, and Maria. He concluded that these asteroid families resulted from a single asteroid that was broken up some time in the past.

Since 1918, further observations, theoretical calculations, and numerical simulations have all verified that the prominent asteroid families in the main belt are formed from a catastrophic breakup of a single asteroid (for a more extensive review, see Bendjoya and Zappalà 2002).

More recently, Vokrouhlický and Nesvorný (2008) found that certain pairs of asteroids could also have very similar orbits that cannot be attributed to random chance. These asteroids are also not gravitationally bound together, but their orbits are much more similar than those between members of asteroid families, suggesting that they formed from a very recent breakup of an asteroid into two parts. These asteroid pairs are also only seen between smaller ($D \lesssim 5$ km) asteroids. Vokrouhlický and Nesvorný (2008) hypothesized a few different formation mechanisms. Like asteroid families, they could be formed from a catastrophic collision which resulted in only two members being large enough to be observed. Another process, known as the Yarkovsky-O'Keefe-Radzievskii-Paddack (YORP) effect, occurs when an irregularly shaped asteroid is heated by the Sun and radiates that heat away imparting a torque on body (Rubincam, 2000; Bottke et al., 2006) The YORP effect can be extremely effective at changing the spin rate of small asteroids and can even cause them to fission when spun up to very high spin rates (Walsh and Richardson, 2008). Pravec et al. (2010) showed that rotational fission via the YORP effect is the most consistent explanation for the creation of asteroid pairs. I give a more detailed background of the studies of Vokrouhlický and Nesvorný (2008) and Pravec et al. (2010) in Chapter 6.

The YORP effect is a very important evolutionary process for small asteroids. Besides being a formation mechanism for asteroid pairs, Walsh and Richardson (2008) also argued that it is the primary formation mechanism for binary asteroids – two gravitationally bound asteroids. Other models have also used the YORP effect to account for the spin rate distribution of NEAs (Rossi et al., 2009) and main belt asteroids (Marzari et al., 2011), as well as the size frequency distribution of the main belt at small sizes (Jacobson and Morbidelli, 2014). I also argue for YORP-induced spin up and surface failure as an effective resurfacing mechanism for S-type asteroids

in Chapter 4. However, the YORP effect can be very difficult to model. The evolution of an asteroid's spin at very low and very high spin rates is not well understood (e.g., Vokrouhlický et al. 2007; Bottke et al. 2015). Also, some studies have argued that the YORP effect will cause a Stochastic evolution of an asteroid's spin rate and cause the YORP effect to stagnate (Statler, 2009; Cotto-Figueroa et al., 2015).

In Chapter 6, I use Pravec et al. (2010)'s conclusion that YORP effect is creating asteroid pairs as well as the observations of asteroid pairs in the inner main belt to estimate the rate at which asteroid pairs are created. A measure of the creation rate of asteroid pairs can then place constraints on the importance and strength of the YORP effect on small asteroids.

2 WEATHERING AND REFRESHING ASTEROID SURFACES

Portions of the content of this chapter were published in the journal Icarus as Graves et al. (2018).

The most common type of meteorite falls are ordinary chondrites (e.g., Chapman 1996). Ordinary Chondrites (OCs) are stony meteorites that were never heated enough to cause differentiation. They have very similar spectral signatures to S-type asteroids, which are the most common type of Near-Earth Asteroid (Binzel et al., 2004; Carry et al., 2016). Near-Earth Asteroids (NEAs) are defined as those that have a perihelion $q \leq 1.3$ and aphelion $Q \geq 0.984$ (Rabinowitz, 1994). They both show absorption bands at 1 and 2 μm, have a feature at $\sim$1.3 μm, and exhibit the same general spectral shape (DeMeo et al., 2009). Many S-type asteroids are also mineralogically very similar, if not identical, to OC meteorites (Gaffey, 1993; Reddy et al., 2015; Brunetto et al., 2015). However, the spectra of S-type asteroids and OC meteorites are not identical. S-type asteroids typically have a higher relative reflectance at longer wavelengths through the visible and near infrared (known as a spectral slope) in the visible and near-infrared wavelengths, and have shallower absorption band depths compared to OC meteorites (Gaffey, 1976; Bus, 1999; DeMeo et al., 2009). S-type asteroids also typically have lower albedos than OC meteorites (Chapman, 2004). Multiple studies have shown that S-type asteroids are almost certainly the progenitors of many OC meteorites, and the differences in spectral characteristics can be due to a process known as "space weathering" (Chapman, 2004; Nakamura et al., 2011; Brunetto et al., 2015).

Space weathering is a broad term used to describe the alteration of the optical properties of material on a surface of an airless body, such as the Moon and asteroids (Brunetto et al., 2015). It is the generally accepted mechanism to explain the differences between the spectral and albedo properties of S-type asteroids and OC

meteorites (e.g., Chapman 2004; Brunetto et al. 2015). Space weathering includes processes such as ion irradiation from the solar wind and micrometeorite impacts (Brunetto et al., 2015), and can change the spectrum of an asteroid with an OC composition to that of an S-type asteroid by increasing the spectral slope and decreasing its absorption band depths. These spectral changes have been verified by experiments (Sasaki et al., 2001; Clark et al., 2002; Brunetto and Strazzulla, 2005; Strazzulla et al., 2005; Brunetto et al., 2006; Loeffler et al., 2009), remote sensing (Vernazza et al., 2009), and a sample return from an S-type asteroid, (25143) Itokawa (Noguchi et al., 2011). Additionally, space weathering can darken the surface of a asteroid with an OC composition, creating the albedo differences between OC meteorites and S-type asteroids (Brunetto et al., 2015).

The presence of Q-type asteroids, with spectra consistent to those of OC meteorites (Bus, 1999; DeMeo et al., 2009), suggests that space weathering has not affected the surfaces of these asteroids. If space weathering alters the surfaces of these types of asteroids, but there are Q-type asteroids that do not show any sign of space weathering, there must either be a compositional or physical reason keeping these asteroids from weathering or additional processes that are resurfacing these asteroids.

Hapke (2001) argued for a selective space weathering effect, where the solar wind could not weather a surface with an OC composition in the absence of fine regolith, potentially giving smaller asteroids, with less fine regolith, a less weathered spectrum. However, observations of S-type asteroid (25143) Itokawa showed highly weathered regions with very little fine regolith (Ishiguro et al., 2007). A better explanation for the presence of Q-type asteroids is that they have recently been resurfaced and have not yet had time for space weathering to create any alteration of their surface. An asteroid is resurfaced if the upper veneer of material that can be altered by space weathering agents (on the order of 10 nm; Noguchi et al. 2011) is removed or buried by unweathered material.

2.1 Weathered and Unweathered Asteroids

To constrain the prevalence of any resurfacing processes, we must first understand the distribution of weathered, S-type asteroids and unweathered, Q-type asteroids. S-type asteroids are the most common type of NEA, comprising about 40% of the total population, and are also the second most common type of asteroid, behind C-type asteroids (DeMeo and Carry, 2013), another type of primitive asteroids that are linked to carbonaceous chondrites. S-type asteroids are more common in the inner parts of the Main Asteroid Belt, and become increasingly less common farther away from the Sun (DeMeo and Carry, 2013). Q-type asteroids have been primarily found in the NEA region where they comprise about 10% of the total population (Binzel et al., 2004; Binzel et al., 2010; DeMeo et al., 2014; Carry et al., 2016), but they have also been found in the small members of multiple asteroid families and clusters (Mothé-Diniz and Nesvorný, 2008; Rivkin et al., 2011; Thomas et al., 2011, 2012), and in the members of recently separated asteroid pairs (Polishook et al., 2014). Marchi et al. (2006a) showed that the spectral slope decreased from a higher average S-type slope to a lower average Q-type slope with decreasing perihelion in the NEA and Mars Crosser (MC) regions. DeMeo et al. (2014) also found a higher percentage of Q-type asteroids at lower perihelion. As Q-type asteroids typically have lower spectral slopes than S-types, their findings correlate with those of Marchi et al. (2006a). Additionally, Binzel et al. (2004) noted that the average spectral slope of NEAs and MCs decreased with decreasing size, starting at a diameter of $\sim$5 km. Carry et al. (2016) and Thomas et al. (2012) found a similar size trend using data from the Sloan Digital Sky Survey (SDSS) in the NEAs and MCs and the Koronis family, respectively. Lin et al. (2015) conducted a multicolor survey and found that the ratio of sub-kilometer Q-type to S-type asteroids in the main belt is $<$0.05. However, both Carvano et al. (2010) and DeMeo and Carry (2013) classified the asteroids in the main belt that were observed by the SDSS, and Carvano et al. (2010) found about four times more Q-types than DeMeo and Carry (2013) at sizes $\lesssim$5 km. Surveys like the SDSS and that of Lin

et al. (2015) have only limited spectral resolution, and, more importantly, limited spectral coverage. As many S and Q-type asteroids can be degenerate in the visible wavelengths, observations in both the near infrared and the visible wavelengths are needed to accurately determine the boundary between the taxonomic classes. Due to the limited observations of small main belt asteroids in both the visible and the near infrared, the ratio of Q to S-types in the main belt is not fully understood.

A number of these studies investigated a trend in the spectral slopes of both S-type and Q-type asteroids, and suggest that there is a spectrum between a fully unweathered, recently resurfaced, Q-type asteroid and a S-type asteroid that has been fully saturated by space weathering. In the remainder of this dissertation, we primarily use the spectral slope as the primary tool to determine the amount that space weathering has affected the asteroid. By making this choice, we avoid using the binary distinction between an S-type and Q-type asteroid to determine if an asteroid is affected by space weathering, and it allows us to quantify the degree of weathering. An example of why it is important to consider the degree of weathering can be seen from the results of Mothé-Diniz et al. (2010). They found that the spectra of a subset of S-type asteroids match the spectra of OC meteorites, suggesting that there are S-type asteroids that are relatively unweathered. However, the asteroids that they considered have lower spectral slopes than the core S-type asteroids. A binary classification would incorrectly mark these asteroids as completely weathered, but by considering the spectral slope we can more accurately represent the weathering state of these asteroids.

Different resurfacing mechanisms would create different observable trends in the spectral slopes of S and Q-type asteroids. By quantifying those trends, we can test the effectiveness of potential mechanisms. From the studies cited above, we can conclude that the distribution of the spectral slopes of S and Q-type asteroids has been shown to have two primary trends: (1) the average spectral slope decreases with decreasing size, and (2) the average spectral slope decreases with decreasing perihelion in the NEA region. We analyze these trends in detail in Chapter 3, but because any asteroid

with a low spectral slope can be classified in one of these two trends, any potential resurfacing mechanism would need to explain at least one trend.

2.2 Space Weathering and Resurfacing Mechanisms

The presence and distribution of Q-type asteroids and less weathered S-type asteroids suggests that there is an ongoing cycle of space weathering and resurfacing. By constraining the timescale of the rate of spectral (or albedo) change from space weathering and the timescale of any potential mechanisms that could resurface asteroids, we can help constrain which potential resurfacing mechanisms may be prevalent.

The timescale for space weathering of an asteroid with an OC composition has been estimated from laboratory experiments to take anywhere from $\sim$ 10 kyr–100 Myr. From heavy ion irradiation experiments, Strazzulla et al. (2005) estimated a timescale for the solar wind to raise the spectral slope of an OC to something similar to an S-type asteroid to be $\sim$ 10 kyr–1 Myr in the NEA region. Loeffler et al. (2009) conducted similar experiments with keV He ions and found a timescale of less than 10 kyr at 1 AU. Sasaki et al. (2001) estimated the timescale for micrometeorite impacts to raise the spectral slope of an asteroid with OC composition to a fully weathered S-type asteroid to be about 100 Myr in the NEA region. Vernazza et al. (2009) matched the ages and spectra of recently created asteroid clusters to the weathering timescales in Strazzulla et al. (2005) to claim that the solar wind is raising the spectral slope of asteroids in the main belt at timescales $\lesssim$ 1 Myr, and that micrometeorite impacts continue to slightly increase their spectral slopes through 100 Myr. Furthermore, Keller and Berger (2014) observed solar flare particle tracks from regolith particles that suggested an exposure age of the upper surface may be as short as 1–10 kyr. The rapid weathering timescales of irradiation experiments ($\sim$ 1 kyr–1 Myr) compared to micrometeorite experiments ($\sim$ 100 Myr) have led to the consensus that the solar wind is the primary space weathering mechanism, especially for relatively unweath-

ered asteroids, such as Q-types (Marchi et al., 2006b; Vernazza et al., 2009; Brunetto et al., 2015).

A space weathering timescale of $\sim$ 10 kyr – 1 Myr places an important constraint on viable resurfacing mechanisms. First, it suggests that any resurfacing process must, on average, reset a single NEA in a timescale comparable to that of space weathering, due to the relatively high ratio of Q-type to S-type asteroids ($\sim 1:4$). Additionally, we can estimate the average resurfacing time of many potential mechanisms, and compare them to this space weathering timescale.

Possibly the most straightforward resurfacing mechanism would be catastrophic collisions, where asteroids are broken apart into many fragments with the largest being about half of the size of the original asteroid. All asteroids created by such a collision would certainly have the upper-most surface stripped away, leaving a fully unweathered, Q-type asteroid. Willman et al. (2008); Willman et al. (2010) and Willman and Jedicke (2011) calculated a space weathering timescale by assuming that asteroids were resurfaced only after their last catastrophic disruption. Using the ages of asteroid families and the estimated age since last catastrophic disruption (Bottke et al., 2005), they estimated a weathering timescale of 100 Myr–1 Gyr. This timescale for the destruction of asteroids into smaller unweathered fragments is 2-5 orders of magnitude longer than the ion irradiation experiments simulating the solar wind, implying that disruptive collisions cannot be the primary resurfacing mechanism for creating Q-type asteroids because they occur far too infrequently.

Smaller, non-disruptive, collisions can also work to resurface asteroids. The physical excavation and depositing of ejecta, known as impact gardening, will expose unweathered material, lowering the entire spectral slope of the asteroid (Paolicchi et al., 2009; Marchi et al., 2012). Additionally, post-impact seismic shaking could overturn an asteroid's surface and also expose unweathered material (Richardson et al., 2005; Rivkin et al., 2011; Shestopalov et al., 2013). Unfortunately, both of these processes are difficult to model quantitatively. For example, see Section 3 in Marchi et al. (2012) for a discussion of the uncertainties in modeling impact gardening. However, Rivkin

et al. (2011) used order-of-magnitude arguments to suggest that post-impact seismic shaking is consistent with the existence and distribution of less weathered asteroids found in the Koronis family for a space weathering timescale of ~ 1 Myr. I did not test this mechanism in my dissertation work, but it is a potential explanation for the decrease in spectral slopes with decreasing size.

Nesvorný et al. (2005) proposed that asteroids could instead be resurfaced from the movement of surface grains due to tidal forces during a close encounter with a terrestrial planet. For an asteroid to be resurfaced by a close encounter with a planet, it must pass very close to the planet. The exact closest approach distance needed to cause a resurfacing event is difficult to determine as it depends on the speed of the asteroid with respect to the planet, the rate of rotation, the spin-pole direction compared to the planet-asteroid plane, and the composition and structure of the asteroid's surface (e.g., Richardson 1998). However, Richardson (1998) showed that at very small distances ($\lesssim 1.5$ planetary radii), nearly all encountering asteroids will break apart. It is reasonable to then assume that a slightly more distant encounter could only resurface (and not disrupt) the asteroid. Many additional studies have further explored this mechanism (Marchi et al., 2006a; Binzel et al., 2010; DeMeo et al., 2014; Carry et al., 2016), and Nesvorný et al. (2010) found that if a close encounter with a distance of 5 planetary radii is sufficient to cause a complete resurfacing of an asteroid, then resurfacing from close encounters could generate the number of Q-type asteroids in the NEA region for a space weathering timescale of 1 Myr. Because most asteroids with low perihelia still have large aphelia, and therefore cross the orbits of all of the terrestrial planets, tidal effects from close encounters with the terrestrial planets could potentially create the decrease in spectral slopes with decreasing perihelion (Marchi et al., 2006a). In Chapter 5, we show that for any reasonable combination of the minimum encounter distance needed for a complete resurfacing and the space weathering timescale, close encounters cannot explain the decrease in spectral slopes with decreasing perihelion.

The increase in spin rate of an asteroid due to irregular radiative torques, known as the Yarkovsky-O'Keefe-Radzievskii-Paddack (YORP) effect, can increase an asteroid's spin rate to the point where it fissions or experiences surface or internal failure (Bottke et al., 2006; Walsh et al., 2008; Hirabayashi, 2015). A fissioning event or a large-scale surface failure could disrupt, cover, or overturn much of the surface of an asteroid resurfacing it and lowering it spectral slope. Additionally, the YORP effect is stronger for asteroids that are either closer to the Sun or smaller (e.g., Scheeres 2007). In Chapter 4, we investigate resurfacing from YORP-induced rotational failure or fission and show that it can create the decrease in spectral slope with decreasing size, but should not create any trends in spectral slope with respect to orbital location (i.e., perihelion).

Finally, thermal cycling and fatigue can cause surface breakdown of an asteroid and remove, destroy, or cover any space weathered particles (Delbo et al., 2014). This process of breaking down boulders and grains due to thermal cycling has been shown to be effective in terrestrial, Martian, and anhydrous environments (e.g., Eppes et al. 2016; Viles et al. 2010; Delbo et al. 2014), and is expected to also occur in vacuum or low pressure environments such as on the surfaces of comets and asteroids (Thirumalai and Demou, 1970; Dombard et al., 2010; Molaro et al., 2015; Molaro et al., 2017; Auger et al., 2018). Additionally, the magnitude of temperature change increases with decreasing perihelion, increasing the rate of thermal fatigue and degradation. This fracture and degradation can expose underlying unweathered material and resurface the asteroid if either the fractured material is removed from the asteroid, or if a significant amount of the surface material is overturned. Although the timescale of thermally induced surface degradation is not well constrained, if it causes resurfacing at moderately low perihelia, it can create the decrease in spectral slopes with decreasing perihelion. In Chapter 5, we show that thermally induced surface degradation is consistent with the spectral slope vs. perihelion distribution for a reasonable range of parameters.

In summary, the resurfacing mechanisms of close encounters with the terrestrial planets, impact gardening, collisions and subsequent seismic shaking, and YORP-driven spin-up and failure could all potentially resurface asteroids at a rate that can match the number of observed unweathered asteroids for a space weathering timescale of $\sim$ 10 kyr – 1 Myr. Thus, it is crucial to consider the spectral slope distribution with respect to size and perihelion when determining which mechanisms are the most effective. In the next chapter, I quantify the spectral slope vs. size and the spectral slope vs. perihelion distributions, and in Chapters 4 and 5, I use those distributions as the primary constraint when modeling the resurfacing processes of YORP-induced spin-up and failure (Chapter 4), tidal effects from close encounters with the terrestrial planets (Chapter 5), and thermally-induced surface degradation (Chapter 5).

3 TRENDS IN THE WEATHERING STATES OF ASTEROIDS

Portions of the content of this chapter were published in the journal Icarus as Graves et al. (2018).

As mentioned in the previous chapter, there are two primary trends in the spectral slopes of S and Q-type asteroids:

1. The average spectral slopes decrease with decreasing size below a diameter of ~ 5 km, and

2. The average spectral slopes decrease with decreasing perihelion in the NEA region.

In this chapter, I quantify these relationships. By using data generated from the Sloan Digital Sky Survey (SDSS), I show that the correlation between lower spectral slopes and a smaller asteroid size is pervasive throughout the inner solar system. Previously, the trend of lower spectral slopes correlating with smaller sizes was constrained to investigations in the NEA and Mars Crosser (MC) region (Binzel et al., 2004; Carry et al., 2016), or the Koronis family in the Main Belt (Thomas et al., 2012). I also re-examine the spectral slope vs. perihelion trend using the same data as in Marchi et al. (2006a). Instead of a steady decrease in average spectral slope with decreasing perihelion from the MC region and throughout the NEA region as found in Marchi et al. (2006a), I found that there is only a significant trend in decreasing average spectral slope with decreasing perihelion for $q \lesssim 0.9$ AU.

3.1 Orbitally Independent gri-Slope vs. Size Trend

The Sloan Digital Sky Survey is a large photometric and spectroscopic survey that was primarily designed to observe extragalactic objects (York et al., 2000). The

SDSS also detected moving objects, such as asteroids in the main belt, NEA and MC regions (Ivezić et al., 2001; Carry et al., 2016). The SDSS takes observations in five photometric bands, u′, g′, r′, i′, and z′, with wavelengths from 0.3 to 1 μm (Ivezić et al., 2001). These five bands have been used to sort asteroids into broad taxonomic classes (Carvano et al., 2010; DeMeo and Carry, 2013; Carry et al., 2016). In this study, we use the set of SDSS data that was processed and classified by DeMeo and Carry (2013) and Carry et al. (2016).

Classifying asteroids as either Q-types or S-types is difficult without both visible and near-infrared spectral data. Additionally, the majority of Sk and Sq-type asteroids in the main belt are good matches to some OC meteorites (Mothé-Diniz et al., 2010). A resurfaced asteroid with this composition need not be classified as a Q-type. To avoid these difficulties, we only use the slope of the linear regression through the g′, r′, and i′ filters, known as the gri-slope (DeMeo and Carry, 2013), as a parameter to describe the amount of weathering that has accumulated on the surface. The gri-slope is analogous to spectral slope, as the g′, r′, and i′ filters cover approximately $0.4 - 0.8$ μm (Ivezić et al., 2001), and the spectral slope is taken over the range $0.44 - 0.92$ μm (Bus, 1999). In nearly all cases, a higher gri-slope corresponds to a higher spectral slope and vice versa.

In Fig. 3.1, we plot the distribution of the gri-slopes of all observed main belt S and Q-type asteroids as a function of their size. We show the linear regression through all asteroids with an absolute magnitude H $>$ 13 (approximately diameters D $<$ 5 km). Choosing the cutoff of D $<$ 5 km is consistent with the change in the trend of gri-slopes vs. size seen in the Koronis family (Thomas et al., 2012), as well as the maximum size of detected Q-types (Binzel et al., 2004). Also, the slope of the linear regression of the asteroids with a magnitude of $H < 13$ is statistically insignificant. This suggests that a resurfacing mechanism is only present at sizes H $\gtrsim$ 13. We also include the linear regression of the NEA and MC S and Q-type asteroids generated from Fig. 7 of Carry et al. (2016).

Both the main belt and the NEA and MC asteroids have nearly the same trend of decreasing average gri-slopes with decreasing size. The slopes of the linear fits are $-0.42 \pm 0.04\,\%/100$ nm/mag and $-0.36 \pm 0.17\,\%/100$ nm/mag for the main belt asteroids and NEA and MC asteroids, respectively. There is also a vertical offset between the linear regression of the main belt and NEA and MC data of $0.6 \pm 0.3\,\%/100$ nm/mag. At all sizes, NEAs and MCs have, on average, slightly lower gri-slopes than their main belt counterparts, but there is a similar trend in both populations.

Composition can also affect the observed weathering state, and thus gri-slope, of individual asteroids (Sasaki et al., 2002; Marchi et al., 2005). The fraction of olivine to pyroxene can cause different maximum (minimum) gri-slopes for fully weathered (unweathered) objects as well as different weathering rates. By considering the entire main belt, we effectively ignore compositional effects. To remove any effect of composition, we can restrict ourselves to a single asteroid family.

The Flora family is a good test population to investigate the resurfacing of asteroids. It is an old family (Dykhuis et al., 2014), so the weathering states of all family members should not be greatly affected by the initial family-forming collision. Its location in the inner belt allows smaller asteroids to be detected by the SDSS. The composition of the Flora family is expected to be dominated more by olivine than pyroxene, potentially allowing for a greater range in gri-slopes between weathered and unweathered surfaces (Vernazza et al., 2009). Finally, asteroids in the Flora family do not cross the orbits of the terrestrial planets, avoiding any need to disentangle the effects of resurfacing at low perihelia.

In Fig. 3.2, we plot the gri-slope vs. size for the members of the Flora family using the asteroid family catalog of Nesvorný et al. (2015). We again plot the linear regression through all asteroids with a magnitude $H > 13$. We also include the running mean of the gri-slopes, with a box size of 15 and the uncertainty of the mean values at a 95% confidence level. There is a steeper gri-slope vs. size trend in the Flora family when compared to the entire main belt. The slope of the linear regression

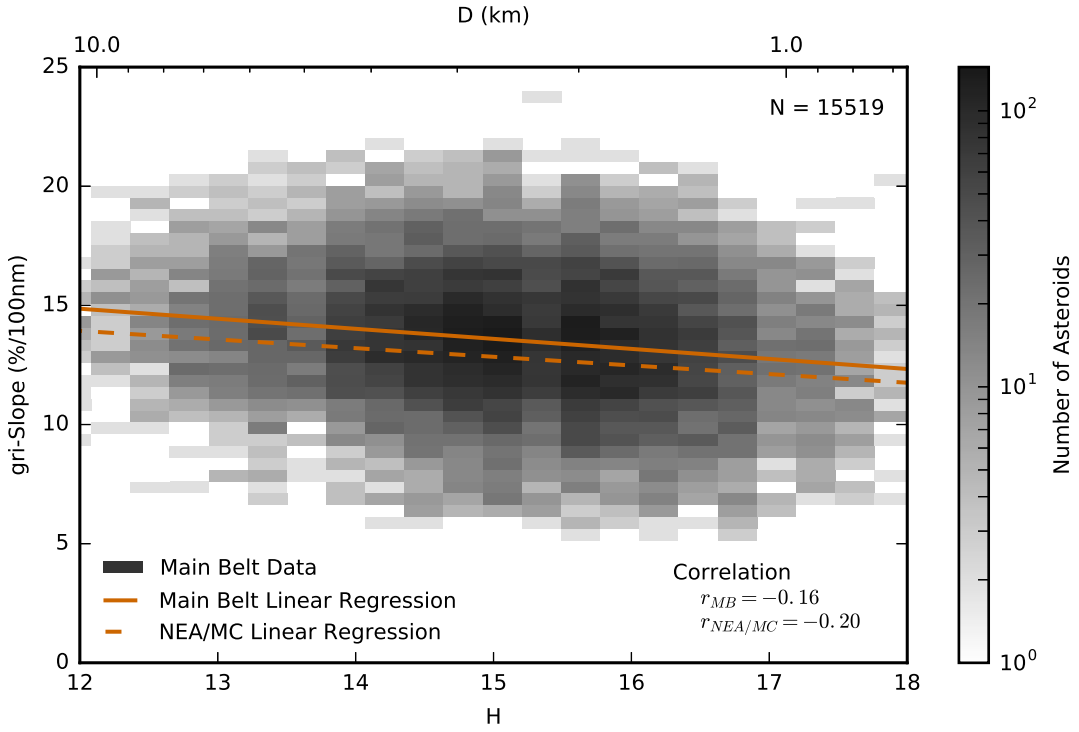

Figure 3.1. The distribution of gri-slope vs. absolute magnitude of S and Q-type asteroids in the main belt from the SDSS. The solid line is the linear regression through the main belt asteroids with absolute magnitudes H > 13, and the dashed line is the linear regression through the NEA and MC data from Carry et al. (2016) (data not shown). The slopes of the linear regressions are -0.42 ± 0.04 %/100 nm/mag and -0.36 ± 0.17 %/100 nm/mag for the main belt asteroids and NEA and MC asteroids, respectively, showing a statistically significant decrease in the average gri-slope of asteroids smaller than H=13 for both populations.

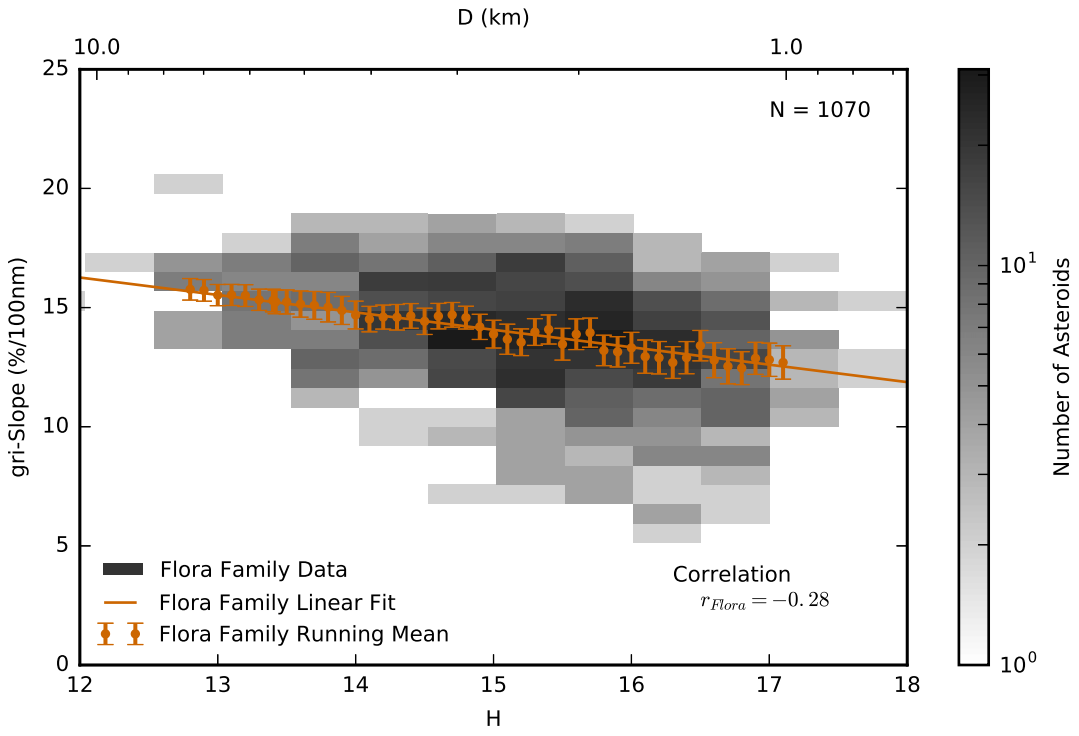

Figure 3.2. Same as Fig. 3.1, except only considering asteroids in the Flora family. The solid line is the linear regression through the Flora family asteroids with absolute magnitudes H $>$ 13. The points and error bars are the running mean of the gri-slope with a box size of 15 and the uncertainty of the mean values at a 95% confidence level. The slope of the linear regression is -0.73 ± 0.15 %/100 nm/mag, showing a significant decrease in the average gri-slope of asteroids smaller than H = 13 that is steeper than the trends in Fig. 3.1.

of the gri-slopes vs. size for the Flora family is -0.73 ± 0.15 %/100 nm/mag. The steeper trend may be due to the large olivine content of the Flora family asteroids (Vernazza et al., 2009). We only use the data from the Flora family to compare to our modeling results in Chapter 4, §4.1 and §4.2

We claim that any results from the restricted analysis of the Flora family are generally applicable to the entire inner solar system due to the similarity of the NEA and MC, and main belt trends shown in Fig. 3.1. The MCs, which are the majority

of asteroids observed in Carry et al. (2016), are sourced from weak resonances all throughout the main belt (Morbidelli and Nesvorný, 1999). Thus, we can expect the MCs to have the same compositional trends as the main belt. We also find qualitatively similar gri-slope vs. size trends if we consider the NEAs or the inner, middle, or outer main belt asteroids alone.

YORP spin-up and failure coupled with space weathering from the solar wind qualitatively fits the data in Figs. 3.1 and 3.2. The YORP effect and exposure from the solar wind scale identically with orbit (see Chapter 4, §4.1 for a further discussion), but only YORP will work increasingly effectively to resurface asteroids at smaller sizes. Additionally, the large sensitivity of the YORP effect from the exact placement of boulders and craters on the surface can cause a large range of possible rotational acceleration rates (Statler, 2009), giving a spread in the timescales needed for an asteroid of a particular size to spin up to the point of failure. A spread in timescales for an asteroid to fail and resurface would also generate a spread in the gri-slopes as seen in Figs. 3.1 and 3.2. In Chapter 4, we develop a model to test the parameters needed for YORP to create the gri-slope vs. size trend seen in Fig. 3.2.

3.2 Distribution of Spectral Slopes and Perihelion

In order to properly test potential resurfacing mechanisms at low perihelion, we must first understand the distribution of spectral slopes there. In this section, we find that there is a substantial observational bias in the observed spectral slopes, especially in the Mars Crosser (MC) region, and, after removing that bias, we find no evidence of a perihelion trend for perihelia $q \gtrsim 0.9$ AU.

In Fig. 3.3, we plot the NEA and MC spectral slopes against perihelion, similarly to Fig. 1 in Marchi et al. (2006a). The size of each circle corresponds to the asteroid's diameter, assuming a constant albedo for all asteroids. We also include a windowed moving average of the spectral slopes, where each average spectral slope is calculated by taking the average of all spectral slopes of asteroids with perihelion that are within

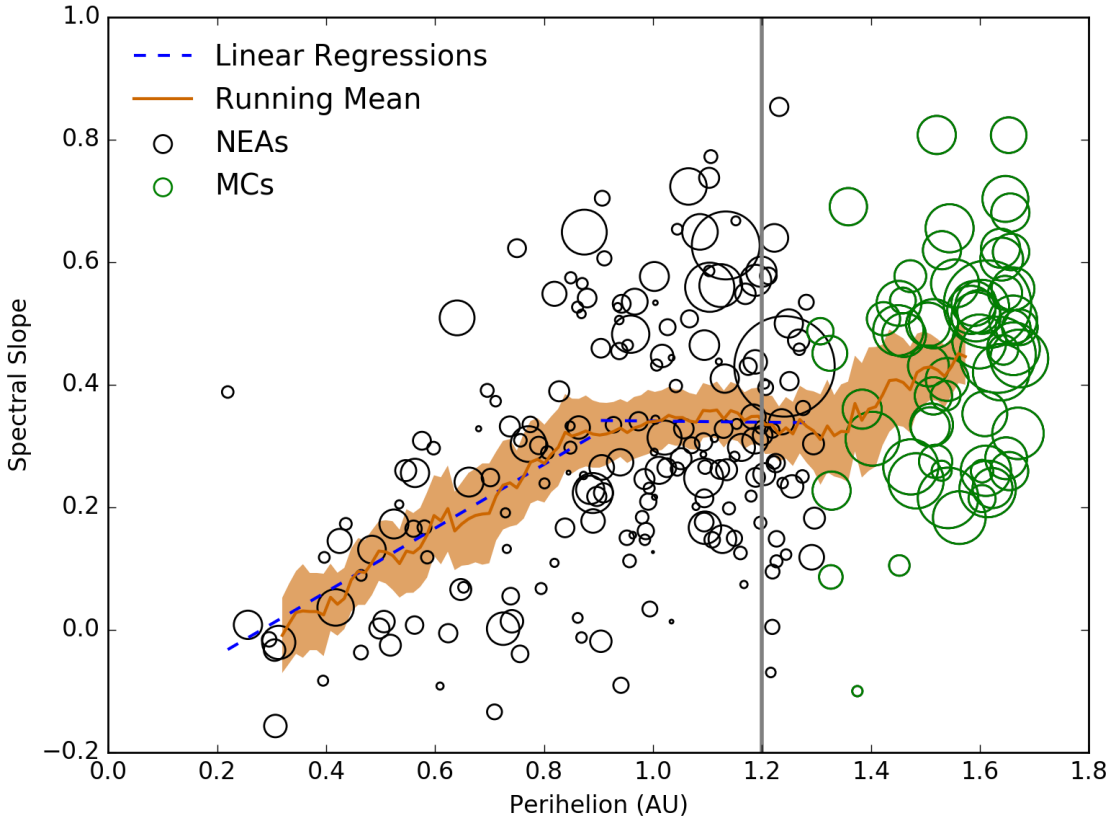

Figure 3.3. The distribution of spectral slope vs. perihelion of S and Q-type asteroids in the NEA and MC regions using the data in Binzel et al. (2004); Lazzarin et al. (2004, 2005). NEAs are drawn as black circles and MCs as green circles. The size of the circle corresponds to the diameter of the asteroid. The dashed blue line is the linear regression through the asteroids, the solid orange line and shaded region is a windowed moving average, where each average spectral slope is calculated by taking the average of all spectral slopes of asteroids with perihelion that are within ±0.1 AU, and its uncertainty at a 95% confidence level. This figure is very similar to Fig. 1 from Marchi et al. (2006a), except that we use a windowed moving average instead of one that uses a set number of points to create the average. We denote the perihelion above which MCs affect the windowed moving average by a vertical gray line. The average spectral slope decreases with decreasing perihelion. However, there is a plateau from $q \approx 0.9 - 1.3$ of nearly constant average spectral slopes, before increasing again in the MC region.

± 0.1 AU. The shaded region is the uncertainty of the average spectral slopes at a 95% confidence level. Overall, the average spectral slope decreases with decreasing perihelion from the MCs through the NEAs. The slope of the linear regression of the spectral slopes vs. perihelion is 0.27 ± 0.06 %/μm/AU for the entire population. However, by using the windowed moving average instead of a traditional moving average, where each average spectral slope is calculated with the same number of points equally sampled from above and below the asteroid's perihelion, we do not find a steady decrease in the average spectral slope with decreasing perihelion, as was found in Marchi et al. (2006a). Instead, we find that the average spectral slope only has a significant trend with perihelia of $q \lesssim 0.9$ AU and $q \gtrsim 1.3$ AU, with the slope of the linear regression through the spectral slopes of asteroids with 0.9 AU $\leq q < 1.3$ AU is 0.01 ± 0.26 %/μm/AU. Additionally, by using a windowed moving average, we better represent the dependence of the asteroids' spectral slopes on perihelion because point-based moving averages use varying perihelion windows based on the number of observations at different perihelia (e.g. larger windows at low perihelion where less asteroids are observed). We also include a gray vertical line at a perihelion, above which the running mean is affected by the spectral slopes of MCs ($q = 1.2$ AU).

Next, we plot the spectral slopes against their absolute magnitude in Fig. 3.4. We include an estimate of the diameter of each asteroid using an albedo of 0.25, which is the approximate average of S and Q-type NEAs (Binzel et al., 2004). Again, we include the windowed moving average with a window size ± 1 mag. with its 95% confidence intervals. In general, the average spectral slope decreases with decreasing size, so smaller asteroids have fresher surfaces on average. The linear regression of the spectral slopes vs. absolute magnitude has a slope of -0.024 ± 0.009 %/μm/mag. We also include the linear regression of the spectral slope vs. absolute magnitude for only the asteroids with 0.9 AU $\leq q < 1.3$ AU since that region has does not show a spectral slope vs. perihelion trend. The slope of the linear regression for the asteroids with 0.9 AU $\leq q < 1.3$ AU is -0.02 ± 0.01 %/μm/mag, consistent with the slope

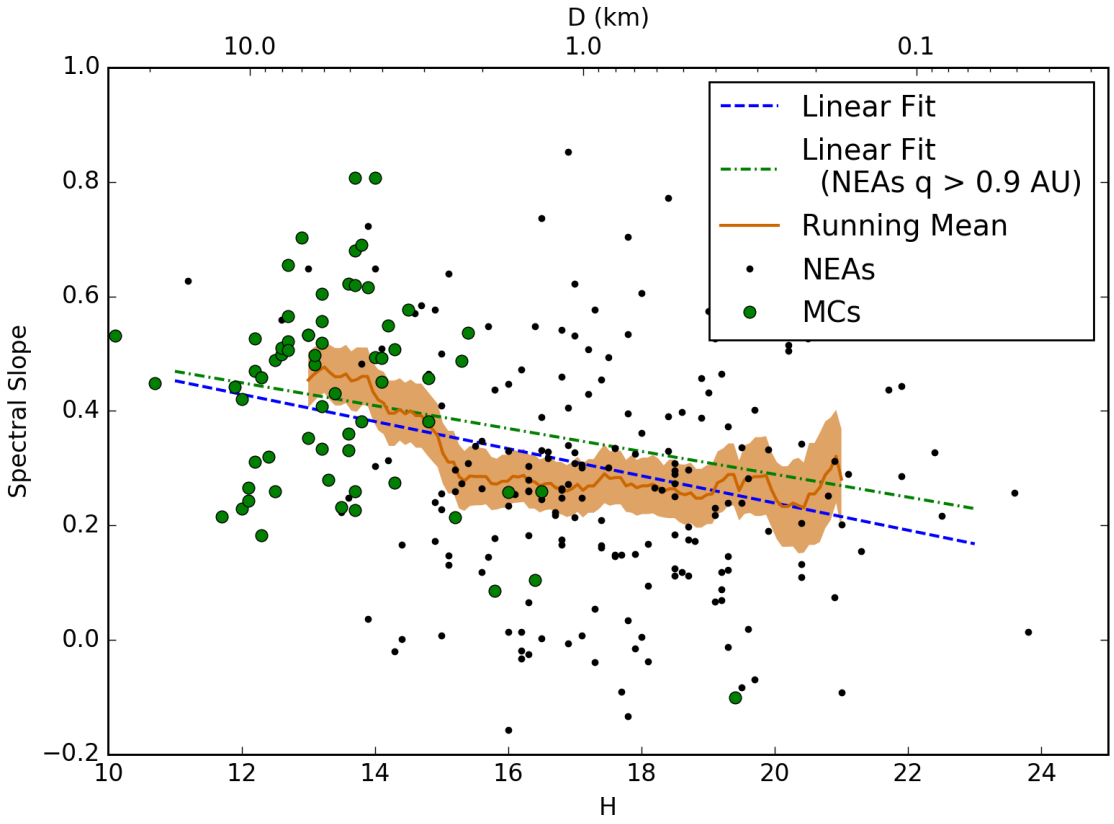

Figure 3.4. The distribution of spectral slope vs. absolute magnitude and diameter using the same data as in 3.3. NEAs are drawn as filled black circles and MCs as filled green circles. The dashed blue line is the linear regression through the asteroids, the solid orange line and shaded region is the windowed moving average of the spectral slopes with a window size of ±0.1 mag and its uncertainty at a 95% confidence level. As noted in Binzel et al. (2004), the average spectral slope does decrease with increasing magnitude.

of the linear regression through the whole population. We also highlight the MCs in Figs. (3.3) and (3.4).

3.2.1 Removing the observational bias in the spectral slope vs. perihelion distribution

There is a bias that is not accounted for in spectral slope vs. perihelion distribution shown in Fig. 3.3. The MCs have a lower average absolute magnitude than the NEAs, with an average magnitude for the MCs of 13.5 ± 0.2 and an average magnitude for the NEAs of 17.5 ± 0.3. Assuming that there is no large systematic difference in the albedos between the NEAs and MCs, then this difference in average absolute magnitude implies that observed MCs are larger than the NEAs, on average. Additionally, we show in the previous section that the gri-slope decreases, on average, with decreasing size in all populations of S and Q-type asteroids.

Because the SDSS data covers magnitudes of up to $H \approx 18$ in the NEA and MC regions, we can conclude that the average spectral slope decreases with decreasing size in the entire population of our NEAs and MCs. Additionally, we show in the previous section that the rate of decrease of spectral slope with size is consistent between the Main Belt and asteroids in the NEA and MC regions. Because this trend appears to be universal in all populations of S-type and Q-type asteroids and that there is no significant difference when only considering asteroids with perihelia $0.9 \text{ AU} \leq q < 1.3 \text{ AU}$ (green dash-dotted line in Fig. 3.3), we make the assumption that there is no significant difference between the rate of decrease in spectral slopes with size in the NEA region and the MC region, and we use the spectral slope vs. magnitude trend shown in Fig. 3.4 to estimate the size-dependent observational bias in the spectral slope vs. perihelion distribution, particularly in the MC region.

To remove the bias, we estimate the spectral slope of each asteroid as if it had a magnitude of $H = 17.5$, the average magnitude of the observed NEAs. We calculate the spectral slope of the linear regression in Fig. 3.4 at the magnitude of each

asteroid, H^*, and at a magnitude of 17.5. Then, we apply a correction based on the difference between those calculated spectral slopes, and that correction is applied to the asteroid's spectral slope. Specifically, we alter each asteroid's spectral slope by:

$$S_D = S_B + [S_\mu(17.5) - S_\mu(H^*)] \tag{3.1}$$

where S_D is the debiased spectral slope of the asteroid, S_B is the initial, biased spectral slope of the asteroid, S_μ is the spectral slope of a point on the linear regression through the spectral slope vs. magnitude distribution (the blue dashed line in Fig. 3.4), which we evaluate at 17.5 and H^*. The moving average in Fig. 3.4, appears to have a much less significant trend for asteroids with $H \gtrsim 15$, so we also attempted to debias the spectral slopes by evaluating S_μ as a point on the windowed moving average, instead of on the linear regression. There is no significant difference between the two results, as the primary change is in the MCs, which primarily exist at $H < 15$. Additionally, if we use the windowed moving average to debias the spectral slopes, we are not able to debais the entire set because there is no corresponding average value of the spectral slopes for the asteroids with the highest and lowest magnitudes.

We apply the correction to each asteroid and show our results in Fig. 3.5. We include a windowed moving average, again with a window size of ± 0.1 AU. We also include two linear regressions through debiased spectral slopes below and above $q = 0.9$ AU. The slope of the linear regression at $q < 0.9$ AU is 0.56 ± 0.21 %/μm/AU, steeper than the slope of linear regression through the entire populations' biased spectral slopes. The slope of the linear regression at $q > 0.9$ AU is 0.03 ± 0.11 %/μm/AU, showing no evidence of any trend.

By debiasing the spectral slope, we show that the increase in spectral slopes at $q \gtrsim 1.3$ AU in Fig. 3.3 is not explained by MCs being more weathered, but by observed MCs being larger than the observed NEAs, combined with an observational bias. Additionally, the requirements for a resurfacing mechanism to explain a perihelion trend in spectral slopes significantly changes. A resurfacing mechanism only needs to affect asteroids with $q \lesssim 0.9$ AU, to match this debiased spectral slope vs. perihelion distribution.

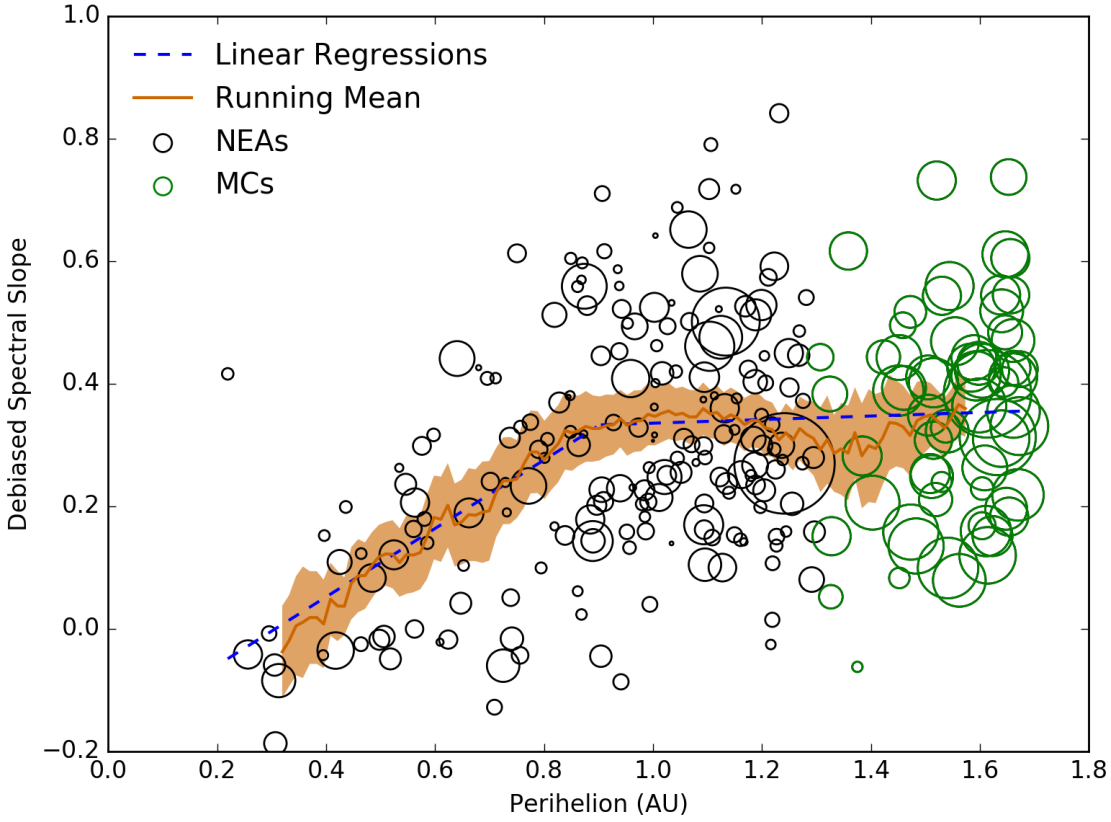

Figure 3.5. Same as Fig. (3.3) except the size bias in the spectral slopes has been removed. See §3.2 for debiasing details. Due to the bias toward observing only large, and thus more highly weathered, MCs, the debaised spectral slope shows no consistent spectral slope vs. perihelion trend above $q \approx 0.9$ AU. The trend in the NEA region does not significantly change.

Due to the relatively consistent range of observed sizes of NEAs for all perihelia, there is not a significant change in the spectral slope vs. perihelion distribution in the NEA region with the debiased data. The slopes of linear regressions of the biased NEAs are 0.52 ± 0.21 %/μm/AU for $q < 0.9$ AU and -0.01 ± 0.31 %/μm/AU for $q > 0.9$ AU, consistent with the slopes of linear regressions of the debiased data. In Chapter 5, we use the windowed moving average through the observed spectral slope vs. perihelion distribution of only the NEAs (denoted by the orange curve lying left of the gray line in Fig. 3.3) as our primary constraint on possible resurfacing mechanisms. We do not model the spectral slopes of MCs due to the difference in the dynamics of NEAs and MCs and due to the lack of evidence for any significant spectral slope vs. perihelion trend in the MCs. We also use average spectral slope of all NEAs with $q > 0.9$ AU of 0.35 ± 0.17 %/μm to define the maximum weathering state for our modeled asteroids.

4 RESURFACING ASTEROIDS FROM YORP SPIN-UP AND FAILURE

Portions of the content of this chapter were published in the journal Icarus as Graves et al. (2018).

4.1 Nominal YORP Spin-up and Failure Model

To understand the process of resetting a surface from YORP spin-up and failure, we develop a Monte Carlo code to compute the evolution of the spin rate and the weathering rate for a population of asteroids. Our YORP evolution model is similar to published models that reproduced the rotation rate of NEAs and main belt asteroids and the size distribution of main belt asteroids (Rossi et al., 2009; Marzari et al., 2011; Jacobson et al., 2014).

We model the evolution of the spin rate by the YORP effect by (Scheeres, 2007; Rossi et al., 2009):

$$\dot{\omega} = \frac{3BG_1}{4\pi\rho a^2\sqrt{1-e^2}}\frac{1}{R^2}\mathrm{C_y} \tag{4.1}$$

where $B \approx 2/3$ is the Lambertian scattering coefficient, $G_1 \approx 10^{17}\mathrm{kg\ m/s^2}$ is the solar radiation constant, ρ is the density of the asteroid, $\mathrm{C_y}$ is a non-dimensional YORP coefficient, R is the volumetric mean radius of the asteroid, and a and e are its semi-major axis and eccentricity. The $\mathrm{C_y}$ parameter describes the effectiveness of YORP on a particular asteroid, and contains information of its shape and moments of inertia. The asteroid's spin rate will accelerate toward a maximum allowed spin rate if $\mathrm{C_y} > 0$ and will decelerate toward a zero spin rate if $\mathrm{C_y} < 0$. Due to the dependence of the acceleration rate on a and R, we expect YORP to become more important at small sizes close to the sun.

Recently, Golubov and Krugly (2012) studied the effects of the normal and tangential components of the solar radiation pressure on the YORP torque and found

that the magnitude of these components are on a similar order. Our model is based on the normal component only.

We also evolve the weathering rate for our population of asteroids. If space weathering is dominated by the solar wind, the rate of exposure will also increase closer to the sun (Marchi et al., 2006b):

$$\text{exposure rate} \sim \frac{1}{a^2\sqrt{1-e^2}} \tag{4.2}$$

Increasing the amount of exposure to the solar wind will continue to change the spectral properties of S and Q-type asteroids until they saturate as a fully weathered S-type. If asteroids are resurfaced by YORP and weathered by the solar wind, we expect to find lower spectral slopes and more Q-type asteroids at smaller sizes, regardless of orbital location, addressing shortcomings of the close encounter models.

In our model, we simulate 10^4 asteroids for 950 Myr, corresponding to the age of the Flora family (Dykhuis et al., 2014). For each asteroid, we select an absolute magnitude from a uniform distribution of $12 < \mathrm{H} < 18$. We only consider the trends based on size, so we do not replicate the size frequency distribution of the asteroid population. We select the initial rotation rate from a Maxwellian distribution with $\sigma \approx 2$ rev/day. The spin rates of small asteroids deviate from a Maxwellian distribution for sizes less than $D \approx 5$ km (Polishook and Brosch, 2009); however, due to the strong effect of YORP on the evolution of small asteroids, the initial rotation rate distribution has no effect on the end state in a YORP evolution model (Rossi et al., 2009).

We assume that all asteroids begin with unweathered surfaces. The initial weathering state of their surfaces is also a transient effect that does not affect the end state of these simulations. We assume that the asteroids in our model can be represented by prolate ellipsoids. We draw an aspect ratio b/a of the smaller to largest axis for each asteroid from a Gaussian distribution with a mean of $\mu = .6$ and a standard deviation of $\sigma = 0.18$ following Jacobson et al. (2014), which matches the aspect ratio of small, fast-rotating asteroids (Michikami et al., 2010). We calculate the maximum

allowed spin rate before failure from a simplified model using the aspect ratio (Pravec and W., 2000):

$$\omega_{max} \approx \sqrt{\frac{4\pi\rho G}{3}\frac{b}{a}} \tag{4.3}$$

where ρ is the density of the asteroid and G is the gravitational constant. We set the density of all asteroids to $\rho = 2500$ kg/m^3.

We do not consider the effect of cohesive forces on asteroid failure in our model. Asteroids larger than approximately 200 m almost never rotate faster than 2.2 h, the critical spin rate for a spherical asteroid held together only by gravity (Pravec and W., 2000). Because our model only considers asteroids down to a size of $H = 18$ ($D \approx 700$ m), cohesion should have little effect on the failure rate of these bodies.

At each timestep, every asteroid is spun up by YORP and is weathered by a simplified space weathering model. We evolve the asteroid spin rate by Eq. 4.1. Following Jacobson et al. (2014), we draw the YORP coefficient C_y from a Gaussian distribution centered at zero with a standard deviation of $\sigma = 0.0125$. The standard deviation is approximated from calculated values of C_y from observed asteroids (Scheeres, 2007).

We do not consider YORP obliquity evolution in our model. The combined obliquity and spin evolution of an asteroid is complex. YORP will cause an asteroid to asymptotically evolve toward a single obliquity value while increasing or decreasing its spin rate (Vokrouhlický and Čapek, 2002; Bottke et al., 2006). Our values of the YORP parameter C_y are derived from observations with a large range of obliquities and are normalized to an obliquity of 90° (Scheeres, 2007). Since an obliquity of 90° often generates the largest absolute value of rotation rate acceleration (e.g., Bottke et al. 2006), we can expect our range of C_y values for the population will incorporate the appropriate range of possible values. Without obliquity dynamics, the evolution of individual asteroids will not be valid, but we can estimate that, for a population of asteroids, the average timescale between resurfacing events will be accurate.

We incrementally weather the asteroids with a simplified space weathering model. We track the time, t, since the last resurfacing event for each asteroid, and calculate a corresponding gri-slope for the asteroid:

$$\mathrm{S} = (\mathrm{S_{max}} - \mathrm{S_Q})(1 - \exp(-t/\tau_{SW})) + \mathrm{S_Q} \tag{4.4}$$

where $\mathrm{S_{max}}$ is the maximum gri-slope an S-type asteroid attains, $\mathrm{S_Q}$ is the gri-slope of a freshly exposed Q-type asteroid, and τ_{SW} is the timescale of the weathering. Eq. 4.4 is a saturation curve and has been used to fit optical properties of an asteroid's surface from the accumulation of space weathering (Brunetto et al., 2006; Willman et al., 2010).

When the spin rate of an asteroid reaches the maximum spin rate, defined by Eq. 4.3, the asteroid experiences a resurfacing event. The resurfacing event could be due to fission, or a large scale surface disruption from global landslides. Regardless of the exact process, we consider the asteroid to be resurfaced. We set the the time since last resurfacing event $t = 0$, and reselect a new YORP coefficient with the condition that $\mathrm{C_y} < 0$. We keep the size and aspect ratio of the asteroid the same. We also make the reasonable assumption that an event that completely resurfaces an asteroid would also change the overall shape of the asteroid, so we also select a new random value of $\mathrm{C_y}$. It is important to note that, depending on how an asteroid's surface fails at high spin rates, it may be possible for the overall shape of the asteroid to change without a total resurfacing event. We discuss the possibility and effects of an incomplete resurfacing event in §4.2.

As an asteroid evolves to a low rotation rate, the asteroid can enter into a tumbling state. The evolution in a tumbling state cannot be represented by our simple model. Following Jacobson et al. (2014), we apply a minimum spin rate of 10^5 hours, at which we reverse the sign of $\mathrm{C_y}$ and allow the asteroid's spin rate to accelerate again.

We do not consider collisions in our model. Previous models have used collisions as an additional mechanism to evolve the spin rate of asteroids and have been necessary to describe the rotation rate distribution of the main belt (Marzari et al., 2011). In our model we are primarily concerned with relative timescales of weathering and

resurfacing of asteroids. Collisions cause infrequent stochastic evolution in the spin rates of the asteroids, but the spin rates of small asteroids are primarily dominated by YORP (Marzari et al., 2011). The stochastic evolution generated from collisions can cause some interesting second order effects which we will discuss in the next section, but they do not substantially change the results of our modeling.

Using the Flora family SDSS data (Fig. 3.2), we set the values of some of the parameters in Eqs. 4.1 and 4.4. From the location of the Flora family in the inner main belt, we set $a = 2.2$ AU and $e = 0$ in Eq. 4.1. We also make the assumption that the space weathering timescale, described in Eq. 4.4, is dominated by the solar wind. The solar wind has an dependence on the orbit shown in Eq. 4.2, so the timescale of space weathering τ_{SW} is dependent on our choice of a and e. We can use Eq. 4.2, to scale the space weathering timescale to other values of a and e.

We derive the maximum gri-slope, S_{max}, from a normal distribution based on the distribution of Flora family asteroids with magnitudes of $H < 13$. For the Flora family members, we find an average value of 15.9 %/100 nm and a standard deviation of 1 %/100 nm. We selected S_Q from a normal distribution with an average of 6 %/100 nm and a deviation of .5 %/100 nm, which corresponds to the lower end of the range of gri-slopes for Q-types in the DeMeo and Carry (2013) classification scheme.

With the assumptions made above, the space weathering timescale τ_{SW} is the only free parameter in our model. Due to the form of our space weathering model, space weathering will asymptotically approach S_{max} with an e-folding time τ_{SW}. We vary τ_{SW} in our model to find the best fit. Fig. 4.1 shows a good fit for $\tau_{SW} = 45$ Myr. We show the gri-slope vs. absolute magnitude distribution of the model results, along with the running mean of both the model results (box size of 330) and the data from the Flora family from Fig. 3.2.

We also find a range of space weathering timescales that acceptably fit the distribution. In Fig. 4.2, we show the Root Mean Square Error (RMSE) between the running mean of the observed and modeled asteroids. The box sizes of the running means were chosen to approximately select from the same range of H values, but

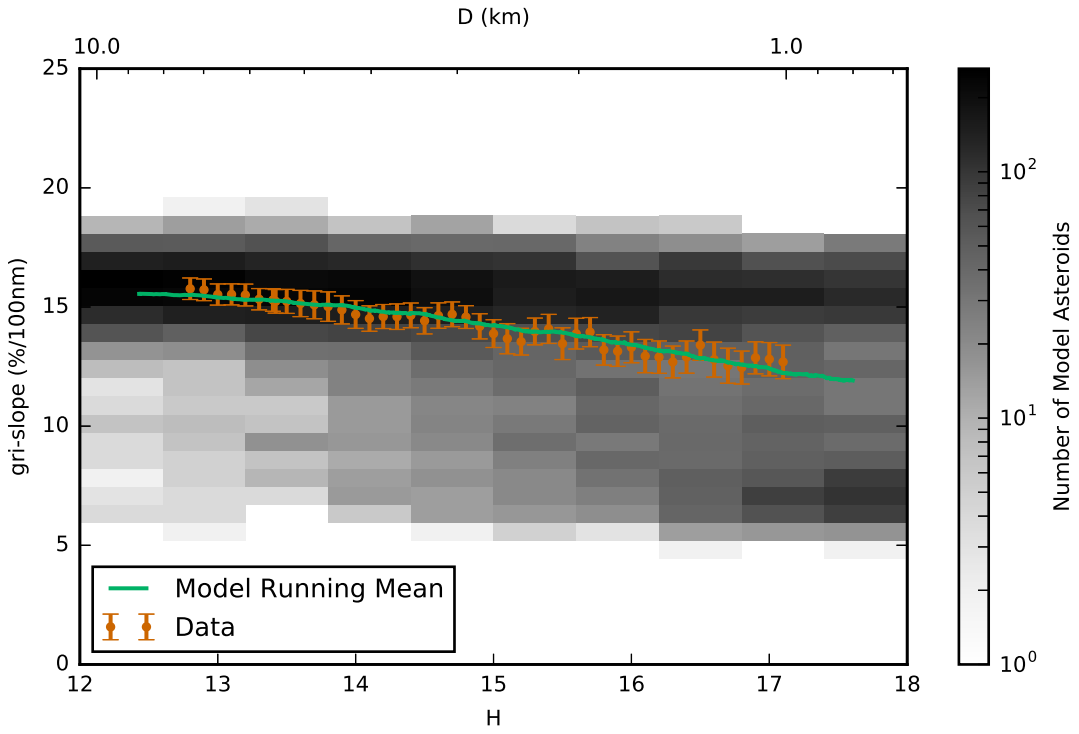

Figure 4.1. The modeled asteroids' gri-slope vs. absolute magnitude distribution for the best fit solution with an e-folding space weathering timescale of $\tau_{SW} = 45$ Myr at 2.2 AU. The points and error bars are the running mean of the gri-slope with a box size of 15 and the uncertainty at a 95% confidence level of the Flora family asteroids (from Fig. 3.2). The solid line is the running mean of the gri-slope of the modeled data with a box size of 330. The uncertainty of the mean for the model data is smaller than the thickness of the line.

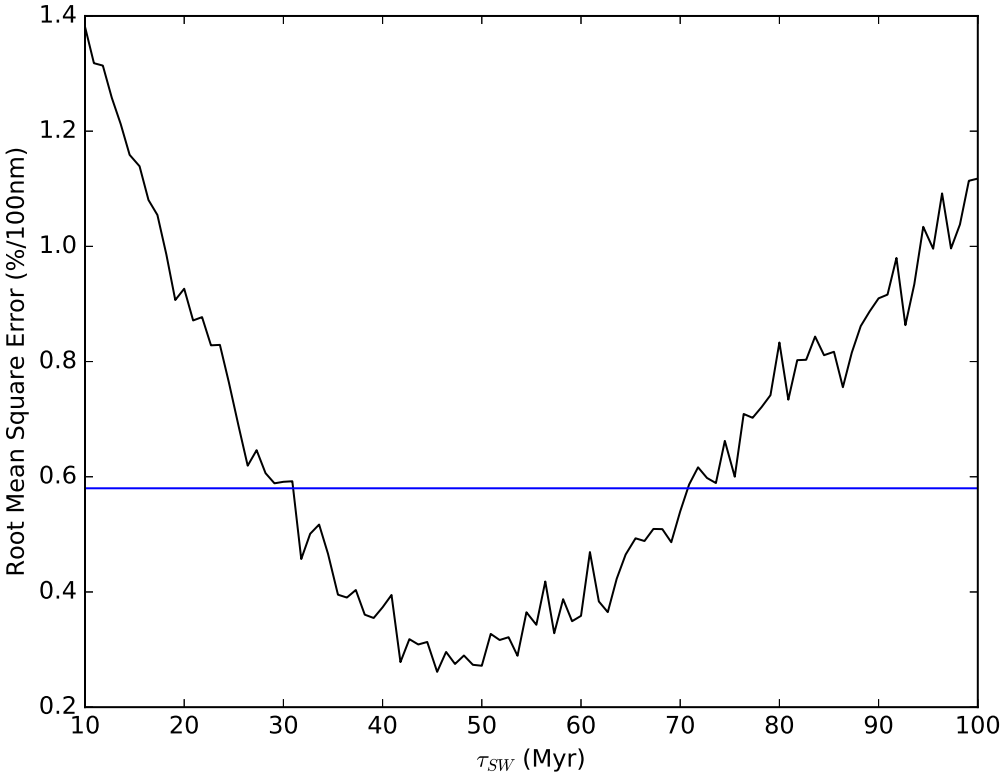

Figure 4.2. The Root Mean Square Error (RMSE) of the gri-slope vs. size running mean of the Flora family and the modeled asteroids. The box sizes of the running mean of the observed and modeled asteroids are selected to sample the approximately the same range of absolute magnitudes. We use the average uncertainty of the mean values of the Flora family asteroids of $\pm.58$ %/100 nm as a cutoff to define the best fit RMSEs. The range of acceptable space weathering timescales from the nominal model is $\tau_{SW} = 32 - 70$ Myr, where the RMSE $\leq$ .58 %/100 nm.

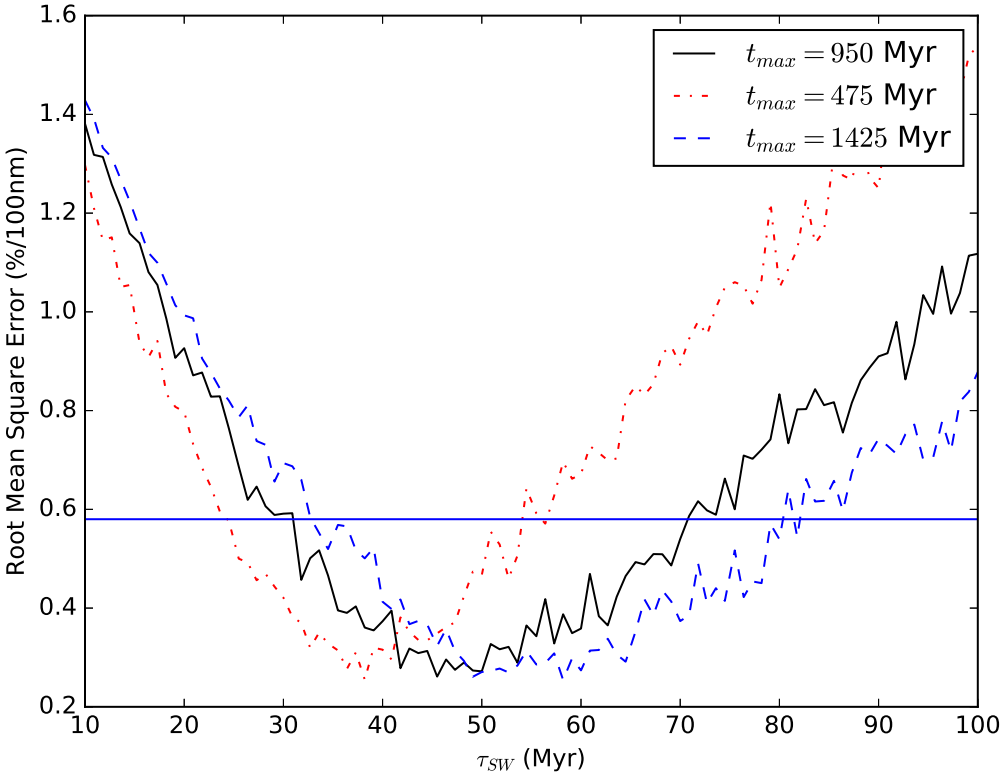

Figure 4.3. Similar to Fig. 4.2, except that we show results from the altering the maximum time, t_{max}, of the model. A larger t_{max} will allow the population to further evolve toward smaller values of C_y and allow for more rapid YORP evolution, and vice versa for lower values of t_{max}. The change to the τ_{SW} is relatively minor for reasonable values of t_{max}, especially for the minimum bound of τ_{SW}.

the RMSEs are insensitive to small variations in the box size. We used the average uncertainty of the mean values of the Flora family asteroids of $\pm.58$ %/100 nm as a cutoff to define the best fit RMSEs. We found a range of space weathering timescales, $\tau_{SW} = 32 - 70$ Myr, where the RMSE $\leq .58$ %/100 nm.

To make these results more comparable to previous studies, we can estimate the time it takes for a newly resurfaced Q-type asteroid to weather such that it would become an S-complex asteroid, $\tau_{Q \to S}$. From DeMeo and Carry (2013), the maximum slope a Q-type asteroid can have is 9.5 %/100 nm. We find the average time that it takes to weather an asteroid from a newly resurfaced state, with a gri-slope of ~ 6 %/100 nm, to a state where the gri-slope is 9.5 %/100 nm. From our range of estimates for the space weathering timescale, we estimate $\tau_{Q \to S} \approx 14 - 31$ Myr. These timescales should only be taken as an approximate maximum, as S-type asteroids can have gri-slopes as low as 6 %/100 nm in the classification of DeMeo and Carry (2013). It is the combination of a low gri-slope and a low z′-i′ color (corresponding to a deep 1 μm absorption band) that defines the unweathered Q-types. Additionally, we can scale these timescales to any orbit using Eq. 4.2:

$$\tau_{Q \to S} = \tau_0 \cdot \left(\frac{a}{1 \text{ AU}}\right)^2 \sqrt{(1 - e^2)} \tag{4.5}$$

where $\tau_0 \approx 3 - 6$ Myr. In the next section, we address the effects of the assumptions that we use in our nominal YORP spin-up and failure model.

4.2 Testing Assumptions of Nominal Model

In the construction of our nominal model we made necessary assumptions and selected parameters that have been previously used in the literature. In this section, we discuss and vary the parameters and assumptions made in the nominal model.

An important effect in the model is that the distribution of the YORP coefficients is not in steady state throughout the simulation. As asteroids evolve to the maximum spin rate, and a resurfacing event occurs, their YORP coefficients are randomly re-drawn. However, for a given asteroid size, those with a larger absolute C_y values will

evolve more quickly and change their C_y values more often. Over time, more asteroids will get "stuck" with low C_y values. Additionally, this trend toward lower values of C_y is more pronounced for smaller asteroids due to their more rapid YORP evolutions. Asteroids that are stuck in these low C_y states will evolve more slowly and lengthen the timescale between resurfacing events, slightly raising the average gri-slopes for smaller asteroids. These low C_y states for small asteroids are important to match the Flora family distribution of gri-slopes at all sizes. Without the slight raising of the average gri-slopes for smaller asteroids, there would be an overabundance of asteroids with very low gri-slopes at small sizes ($H \gtrsim 16$).

The effect of the trend toward lower values of C_y on the derived necessary space weathering timescale is minor. We test the effect of this trend by altering the length of our simulations, $t_{\max}$. In Fig. 4.3, we show the distribution of the RMSE between the running mean of the model and observations for a range of space weathering timescales and for different values of $t_{\max}$. For lower values of $t_{\max}$, the trend toward lower values of C_y, is muted and restricted to only the smallest asteroids, resulting in shorter resurfacing timescales and requiring a shorter space weathering timescale. By increasing $t_{\max}$, asteroids will have more resurfacing events and causes slightly more asteroids in the simulation to be "stuck" with low C_y values, resulting in longer resurfacing and space weathering timescales. If $t_{\max}$ becomes too small (~ 100 Myr), the initial weathering state of the asteroids begins to become important. Varying the nominal value of $t_{\max}$ by $\pm 50\%$ only slightly changes the minimum bound of τ_{SW}. The maximum bound of τ_{SW} does change more significantly. Raising $t_{\max}$ by 50% raises the maximum bound of τ_{SW} to ≈ 80 Myr, and lowering $t_{\max}$ by 50% lowers the maximum bound of τ_{SW} to ≈ 54 Myr.

For asteroids to get stuck with low C_y values, the population must be left undisturbed for a period of time equal to $t_{\max}$. Collisions can create large craters and move boulders on the surface of asteroids, which can cause a significant change in the YORP coefficient (Statler, 2009). This high sensitivity of YORP to the exact shape of the asteroid, called Stochastic YORP (Bottke et al., 2015), could cause small collisions

to disturb the asteroids with low values of C_y, thereby increasing C_y, and allowing those asteroids to resurface more often. Marzari et al. (2011) first used collisions alongside YORP evolution. They considered that collisions could effectively induce stochastic evolution by randomly selecting a new C_y after any collision changed the obliquity of the asteroid by > 0.2 radians. They found that collisions could trap large (≈ 5 km) asteroids in a low spin state, which could lengthen the time between resurfacing events. This effect quickly becomes less important at sizes less than 5 km, as YORP begins to more strongly dominate the spin evolution of the asteroid. Since ≈ 5 km is where the trend in decreasing gri-slope with decreasing size begins, we assume that this effect will only cause a minor change in the average gri-slopes of asteroids in our model.

Collisions could potentially decrease the average gri-slope of the smaller asteroids in our model, where the trend toward lower values of C_y is the strongest. Collisions could change C_y often enough to quickly remove any asteroid stuck in a low C_y state, which would keep the time between resurfacing events relatively short. However, the effect of collisions on the evolution of asteroids in our model could be highly dependent on the number of small impactors in the main belt. The exact impactor Size Frequency Distribution (SFD) at sizes $\lesssim 1$ km in the main belt is not well understood. Collisional evolution models predict a steep power law slope ($N(> D) \sim D^{-3.5}$) and many small impactors (Dohnanyi, 1969; Bottke et al., 2005). The SDSS and the Sub-Kilometer Asteroid Diameter Survey, suggest a shallow power law slope ($N(> D) \sim D^{-2.5}$) continuing down to sizes $D \sim 200$ m (Ivezić et al., 2001; Gladman et al., 2009). The rotational disruption model of Jacobson et al. (2014) creates an SFD that also matches well with the shallower power law slope of these observations. A shallower power law could mean less impactors at small sizes, and a slower removal of asteroids stuck with low values of C_y. Regardless of the impact rate, collisions should only affect the resurfacing rate of the smaller ($D \lesssim 2$ km) asteroids. Larger asteroids would still resurface at a similar rate and require a similar space weathering timescale to match

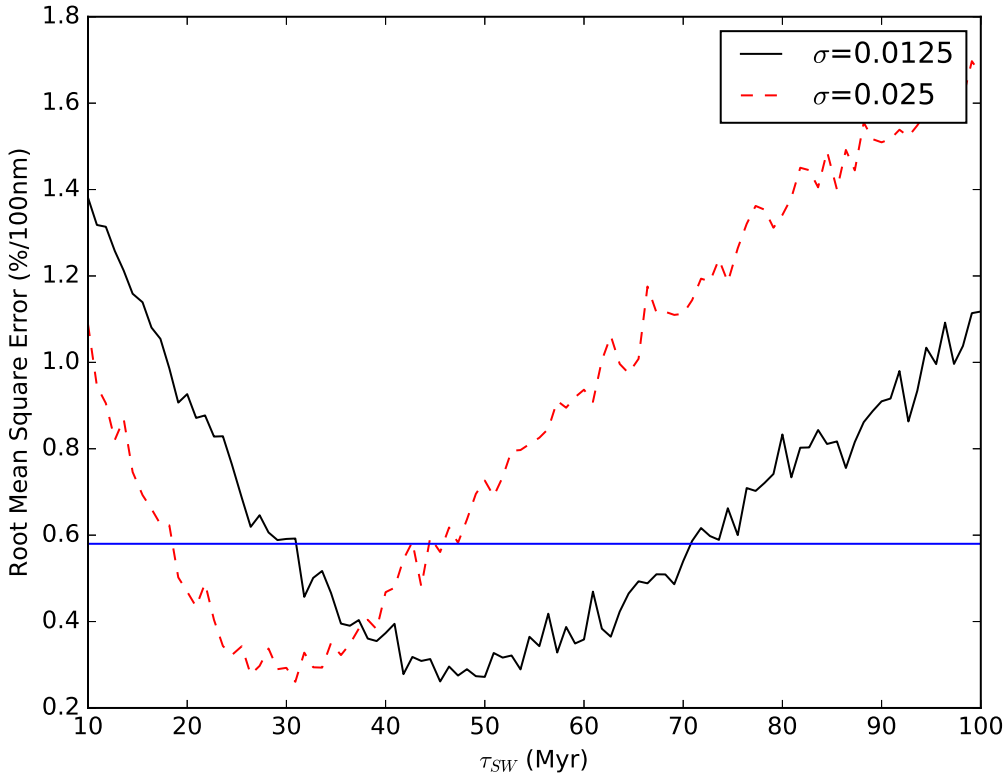

Figure 4.4. Similar to Fig. 4.2, except that we also show results from doubling the standard deviation of the distribution of C_y. A wider distribution of C_y, allows asteroids to evolve more quickly and resurface more often, lowering the acceptable values of τ_{SW}.

observations. The complex interaction between collisions and the resurfacing rate of asteroids from failure at high spin rates are left for a future study.

The only reasonable change to a parameter that could allow for a shorter space weathering timescale in our model would be increasing the value of C_y. Our nominal distribution of C_y matches well with the measured values of 0.022 and 0.005 for asteroids (1862) Apollo (Kaasalainen et al., 2007) and (54509) YORP (Taylor et al., 2007; Lowry et al., 2007), respectively, under the assumption that these asteroids were affected by YORP. As small asteroids settle into low values of C_y in our model,

Location	τ_{SW} (Myr)	$\tau_{Q\rightarrow S}$ (Myr)
NEA Region ($a \approx 1$ AU)	4-17	2-7
Inner Main Belt ($a \approx 2.2$ AU)	19-80	8-35
Middle Main Belt ($a \approx 2.7$ AU)	29-120	12-53
Outer Main Belt ($a \approx 3.1$ AU)	38-159	16-69

Table 4.1.
Space weathering timescales for different populations of S and Q-type asteroids. Values are calculated with $\tau_0 \approx 4-17$ Myr for the e-folding timescale (τ_{SW}) and $\tau_0 \approx 2-7$ Myr for the Q-type removal timescale ($\tau_{Q\rightarrow S}$). All timescales are calculated with zero eccentricity.

the standard deviation of C_y decreases to $\sim$ .006%/100 nm after 950 Myr, about half of the initial value. Any measurements of C_y of asteroids today could be skewed toward these lower values. To test the effect of changing C_y, we run the model where we select C_y from a Gaussian distribution centered at zero with a standard deviation of $\sigma = 0.025$, twice the nominal value. The RMSE values with the new distribution of C_y for a range of space weathering timescales is shown in Fig. 4.4. Using these larger values of C_y, we estimate that the needed space weathering timescale can be as short as 19 Myr in the main belt, resulting in space weathering timescales of $\tau = \tau_0 \cdot \left(\frac{a}{1\text{ AU}}\right)^2 \sqrt{(1-e^2)}$, where $\tau_0 \approx 4-17$ Myr for the e-folding timescale (τ_{SW}) and $\tau_0 \approx 2-7$ Myr for the Q-type removal timescale ($\tau_{Q\rightarrow S}$). Both of these values of τ_0 are generated from the range of possible solutions discussed in this section. Table 4.1 provides a list of the approximate e-folding and Q-type removal space weathering timescales for the NEA region, and the inner, middle, and outer main belt.

After reaching the maximum spin rate, an asteroid could experience a number of different effects. Some models have shown that asteroids could fission to form a binary or pair at high spin rates (Walsh and Jacobson, 2015). After a fissioning event, the evolution of a binary asteroid can take different pathways, some of which can slow down the spin rate evolution of the asteroid from YORP (Jacobson and

Scheeres, 2011), implying that this mechanism could lengthen the timescale between resurfacing events. We expect binary formation to have a higher order effect on the resurfacing rate of asteroids, and we leave its investigation for a future study. Other modeling efforts such as Hirabayashi (2015), have shown that, depending on the internal structure, spherical asteroids could experience large scale failure at high spin rates, which would not necessarily result in a fission. Any large scale failure could alter the shape of the asteroid and change the sign and magnitude of C_y causing the asteroid to decrease its rotation rate.

Regardless of the outcome of the asteroid's surface at its maximum spin rate, we have considered the asteroid to be fully resurfaced in our model. There is a possibility in both the fissioning and non-fissioning cases that the asteroid would not completely resurface. Movement of a fraction of the surface could change the YORP parameter enough to cause the asteroid's rotation rate to decrease, but it would not completely resurface the asteroid and reset its spectral slope. For instance, repeated landslides and internal deformation, such as those hypothesized to create the equatorial ridge on fast rotating "top-shaped" asteroids, such as (66391) 1999 KW4 and (29075) 1950 DA (Walsh et al., 2008; Hirabayashi and Scheeres, 2015), could refresh the material on only a limited part of the asteroid's surface. Also, Polishook et al. (2014) suggested that a fission event could be followed by the spreading of dust, which coats the primary and secondary in weathered material and covers any exposed unweathered material.

Unfortunately, there is no clear understanding of the surface evolution of asteroids at high rotation rates. For a partial resurfacing due to landslides or internal deformation, it is unclear what fraction of surface material is displaced when an asteroid reaches its maximum spin rate. Additionally, the probability that an asteroid will experience a certain type of evolution - fission, surface shedding, or large-scale deformation - is unknown. Due to the lack of clear understanding of the surface evolution at high spin rates and to keep unconstrained parameters to a minimum, we only consider the case where an asteroid is fully resurfaced every time it reaches its maximum spin rate.

Previous studies, such as Čapek and Vokrouhlický (2004), Golubov and Krugly (2012), and Bottke et al. (2015), have investigated a bias of YORP torques toward either prograde or retrograde. Unfortunately, these investigations have not converged to a single conclusive answer. We do not account for any YORP directional bias in our model.

4.3 Discussion

Modeling studies of resurfacing mechanisms are very important because they can allow us to find a range of space weathering timescales at which certain mechanisms are important. By varying parameters in the last section, we find the full range of the space weathering timescale needed for YORP spin-up and failure, $\tau_{SW} \approx 19-80$ Myr. Our estimated Q-type removal timescale, $\tau_{Q \rightarrow S(1AU)} \approx 2-7$ Myr, is shorter than those calculated assuming that disruptive collisions are the primary resurfacing mechanism, but is still longer than laboratory estimates (Willman and Jedicke, 2011; Strazzulla et al., 2005). If the space weathering rate is $\tau_{SW} \sim 1$ Gyr in the main belt as calculated in Willman and Jedicke (2011), from only destructive collisional resurfacing, we would expect YORP spin-up and failure to keep asteroids smaller than a few kilometers uniformly unweathered. This prediction is not consistent with observations, and it suggests that YORP spin-up and failure is a more effective resurfacing mechanism that catastrophic collisions and that the space weathering timescale must be shorter than 1 Gyr.

Laboratory estimates using solar wind as a source find a faster space weathering rate by an order of magnitude or more than what is required for YORP to be the primary resurfacing mechanism for small asteroids. These faster laboratory measurements require one of two things: (1) another mechanism is resurfacing asteroids at a faster rate than YORP spin-up and failure, or (2) the observed space weathering rate is longer than the experimentally derived space weathering rate. A longer observed space weathering rate could be generated from gardening of the surface from

small impacts or small landslides as the spin rate and the local slopes on the asteroid change. These local resurfacings would expose unweathered material, giving the asteroid a less weathered overall spectrum, and increasing the time for an asteroid to become saturated (Shestopalov et al., 2013). We also find our estimated space weathering timescale to be comparable ($\sim 2-7$ times longer) than the timescale needed for planetary encounters to create the 20% of Q-types seen in the NEA population from the model of Nesvorný et al. (2010). It is possible that both could be effective resurfacing mechanisms in the NEA region.

There are also other effects apart from YORP spin-up and failure that could cause the spectral slope vs. size trend seen in the data. Collisions and subsequent seismic shaking have been cited as a possible explanation for the similar trend seen in the Koronis Family (Rivkin et al., 2011; Thomas et al., 2011, 2012). Rivkin et al. (2011) used an order of magnitude argument to suggest that the timescales for collisions and seismic shaking, and space weathering are comparable. It is unclear whether seismic shaking could match the slope and shape of gri-slope vs. size trend or whether that resurfacing rate would be faster or slower than YORP. Its investigation is left for future work.

We discussed in the last section that we do not include binary formation in our model; however, since YORP can create both binary and Q-type asteroids, the number of Q-type vs. S-type binaries can hint at the relative lifetimes of Q-type and binary asteroids. A full statistical analysis is left for future work, but even finding binary Q-type asteroids, such as (1862) Apollo (Pravec and Harris, 2007; DeMeo et al., 2014), suggests that a YORP induced fission (and not a close encounter with Earth or Venus) may have been the last event to resurface that asteroid. This prediction is reasonable because a close encounter with a planet would much more readily disrupt the binary before it would disturb the surface of either member. Walsh et al. (2008) showed that close encounters can only be expected to create a small fraction of the binaries in the NEA region, making it unlikely that (1862) Apollo formed by tidal effects. The destruction of binary asteroids is most often due to the Binary YORP effect (Ćuk

and Burns, 2005; Jacobson and Scheeres, 2011; Walsh and Jacobson, 2015), which will scale in orbit together with YORP and space weathering. However, we only expect YORP and Binary YORP, and not the space weathering rate to scale with size. A strong prediction of this study is that we should observe more Q-types among small binary asteroids compared to larger binaries.

The spectral slope vs. size trend in this study is not the only trend in spectral slopes that is seen for the S and Q-type asteroids. Marchi et al. (2006a) first noted that there is a spectral slope vs. perihelion trend in the NEAs and MCs. It was these observations that led to further investigations of creating Q-type asteroids from close encounters with the terrestrial planets (e.g., Binzel et al. 2010; Nesvorný et al. 2010; DeMeo et al. 2014; Carry et al. 2016). Boulder breakdown from thermal cycling could also work to resurface asteroids in the NEA region and could naturally create the slope vs. perihelion trend (Delbo et al., 2014; Molaro et al., 2015), although further investigations are necessary. Our study has not considered the perihelion trend, and YORP coupled with space weathering originating from the solar wind will not reproduce it. It seems that there must be at least two primary mechanisms resurfacing asteroids: one effect (such as YORP spin-up and failure) creating the spectral slope vs. size trend and another effect creating the slope vs. perihelion trend. Additionally, if the mechanism creating the perihelion trend is independent of size, which would be reasonable for resurfacing from close encounters with the terrestrial planets or from thermal cycling, it could also explain the size-independent lower gri-slopes in the NEAs and MCs compared to the main belt that is seen in Fig. 3.1.

4.4 Conclusion

From gri-slopes of main belt asteroids, MCs, and NEAs gathered from the Sloan Digital Sky Survey, we showed that S-type and Q-type asteroids are, on average, less weathered at smaller sizes, regardless of orbital location. We found the slope of the

linear trends of the gri-slope vs. absolute magnitude distributions to be $-0.42 \pm 0.04\,\%/100$ nm/mag and $-0.36 \pm 0.17\,\%/100$ nm/mag for the main belt asteroids, and the NEAs and MCs, respectively. The similarity between the trends suggested a common resurfacing mechanism that preferentially reduces the average gri-slopes of S and Q-type asteroids at smaller sizes. Additionally, we presented the gri-slope vs. size distribution of the Flora family asteroids to remove any compositional trends in gri-slope and any observational biases. We found a steeper slope of the linear trend through the Flora family asteroids of $-0.73 \pm 0.15\,\%/100$ nm/mag.

We presented the first resurfacing model from YORP spin-up and failure to explain the weathering trends with size. With a simple YORP evolution and space weathering model, we can fit the observed gri-slope vs. size trend in the Flora family asteroids. By varying the non-dimensional YORP coefficient distribution and the run time of the model, we find a range of values for the space weathering timescale $\tau = \tau_0 \cdot \left(\frac{a}{1\text{ AU}}\right)^2 \sqrt{(1-e^2)}$, where $\tau_0 \approx 4 - 17$ Myr for the e-folding timescale and $\tau_0 \approx 2 - 7$ Myr for the Q-type removal timescale.

Given the assumptions in our model, we conclude that YORP spin-up and failure is an effective mechanism for resurfacing small asteroids. The relative effectiveness between YORP and other resurfacing mechanisms affecting only small asteroids, such as impacts and subsequent seismic shaking, is left for future work.

5 RESURFACING ASTEROIDS AT LOW PERIHELIA

5.1 Introduction

In this chapter, I investigate two potential resurfacing mechanisms: (1) tidal effects from close encounters with the terrestrial planets, and (2) thermally-induced surface degradation. I show the possible spectral slope vs. perihelion distributions that can be created from each mechanism and compare them to the observed distribution quantified in Chapter 3. I find that tidal effects from close encounters with the terrestrial planets cannot generate a distribution that can match observations for any reasonable combination of parameters, and that thermally-induced surface degradation provides a much better fit. Thus, close encounters with the terrestrial planets are not an important resurfacing mechanism, and, while more work needs to be done to fully understand the process of thermally-induced degradation on the surfaces of asteroids, it is very likely that it plays a crucial role in resurfacing asteroids in the NEA region.

5.2 Modeling Methods

To model the spectral slopes of asteroids at low perihelia ($q \lesssim 0.9$ AU), we must consider the evolution of asteroids from from their source regions in the main belt, and track their orbits throughout their lifetime in the NEA region. By combining information on the amount of accumulated space weathering, resurfacing processes, and the current perihelion of each asteroid throughout the simulation, we can model the spectral slope vs. perihelion distribution.

In the model of Bottke et al. (2002), the three primary source regions of S and Q-type NEAs are the 3:1 mean motion resonance with Jupiter, the ν_6 secular resonance, and the Intermediate source Mars Crossers (IMCs). The IMCs are a subset of the

Mars crossing population that are below the ν_6 resonance and are not in the 3:1 mean motion resonance. We do not consider other source regions, such as the outer belt resonances, because they do not contain a significant number of S and Q-type asteroids (DeMeo and Carry, 2013), and they contribute less to the steady state population of NEAs when compared to the above three (Bottke et al., 2002). We note that there is a recent updated estimate to the near-Earth Object fluxes in Granvik et al. (2018). However, we do not expect our results to significantly change with the inclusion of this updated model because the results of the two resurfacing methods are similar when considering each of the three source regions alone. It appears that, in our model, the estimate of the NEA fluxes plays a minor role compared to the weathering and resurfacing that occurs once the asteroids are in the NEA region.

We integrate the orbits of 6000 asteroids, with 2000 initially in each of our source regions. Asteroids in the 3:1 mean motion resonance with Jupiter are randomly distributed within a semi-major axis of $a = [2.48 - 2.52]$ AU, an eccentricity of $e < 0.35$, and an inclination of $i < 15$ degrees. Asteroids in the ν_6 secular resonance begin with a semi-major axis of $a = [2.06 - 2.37]$ AU, an eccentricity of $e = 0.1$, and an inclination of $i = [2.5 - 15]$ degrees. The semi-major axis and inclination are selected such that the asteroids fall within the strong part of the ν_6 resonance, described in detail in Morbidelli and Gladman (1998). Asteroids in the IMCs are generated to match the semi-major axis, inclination, and eccentricity distribution of observed asteroids with a magnitude of $H < 16$ in the IMC region, using 3373 asteroids pulled from the JPL Small Body Database (ssd.jpl.nasa.gov). These initial conditions are very similar to those in Bottke et al. (2002), and generate statistically similar NEAs.

We use a Regularized Mixed Variable Symplectic (RMVS) integrator in the SWIFTER N-body code (Levison and Duncan, 1994) to integrate the asteroids. We include all eight major planets, but do not account for the general relativistic effects on Mercury's orbit. We integrate all asteroids with a 1 day timestep and the simulation runs for 100 Myr. We tested a subset of our model with a 12 hour timestep and found

no difference in the final average spectral slope vs. perihelion distribution. We also remove asteroids from the simulation if they collide with the Sun or a planet or have a semi-major axis larger than 1000 AU. Due to the relatively short integration time of 100 Myr and the chaotic nature of NEAs, we do not expect the small deviations in Mercury's orbit from general relativistic effects to change the close encounter statistics or the orbital distributions of the NEAs. Additionally, encounters with Mercury are very rare compared to encounters with the other terrestrial planets. The integrator records all close encounters between asteroids and planets within 3.5 Hill Radii of the planet.

We also simulate the increase in the asteroids' spectral slopes over time using a simplified space weathering model. If an asteroid remains in its current orbit and experiences no resurfacing events, the rate of change of the spectral slope depends on the current spectral slope of the asteroid (Brunetto et al., 2006; Willman et al., 2010). In other words, the spectral slope of an asteroid being space weathered follows an exponential saturation curve, where the rate of increase of its spectral slope decreases as the asteroid becomes more weathered. Since we constrain the spectral slope to a maximum value of $\mathrm{S_{max}}$, we can express the rate of change in spectral slope due to space weathering as:

$$\left(\frac{d\mathrm{S}}{dt}\right)_{SW} = \frac{1}{\tau_{SW}}\left(\mathrm{S_{max}} - \mathrm{S}\right). \tag{5.1}$$

where S is the slope of the asteroid and τ_{SW} is its e-folding space weathering timescale.

We assume that the process of space weathering is dominated by the alteration of an asteroid's surface by the solar wind because of its much smaller timescale. Because the intensity of the solar wind scales with the solar distance as $1/r^2$, we scale the space weathering timescale accordingly:

$$\tau_{SW} = \frac{\tau_{SW0}}{(1\ \mathrm{AU})^2}\frac{P}{\oint r^{-2}dt} = \frac{\tau_0}{(1\ \mathrm{AU})^2}a^2\sqrt{1-e^2}, \tag{5.2}$$

where r is the instantaneous solar distance of the asteroid, P is the orbital period, a and e are its semi-major axis and eccentricity, and τ_{SW0} is the space weathering timescale at $a = 1$ AU and $e = 0$. The integral in Eq. 5.2 is taken over one orbit.

Throughout the simulation, the asteroid's orbit evolves, and the space weathering timescale τ_{SW} changes. Thus, we increment the spectral slope at each timestep with Eq. 5.1 to accurately represent the spectral slope over its evolution throughout the NEA region.

We select the minimum spectral slope, S_{OC}, and maximum spectral slope, S_{max}, for each asteroid randomly from Gaussian distributions. We use the spectral slopes of OC meteorites to calculate the value of S_{OC}, with the mean value $\mu_{OC} = 0$ and the standard deviation $\sigma_{OC} = 0.05$, approximately matching the OC spectral slopes used in Vernazza et al. (2009). We use the distribution of spectral slopes from NEAs with perihelia $q > 0.9$ AU to calculate the value of S_{max} (Fig. 3.3). By using the average spectral slope for NEAs with $q > 0.9$ AU, we are not necessarily finding the average spectral slopes of completely weathered S-type asteroids. There are other resurfacing mechanisms that can lower the average spectral slope of the entire population, but there is no significant spectral slope vs. perihelion trend at $q > 0.9$ AU. We find a mean value of $\mu_{max} = 0.34$ and standard deviation of $\sigma_{max} = 0.1$.

At the beginning of the simulation all asteroids start at S_{max}, simulating a lack of spectral slope vs. perihelion trend in the MCs and main belt. Then, throughout the integration, an asteroid can experience resurfacing processes either through close encounters or thermally induced degradation. These effects, which are described in §5.3.1 and §5.4.1, will cause the spectral slopes of asteroids to decrease. We calculate the change in spectral slope on each asteroid from space weathering every 10^4 years. For the close encounter resurfacing model, we apply the change in the spectral slopes due to a resurfacing encounters at the time of the encounter, and for the thermally induced degradation model, we also calculate the change in spectral slope on each asteroid every 10^4 years. We then save the perihelion and spectral slope of each asteroid in the NEA region every 10^5 years throughout the simulation to measure the effect of the resurfacing and weathering processes on the spectral slope vs. perihelion distribution. Shorter timesteps for calculating the change in spectral slope and for saving the perihelion and spectral slope of each asteroid yield similar results.

We use the positions and spectral slopes from timesteps throughout the simulation to generate a representative sample of the steady-state NEA distribution. According to Bottke et al. (2002), the ν_6 resonance, the 3:1 resonance, and the IMCs generate approximately 37%, 27%, and 20% of the population of NEAs at any given time. By simply selecting all asteroids in the NEA region every 10^5 years, we will not generate the appropriate total fraction of asteroids evolving from each source region. To account for this, we artificially duplicate instances of a perihelion and a spectral slope of an asteroid at a random time from underrepresented source regions until we find the correct distribution. Specifically, we find the number of saved asteroids from each source region across all timesteps: $N_{3:1}$, N_{ν_6}, and N_{IMC}. Then, we find the maximum of ($N_{\nu_6}/0.37$, $N_{3:1}/0.27$, $N_{IMC}/0.2$) corresponding to the source region that has the largest number of asteroids over the needed fraction. We artificially increase the number of the other two source regions and repeat this process until we reach the appropriate fractions for each source region.

For both resurfacing mechanisms, we consider a range of possible parameters. Due to the computational cost of running the N-body integration, we reuse its results for each set of parameters. For each new parameter set, we select a new S_{max} and S_{OC} for each asteroid from the appropriate distribution, and evolve the spectral slopes according to the model and the specific parameters. There are two primary sources of uncertainty in calculating the windowed moving average from the modeled asteroids: (1) the selection of S_{max} and S_{OC} for each asteroid at the beginning of the simulation, and (2) the randomized artificial increase in the number of asteroids from underrepresented source regions. To reduce the uncertainty from these two sources, we run each set of parameters 12 times with randomized values of S_{max} and S_{OC} and randomized duplication of asteroids from underrepresented source regions for each iteration. The final spectral slope vs. perihelion distribution for a specific set of parameters is the combination of all of the spectral slope and perihelion pairs from all 12 iterations.

After applying these iterations, we have almost 4 million total sets of perihelia and spectral slopes from all iterations (including all source regions) for each set of pa-

rameters to compare to the NEA distribution in Fig. 3.3. We calculate the windowed moving average through the modeled spectral slope vs. perihelion NEA distribution with a window size of ± 0.1 AU. We then calculate the Root Mean Square Error (RMSE) between the windowed moving averages of the observed spectral slope vs. perihelion distribution and the modeled distribution. A lower RMSE corresponds to a better fit, and we define acceptable solutions by the condition that $\geq 95\%$ of the points on the modeled windowed moving average must fall within the 95% confidence intervals of the windowed moving average of the observed NEAs in Fig. 3.3. Due to the multiple iterations at each set of parameters, the uncertainties of the modeled distributions' windowed moving averages are over an order of magnitude less than those from the observed distribution. Thus, we only consider the uncertainties from the observed distribution. In the next section, we include resurfacing from planetary close encounters in our model, and show the results in §5.3.2.

5.3 Resurfacing from Close Encounters

5.3.1 Methods

To include resurfacing from close encounters, we follow the "NEA model" described in Nesvorný et al. (2010), except that we model the spectral slopes instead of the S vs. Q-type classification. We gather all close encounters in the simulation and select a maximum resurfacing distance, r^*, in planetary radii (R_{pl}) inside which all asteroids will experience a complete resurfacing event. By considering only the maximum resurfacing distance, we simplify the complex behavior of asteroids during close encounters, but we capture the average required resurfacing distance for a population of asteroids. Additionally, by using planetary radii, we approximately scale for tidal gravity between all planets (Richardson, 1998). After an asteroid experiences a resurfacing encounter with a planet, we select its spectral slope from the S_{OC} distribution to estimate an unweathered surface. Then, the asteroid incrementally weathers each time step due to the solar wind using Eq. 5.1.

We simulate the spectral slopes vs. perihelion distribution for the range of space weathering timescales, τ_{SW0} = 10 kyr – 100 Myr, and for maximum resurfacing distances, $r^* = 1.5 - 20\ R_{pl}$. The range of space weathering timescales encapsulates those estimated through other studies with solar wind as the primary weathering agent (Brunetto et al., 2015). We extend the maximum range of the space weathering timescale to 100 Myr because better solutions were found at long timescales. The upper bound of maximum resurfacing distances of 20 R_{pl}, is distant enough that we should not expect any tidal effects to be relevant at that distance (Richardson, 1998; Walsh and Richardson, 2008).

5.3.2 Results

We plot the RMSE between the windowed moving averages of our simulated and observed distributions in Fig. 5.1 for the entire range of tested parameters. No set of parameters produce a windowed moving average that has $\geq 95\%$ of its points within the 95% confidence intervals of the observed distribution in Fig. 3.3. Also, there are no solutions that can match the steep slope of the linear regression at $q < 0.9$ AU. Thus, no combination of τ_{SW0} and r^* can provide a spectral slope vs. perihelion distribution that resembles the observed NEA distribution.

Fig. 5.2 shows the windowed moving average through the distribution of spectral slopes vs. perihelia and the linear regression at $q < 0.9$ AU for a simulation with τ_{SW0} = 100 Myr and $r^* = 3.4\ R_{pl}$. This combination of parameters represents the minimum RMSE for all tested parameters, with RMSE = 0.07 $\%/\mu$m. The windowed moving average has the same window size as the observed moving average of ± 0.1 AU. The uncertainties on the modeled windowed moving average are smaller than the width of the line. We also show the windowed moving average and the linear regression at $q < 0.9$ AU for the observed NEAs reproduced from Fig. 3.3.

The windowed moving average of the modeled distribution in Fig. 5.2 is visibly not a good fit for the observed spectral slope vs. perihelion distribution. There are large

deviations between the observed and modeled windowed moving averages, especially at low perihelia. Additionally, the slope of the linear regression at $q < 0.9$ AU is 0.170 ± 0.004 %/μm/AU, significantly different than the slope through the linear regression of observed NEAs (0.52 ± 0.21 %/μm/AU).

From these results, we can confidently conclude that resurfacing asteroids from close encounters with the terrestrial planets is not a dominant resurfacing mechanism for S and Q-type NEAs. However, this conclusion is contrary to many previous studies (e.g., Marchi et al. 2006a; Binzel et al. 2010; Nesvorný et al. 2010; DeMeo et al. 2014; Carry et al. 2016). In §5.5.1, we discuss how the correlation between close encounters and Q-type asteroids found in many of these studies is most likely due to confounding variables. In the next section, we investigate a model for resurfacing asteroids from thermally induced degradation, and show that it can provide a better fit to the spectral slope vs. perihelion distribution in the NEA region compared to resurfacing from close encounters.

5.4 Resurfacing from Thermally Induced Surface Degradation

5.4.1 Methods

It has been well established in the engineering literature that the growth rate of macroscopic cracks as a result of thermal fatigue goes as a power law with the induced cyclic stress (e.g., Janssen et al. 2002; Paris and Erdogan 1963; Le et al. 2014; Ritchie 2005). Measurements of such power laws are strongly dependent on the material size and shape, the size of the initial crack, and the environment, so they cannot be generalized to the case of asteroid surfaces. However, if we consider that the breakdown of boulders, production of regolith, and exposure of fresh material on these asteroids depends, in part, on the growth of many fatigue cracks in and across the surface, then it is not unreasonable to hypothesize that their convolved effect on the removal of space weathered surface material – or the resurfacing rate – also follows some power law with stress (a similar argument was also made in Marchi et al. 2009).

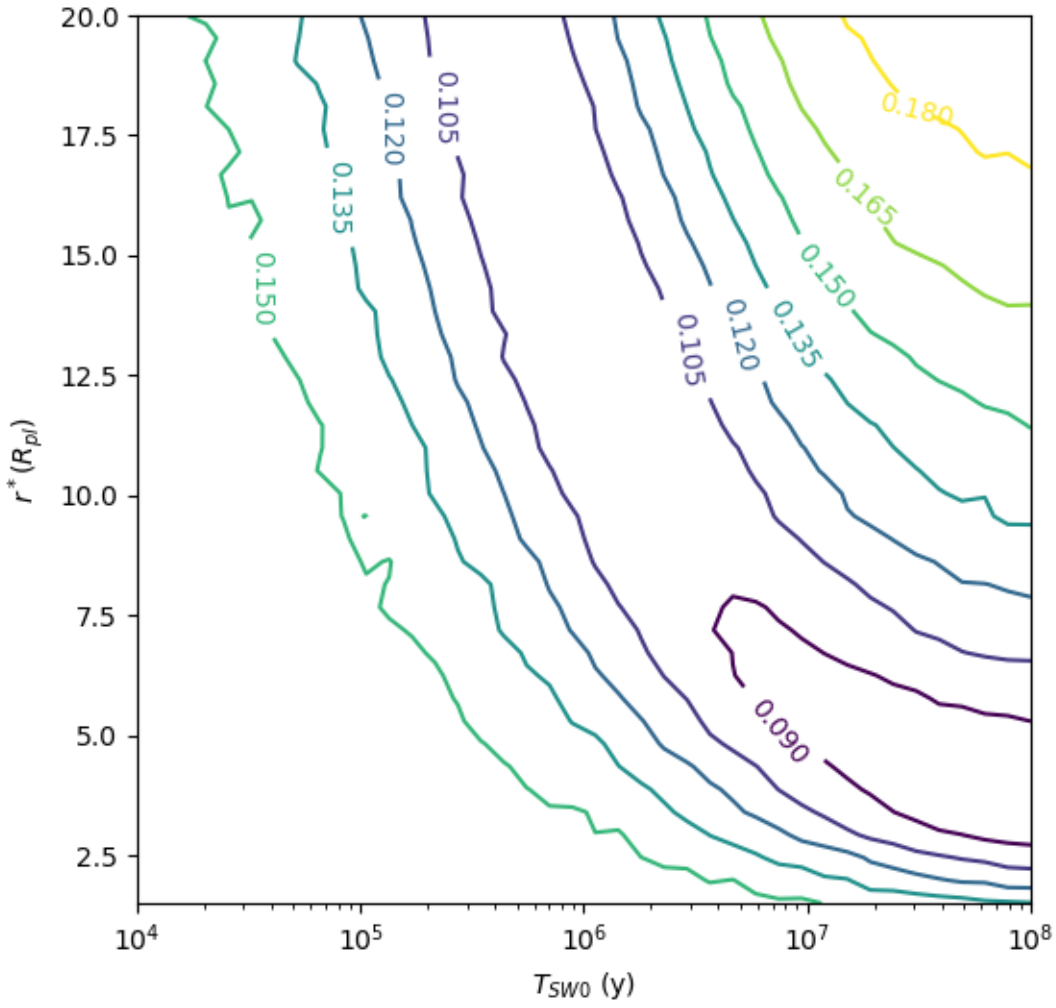

Figure 5.1. A contour plot of the Root Mean Square Error (RMSE) between the observed spectral slope vs. perihelion windowed moving average and the windowed moving average of the asteroids generated by resurfacing from close encounters with the terrestrial planets. No combination of the parameters τ_{SW0} and r^* can generate windowed moving averages with $> 95\%$ of the points within the 95% confidence intervals of the observed distribution in Fig. 3.3.

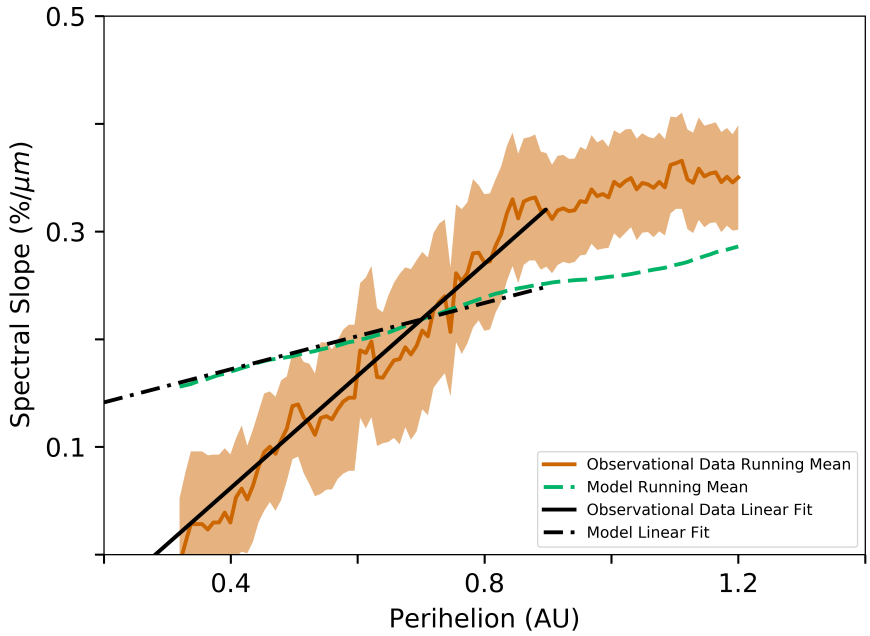

Figure 5.2. The windowed moving average and the linear regression at $q < 0.9$ AU of the asteroids' spectral slope vs. perihelion distribution from resurfacing due to close encounters with the terrestrial planets for the best fit solution of $\tau_{SW0} = 100$ Myr and $r^* = 3.4\ R_{pl}$. The dashed green line is the windowed moving average of the spectral slopes of the modeled asteroids. The uncertainty for the model windowed moving average is smaller than the thickness of the line. The solid orange line is the windowed moving average of the observed spectral slopes of the observed NEA asteroids and the shaded region is its uncertainty at a 95% confidence level (from Fig. 3.3). Both moving averages have a window size of ± 0.1 AU. The dashed-dotted black line is the linear regressions for $q < 0.9$ AU of the modeled asteroids, and the solid black line is the linear regressions for $q < 1$ AU of the observed NEA. The modeled asteroid windowed moving average does not match that of the observed data . Only 42% of the points on the modeled windowed moving average fall within the error bounds of the observed moving average. For clarity, the error bars for the slopes of the linear regressions are not shown (see §5.3.2 for the errors), but the slope of the modeled asteroids' linear regression does not match the steep slope of the observed and debiased linear regression at $q < 0.9$ AU.

Additionally, the thermally induced stress in an object is directly proportional to the amplitude of its diurnal temperature range (e.g. Molaro et al. 2015). For fast rotating bodies (with periods less than one Earth day), such as most asteroids, the amplitude of its diurnal temperature range is primarily controlled by the solar distance (Marchi et al., 2009; Molaro et al., 2017). Thus, we make the reasonable assumption that the total rate of surface degradation on an asteroids surface has a power law relationship with the solar distance.

For resurfacing to occur from thermal effects, the thermal cycling would cause cracks to form in boulders on the surface of the asteroid, and those growing cracks would eventually break off sections of the boulders' surfaces. Then, any resulting debris or regolith would need to be moved across the surface or completely removed from the asteroid to expose the underlying unweathered material (see §5.5.2 for further discussion). Because space weathering only affects the upper microns of the regolith grains on an asteroid (Noguchi et al., 2011), any location where breakdown and subsequent surface movement or removal occurs will expose completely unweathered material. Additionally, the bulk spectral slope of an asteroid is a combination of the spectral slopes across all arbitrary subdivisions of the observed hemisphere. Thus, as small sections are resurfaced, the bulk spectral slope of the asteroid is lowered. However, if a highly weathered section is resurfaced, there will be a larger change in the bulk spectral slope than if a relatively unweathered section is resurfaced. Thus, the rate of change of an asteroid's bulk spectral slope from thermally induced resurfacing should approximately depend on the current bulk spectral slope of the asteroid, assuming that the spectral slope doesn't greatly change across the surface of the asteroid.

In our model implementation, we assume that the averaged rate of change in the bulk spectral slope due to the resurfacing of small sections across the body linearly depends on the current bulk spectral slope of the asteroid. Specifically, we calculate the rate of change of the spectral slope as:

$$\left(\frac{d\mathrm{S}}{dt}\right)_R = \frac{1}{\tau_R}\left(\mathrm{S_{OC}} - \mathrm{S}\right). \tag{5.3}$$

where τ_R is the e-folding resurfacing timescale. Eq. 5.3 satisfies the need for a more rapid rate of decrease in the spectral slope for more highly weathered asteroids. We also found that the exact formulation of the rate of change in the spectral slope due to resurfacing does not greatly alter our results.

We then increment the spectral slope, S, at each time step using Eqs. 5.1 and 5.3. Due to our relatively large timestep of 10^4 y, an incremental change in spectral slope can become large when τ_{SW} or τ_R become small. However, for a given τ_{SW} and τ_R, there is a spectral slope (S^*) between $\mathrm{S_{OC}}$ and $\mathrm{S_{max}}$ where the space weathering and resurfacing rate cancel each other. By setting Eq. 5.1 equal to the negative of Eq. 5.3, we find

$$S^* = \frac{\tau_R \mathrm{S_{max}} + \tau_{SW} \mathrm{S_{OC}}}{\tau_R + \tau_{SW}}. \tag{5.4}$$

We create a constraint that if an incremental step in spectral slope would cross S^*, then we set $S = S^*$.

Following our argument at the beginning of this section, we let the resurfacing timescale, τ_R, scale with the solar distance, r, raised to some unknown power k:

$$\tau_R = \frac{\tau_{R0}}{(1\mathrm{AU})^2} \frac{P}{\oint r^{-k} dt} = \frac{\tau_{R0}}{(1\mathrm{AU})^2} \frac{2\pi a^k \left(1-e^2\right)^{k-3/2}}{\oint \left(1+e\cos\left(f\right)\right)^{k-2} df}, \tag{5.5}$$

where f is the true anomaly, P is the orbital period, and τ_{R0} is the resurfacing timescale at $a = 1$ AU and $e = 0$. As in Eq. 5.2, the integral is taken over one orbit. The integral in Eq. 5.5 cannot be solved analytically in general, but it can be solved numerically and rapidly with the use of Gaussian hypergeometric functions.

Due to the limited constraints on thermally induced surface degradation, we have 3 relatively unconstrained parameters to explore: the space weathering and resurfacing timescales for a circular orbit at 1 AU, τ_{SW0} and τ_{R0} respectively, and the power law exponent controlling the dependence of the resurfacing timescale on solar distance, k. To simplify the parameter space, we searched over 10 logarithmically spaced values of space weathering timescales from $\tau_{SW0} = 10$ kyr – 10 Myr, and vary $\tau_{R0}/\tau_{SW0} = 10^{-1} - 10^8$ and $k = 1.5 - 35$. We use the parameter τ_{R0}/τ_{SW0} instead of τ_{R0} because

comparing the plots with different values of space weathering timescales (τ_{SW0}) is more intuitive.

5.4.2 Results

Fig. 5.3, shows three contour maps of the RMSE between the windowed moving averages of the modeled and observed spectral slope vs. perihelion distributions. The top, middle, and bottom plots are calculated with $\tau_{SW0} = 10$ kyr, 100 kyr, and 1 Myr respectively. We also shade acceptable solutions, where $\geq 95\%$ of the points on the windowed moving average of the modeled distribution are within the 95% confidence intervals of the observed distribution. We find a small range of acceptable solutions for $\tau_{SW0} = 10$ kyr with $k \approx 5 - 10$, and $\tau_{R0}/\tau_{SW0} \approx 2 - 50$. For $\tau_{SW0} = 100$ kyr and $\tau_{SW0} = 1$ Myr, we find a large range of solutions with $k \gtrsim 6$ and $\tau_{R0}/\tau_{SW0} \gtrsim 5$, with no upper bound in the tested parameter space. Considering all 10 tested values of τ_{SW0}, we find acceptable solutions with $\tau_{SW0} \lesssim 5$ Myr, $k \gtrsim 5$ and $\tau_{R0}/\tau_{SW0} \gtrsim 2$. We choose not to extend the parameter space for k and τ_{R0}/τ_{SW0} because higher values produce increasingly higher RMSEs, and exceedingly high values of k are likely not physical.

Fig. 5.4, shows the windowed moving average and the linear regression at $q < 0.9$ AU of the spectral slope vs. perihelion distribution for $\tau_{SW0} = 22$ kyr, $\tau_{R0}/\tau_{SW0} = 7$ ($\tau_{R0} \approx 150$ kyr), and $k = 8$. This combination of parameters represents the minimum RMSE for all tested parameters, with RMSE = 0.018 $\%/\mu$m. As in the Fig. 5.2, the windowed moving average has a window size of ± 0.1 AU, and the uncertainty of the modeled distribution is smaller than the thickness of the line. We also show the windowed moving average and the linear regression at $q < 0.9$ AU for the observed NEAs.

The parameters in Fig. 5.4 provide a very good fit to the spectral slope vs. perihelion distribution. The slope of the linear regression at $q < 0.9$ AU is 0.4656 ± 0.0005 $\%/\mu$m/AU, which is also consistent with the observed distribution of NEAs

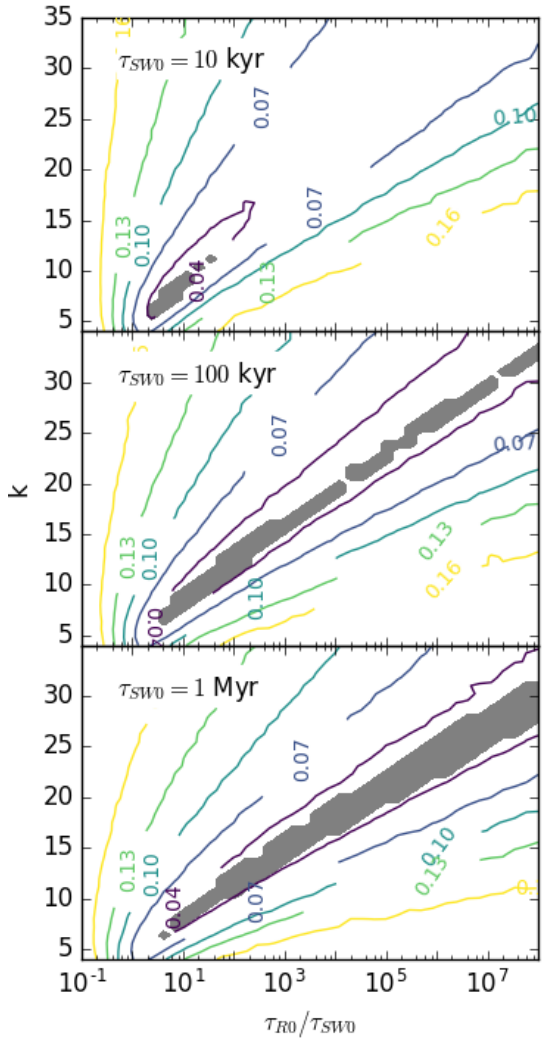

Figure 5.3. Three contour plots showing the RMSEs between the windowed moving averages of the spectral slope vs. perihelion distribution of the perihelion threshold resurfacing model and the observed and data. The top, middle, and bottom frames show the RMSEs for the space weathering timescales of $\tau_{SW0} = 10$ kyr, 100 kyr, and 1 Myr respectively. The shaded regions correspond to solutions where $> 95\%$ of the points on the modeled windowed moving average fall within the error bounds of the observed moving average. For all tested values of τ_{SW0}, the parameters that provide acceptable solutions are $\tau_{SW0} < 5$ Myr, $k \gtrsim 5$, and $\tau_{R0}/\tau_{SW0} \gtrsim 2$.

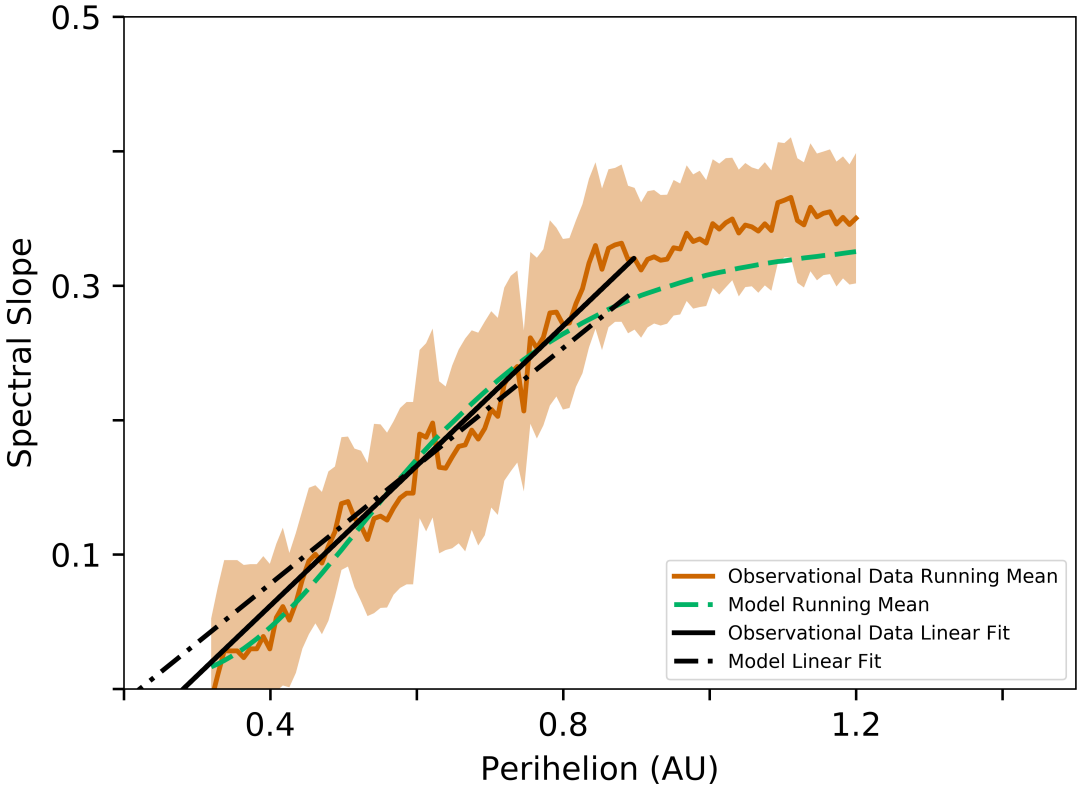

Figure 5.4. Identical to Fig. 5.2 except showing the results for the solar distance-dependent resurfacing model for the parameters: $\tau_{SW0} =$ 22 kyr, $\tau_{R0}/\tau_{SW0} = 7$ ($\tau_{R0} \approx 150$ kyr), and $k = 8$. These parameters represent the smallest RMSE between the windowed moving averages of the modeled and observed spectral slope vs. perihelion distributions of NEAs. We found that 100% of the points on the modeled windowed moving average fall within the error bounds of the observed moving average. The slope of the linear regression at $q < 0.9$ AU of the modeled asteroids also falls within the error bounds of slope of the linear regression for the observed and debiased data (see §5.4.2 for details).

(0.52 ± 0.21 %/μm/AU). All of the acceptable solutions, which are shaded in Fig. 5.3, provide similar fits as the one shown in Fig. 5.4, and are able to match the slope of the linear regressions at $q < 0.9$ AU of the observed distribution of NEAs. When comparing Figs. 5.4 and 5.2, resurfacing asteroids from thermally induced surface degradation can provide a much better explanation for the decrease in spectral slopes at low perihelia.

The large region of acceptable solutions supports solar distance dependent resurfacing as a natural explanation for producing the spectral slope vs. perihelion trend. However, a robust and quantitative conclusion for whether resurfacing from thermally induced degradation as a solar distance dependent resurfacing process is occurring on the surface of asteroids, may require precise knowledge of all three parameters –τ_{SW0}, τ_{R0}, and k. This work – specifically Fig. 5.3 – builds a functional relationship between these three parameters, and future work can help constrain the region of acceptable solutions. We discuss these results and additional qualitative and quantitative evidence for thermally induced surface degradation in §5.5.2.

5.5 Discussion

By modeling the population of NEAs, we were able to test the effectiveness of resurfacing S and Q-type asteroids from either tidal effects during close encounters with the terrestrial planets or thermally induced degradation at low solar distances. We find that resurfacing from close encounters cannot adequately match the observed spectral slope vs. perihelion distribution, and that a thermally induced degradation process modeled as a solar distance dependent resurfacing model provides a much better fit. In this section we discuss both results. We show how previous studies supporting the close encounter mechanism are most likely confounded by an underlying distribution of less weathered asteroids at low perihelion. We also consider the acceptable solutions of the thermally induced surface degradation models and show that they agree with the process of thermal fracture on the surface of an asteroid.

5.5.1 Resurfacing from Close Encounters

Resurfacing asteroids from close encounters with the terrestrial planets cannot generate a spectral slope vs. perihelion distribution that is consistent with the observed distribution. However, previous studies by Binzel et al. (2010) and Carry et al. (2016) used the correlation between Q-type asteroids and recent low Mean Orbital Intersection Distances (MOIDs) and low close encounter distances with the terrestrial planets instead of relying on the spectral slopes. Here, we argue that the correlations in these studies are confounded by the higher fraction of Q-types at low perihelia created by another resurfacing mechanism (such as thermally induced surface degradation).

Binzel et al. (2010) cloned all observed Q and S-type NEAs and MCs, six times and conducted backwards simulations of all asteroids and clones. Over their 0.5 Myr integrations, they selected the lowest MOID from all timesteps for each asteroid and its clones, which we refer to at the minimum MOID. They found that all Q-type asteroids had a minimum MOID within the lunar distance, while this was not true for the S-types. Using binomial statistics, they found a probability of 0.9% that all Q-types would have a minimum MOID within the lunar distance if they were randomly sampled from the distribution of their population of S and Q-type asteroids. Even though Q-type asteroids were later observed in the NEA and MC regions that do not have a minimum MOID within the lunar distance (DeMeo et al., 2014), this statistical argument still suggests a strong correlation between Q-type asteroids and a low minimum MOID with Earth.

Carry et al. (2016) used observations from the Sloan Digital Sky Survey, and conducted similar backwards simulations for NEAs and MCs with about 100 clones for each asteroid. They counted the number of close encounters of each asteroid and all of its clones with Venus, Earth, and Mars. They found that Q-type asteroids have more resurfacing encounters than S-types for Venus and Earth, but no difference between S-types and Q-types for encounters with Mars. They did not attempt to

correlate each Q-type asteroid to a recent resurfacing event with a terrestrial planet, but they did conclude that Q and S-type asteroids are dynamically different and that Q-types tend to have more close encounters with Earth and Venus.

Using the data from the supplementary material of Binzel et al. (2010), we found that 100% of all asteroids with $q < 0.9$ AU have a minimum MOID within the lunar distance of Earth, including 13 Q-type asteroids. Therefore, there is no significance that the Q-types at $q < 0.9$ AU have low minimum MOIDs because all asteroids in their study at $q < 0.9$ AU have low minimum MOIDs. If we remove these asteroids due to their lack of significance, and also remove the MCs from the calculation because they are unable to have low MOIDs with Earth, we find that the fraction of asteroids with $0.9 < q < 1.3$ AU with low minimum MOIDs is 30/42. The probability that all 7 Q-types with $0.9 < q < 1.3$ AU have a minimum MOID within the lunar distance if they are randomly sampled is $(30/42)^7 \approx 9\%$, much less significant than 0.9%.

Additionally, the conclusion that Q-types tend to have more close encounters with Earth and Venus, on average, from Carry et al. (2016) is certainly correct. However, it is difficult to gain any insight into whether close encounters have actually resurfaced these Q-types unless we consider similar populations of S and Q-type asteroids. The majority of asteroids that Carry et al. (2016) considered for close encounters with Earth and Venus were MCs, and the majority of MCs that they observed are S-types. Q-type asteroids only comprised a significant fraction of their population for the NEAs. By including MCs that are heavily weighted towards S-types and that cannot have close encounters with Earth or Venus, the cumulative number of close encounters of S-type asteroids with Earth and Venus will naturally grow more slowly than Q-types, even if both S and Q-type NEAs have the same average number of close encounters. If the MCs were removed from the analysis, it is unclear if the remaining Q-types NEAs would have more close encounters with Earth and Venus than compared to S-type NEAs, and the significance of their results would certainly decrease.

Furthermore, Nesvorný et al. (2010) found that resurfacing from close encounters with the terrestrial planets could explain the overall number of Q-types in the NEA population but could not match their orbital distribution. They noticed a bimodal distribution of Q-type asteroids at semi-major axes $a \lesssim 1$ AU and $a \gtrsim 1.5$ AU, which has since been smoothed out with more observations (DeMeo et al., 2014). However, they found that they were not able to match both populations simultaneously. In particular, when they used a space weathering timescale that scaled with solar wind irradiation ($1/r^2$), they were unable to match the low a (and low q) population, consistent with our inability to match the very low spectral slopes at low perihelia by resurfacing from close encounters.

We conclude that tidal effects from close encounters with the terrestrial planets are not a dominant resurfacing mechanism for S and Q-type asteroids for the following reasons: (1) close encounters are unable to generate the observed spectral slope vs. perihelion distribution for any reasonable range of space weathering timescales and maximum resurfacing distances, and (2) the previous correlations between Q-type asteroids and low MOIDs or close encounters with the terrestrial planets in backwards simulations can be explained by a larger fraction of Q-type asteroids at low perihelion. It is possible that very close encounters with the terrestrial planets can still resurface some asteroids, but those events do not appear to play a large role in the population of S and Q-type asteroids. In the next subsection, we discuss the results from our thermally induced surface degradation model, which can provide a much more consistent fit to the observed spectral slope vs. perihelion distribution of NEAs.

5.5.2 Resurfacing from Thermally Induced Surface Degradation

In §5.4.1, we cite evidence that suggests the breakdown of the surface of an asteroid due to thermal cycling can be well represented by a power law. However, we did not place any limits on the power law relationship, and allowed both τ_{R0} and k to be unconstrained parameters. From the acceptable solutions of our solar distance

dependent resurfacing model, we conclude that the process of thermally induced surface degradation produces a good representation of the observed spectral slope vs. perihelion distribution, only if our acceptable solutions are consistent with the process of thermal fracture. Here, we argue that the range of acceptable solutions are consistent, and that other observations and modeling studies qualitatively support the process of thermal breakdown at low perihelia.

The acceptable values of $\tau_{SW0} \lesssim 5$ Myr generally fit with experimental results. Interestingly, this upper bound is barely consistent with the range of space weathering timescales at $a = 1$ AU and $e = 0$ required for YORP spin-up and failure to be a primary resurfacing mechanism for asteroids at small sizes found in Chapter 4, §4.1. If a solar distance dependent resurfacing process is the cause of the low spectral slopes at low perihelion, it could suggest that the YORP effect could be resurfacing asteroids more often than only at the fission spin rate, as assumed in Chapter 4. It could also mean that another process, such as impacts followed by seismic shaking, may be the dominant process for resurfacing asteroids at small sizes.

The acceptable values of k can provide additional insight. In our model, the timescale of resurfacing scales as $\tau_R \propto r^k$ with $k > 5$, and the best solutions found at lower values of k. This constraint is not surprising, as k needs to be larger than 2 to overcome the increase in the rate of space weathering with decreasing perihelion, which is controlled by the amount of solar insulation. To consider how k compares with the process of thermally induced degradation and with previous studies, it is useful to estimate the dependence of the thermally induced resurfacing timescale from our model on the induced thermal stress. From the arguments in §5.4.1, we assume that the resurface timescale goes as a power law with both thermal stress and solar distance. Furthermore, Molaro et al. (2017) give the relationship between induced thermal stress and solar distance: $\Delta\sigma_s \propto r^{-1.71}$. Thus, using $\tau_R \propto r^k$, we find

$$\tau_R \propto \Delta\sigma_s^m = \Delta\sigma_s^{k/-1.71} \tag{5.6}$$

where $m \lesssim -3$ to match the range of acceptable solutions in our model, and the best fit solutions are around $m \approx -4.7$.

One approach that has been used in the literature to estimate thermally induced degradation rates is to measure the rate of crack growth for a given boulder size and initial crack length based on induced stress. Migliazza et al. (2011) estimated the dependence of the rate of stable crack growth in a block of marble on the amplitude of induced thermal stress using the Paris law (Paris and Erdogan, 1963): $da/dN \propto \Delta\sigma_s^{3.84}$, where a is the crack length and N is the number of thermal cycles. Delbo et al. (2014) used this result, along with experimental measurements of thermally induced crack growth through meteorites in dry air, to estimate the rate of regolith production on asteroid surfaces. Our parameter would be consistent with that from Migliazza et al. (2011), if we were to assume that the rate of crack growth of a single macroscopic crack is inversely proportional to the resurfacing timescale of an asteroid ($da/dN \propto 1/\tau_R$). However, there are a number of critical issues with making this assumption, which are discussed extensively in Section 4 of Molaro et al. (2017). For one, the results from Migliazza et al. (2011) and Delbo et al. (2014) only quantify the stable regime of crack growth, neglecting the time it takes to form and grow a microcrack into a macroscopic feature. For an asteroid first undergoing strong thermal cycling, many macroscopic cracks may be present on the surface and the results of Delbo et al. (2014) may be accurate. However, to account for the complete and continuous resurfacing that is occurring at low perihelia, it is necessary to account for the total fatigue lifetime of the surface. This period can be orders of magnitude longer than that of stable crack growth (Janssen et al., 2002), suggesting that these models underestimate the total lifetime of objects undergoing breakdown, and thus would not produce the same scaling law as our resurfacing rate. Most importantly, thermally induced breakdown occurs over a range of geomorphic scales, and thus a thermally induced resurfacing rate should reflect the convolved effect of the thermally induced changes to the landscape as a whole. Since da/dN is crack-size and block-size dependent, the behavior it describes is not representative of such a complex

geomorphological process. Ultimately, we argue that the scaling law inferred from our analysis describes something different than the Paris law.

A given value of τ_{R0} is difficult to translate into a timescale of a physical alteration of the surface of an asteroid because τ_{R0} only considers the spectrum of the entire asteroid. However, the rate of regolith production due to thermally induced surface degradation may be closely related. Recent studies of the properties of regolith particles returned from (25143) Itokawa by the JAXA Hayabusa spacecraft have attempted to predict the primary formation process of regolith on Itokawa. Michikami et al. (2018) argued that the axial ratio and shape distribution of the regolith fragments are consistent with being the products of impact fragments and not thermal fatigue. Tsuchiyama et al. (2011) argued that the well-rounded profiles of the regolith fragments could be due to abrasion from seismic-induced grain motion, but Hazeli et al. (2018) argued that the well-rounded profiles we consistent with thermal fatigue.

Unfortunately, our range of acceptable results cannot help determine which mechanism of regolith production is the most dominant on Itokawa. Depending on the value of τ_{R0}, the thermal breakdown rate at Itokawa's perihelion of about 1 AU could create more or much less regolith compared to that generated by impacts. If a consensus on the presence or production rate of regolith on the surface of Itokawa is reached, we could place a direct constraint on τ_{R0} and greatly shrink the parameter space of acceptable values for τ_{SW0} and k that would be necessary for thermally induced surface degradation to create the spectral slope vs. perihelion trend at $q \lesssim 0.9$ AU. Additionally, two spacecraft missions, OSIRIS-REx and Hyabusa2, are expected to return more regolith samples to Earth in the next five years. Even though these asteroids have different mineralogies than S and Q-type asteroids, studies of their regolith may provide important insights on the presence and rate thermal breakdown on the surface of asteroids.

There are also separate observations and modeling results suggesting that thermal processes can drastically affect asteroids at low perihelia. The asteroid (3200) Phaethon has a perihelion of 0.14 AU, and has experienced unexpected brightening

during multiple perihelion passages (Jewitt and Li, 2010; Li and Jewitt, 2013). The brightening is associated with an impulsive release of dust particles near its perihelion (Jewitt and Li, 2010). Due to the high temperatures reached on Phaethon's surface, near surface water ice is not expected to survive. Thus, the most plausible explanation is that thermal fracture of the surface creates dust which is then removed by either the residual velocities of crack growth or through radiation pressure sweeping (Jewitt, 2012).

Additionally, there is evidence that asteroids are completely disrupted at very low perihelia. The model of Granvik et al. (2016) was able to match the distribution of NEAs by instantaneously removing any asteroids from the simulation if they fell below a threshold perihelion, $q \sim 0.05 - 0.2$ AU. They did not directly model the disruption process, but did suggest 3 possible mechanisms: (1) thermal cracking and removal of grains from radiation pressure, (2) the spin up of asteroids to the point of disruption from the YORP effect (or a similar sublimation driven YORP effect; see Steckloff and Jacobson 2016), and (3) the sublimation of volatiles present inside the asteroid causing it to blow apart. If thermally induced surface cracking or degradation and the removal of grains from radiation pressure is the primary cause of asteroid resurfacing and disruption at low perihelia, it paints the picture that thermal processes first disrupt the surface of asteroids at a perihelion of $q \lesssim 0.9$ AU. Once the asteroid reaches a perihelion of $q \sim .05 - .2$ AU, thermal fracture becomes a runaway process and quickly disrupts the entire asteroid.

As suggested by Jewitt (2012) and Granvik et al. (2016), the removal of dust via radiation pressure sweeping may play an important role in resurfacing and disrupting asteroids. Lofted particles can only be pushed away from an asteroid when the acceleration due to radiation pressure becomes larger than the acceleration due to the gravity of the asteroid. If the residual velocities from thermally induced surface cracking lofts particles off the surface of the asteroid, radiation pressure may push sufficiently small particles away from the asteroid (Jewitt, 2012). We note that simple dust removal (i.e. without any surface degradation) would not be sufficient to give

a small asteroid an unweathered spectrum because the surfaces of boulders can be weathered just as effectively as loose material (e.g., Ishiguro et al. 2007). Thus, for an asteroid to have a completely unweathered spectrum, the surfaces of boulders on the asteroid would need to be disrupted to expose unweathered material.

Conversely, surface degradation, followed by overturn or mass movement, without any dust removal, could resurface an asteroid, but it would naturally be a self-limiting process. The fast resurfacing timescale, $\tau_{R0} \approx 150$ kyr, of our best fit solution, shown in Fig. 5.4, would suggest that the surfaces of asteroids at the Earth's orbit are broken down much more rapidly than the lifetime of NEAs (~ 10 Myr; Gladman 2000). Other acceptable solutions permit significantly higher values of τ_{R0}, but asteroids with lower perihelia would still experience surface degradation on a much faster timescale than their lifetimes. If the resulting surface degradation does not remove material from the asteroid, then a thick regolith layer would rapidly form and shut off further thermally induced resurfacing. For our model to accurately describe the distribution of spectral slopes at low perihelion, we require some level of dust removal to occur at least at lower perihelia. Fortunately, this process appears to be reasonable (e.g., Jewitt 2012; Granvik et al. 2016.

If the weathered material is being removed from the surface in large amounts, we would expect to see a brightening of the asteroid shortly after the dust is released (Jewitt et al., 2015). However, no S or Q-type asteroids with low perihelia have been seen to show any cometary features (Jewitt, 2013). These observations suggest that (1) the removal of surface material is an ongoing process that is occurring very slowly ($\lesssim 1$kg s^{-1}; Jewitt 2013), (2) the removal of material happens only periodically and wasn't observed, or (3) the asteroids are somehow being resurfaced without the removal of surface material. It is puzzling that asteroids appear to be completely disrupted at low perihelion (Granvik et al., 2016), but we have only seen evidence of one asteroid (3200 Phaethon) losing mass in that region (Jewitt et al., 2015).

From the above arguments, we cannot conclusively show that thermally induced surface degradation is resurfacing asteroids at low perihelia. However, it is consistent

with other observations and our basic understanding of thermal fracture. Additionally, other resurfacing processes that could occur at low perihelia cannot explain the rapid change in resurfacing rates that is needed to match the observed spectral slope vs. perihelion distribution. YORP driven spin-up and failure has been cited as a possibility for resurfacing and disrupting asteroids at low perihelion (Nesvorný et al., 2010; Granvik et al., 2016). However, if space weathering is dominated by the solar wind, both the rate of spin-up and failure from the YORP effect (or a sublimation driven YORP effect) and the space weathering rate should identically scale with the amount of solar insolation (see e.g., Chapter 4, §4.1), resulting in no orbital dependence on the spectral slopes of asteroids.

Granvik et al. (2016) also suggested that the sublimation of volatiles inside asteroids could cause them to blow apart. It could be possible that a similar sublimation of volatiles in the near surface could be breaking apart the surface of S and Q-type asteroids at a slightly higher perihelia than where these asteroids are disrupted. However, S and Q-type asteroids likely experienced heating to 600–960°C (Keil, 2000), most likely removing the majority of water content from the entire body and making a sublimation driven resurfacing process unlikely.

5.5.3 Testable Predictions of Thermally Induced Surface Degradation

In the previous subsection, we discussed how the process of thermally induced surface degradation is a viable mechanism for resurfacing asteroids at low perihelia. Here we list a few testable predictions from our model:

1. The primary testable result from this study is that the timescale of thermal degradation must scale relatively strongly with solar distance and induced thermal stress. We estimate that the timescale of thermal degradation scales by r^k where $k > 5$, and by $\Delta\sigma_s^m$ where $m < -3$, with the best fit solutions around $k \approx 8$ and $m \approx -4.7$. The value of m could be potentially measured through experimental studies of thermally induced surface degradation with a focus on the

entire breakdown process, from crack initiation to failure and disaggregation. These experiments would also need to consider the nature of the breakdown in a vacuum and in objects of different sizes. Finally, the changes in the bulk spectral measurements due to breakdown would need to be measured.

2. S and Q-type asteroids at low perihelion may have high thermal inertia (potentially higher than those with perihelia above ≈ 0.9 AU) suggesting that they have lost loose material, or that the asteroid is blocky enough to allow significant thermal stresses to build up.

3. If asteroids are resurfaced through thermal effects causing the removal of material, evidence for dust lofting off these asteroids may be observable – even though it was not seen in Jewitt (2013). In particular, Q-types and S-types with low spectral slopes at very low perihelia would be good candidates for observations. However, the resurfacing and removal process needed to change the spectral properties of these asteroids does not require large amounts of material loss, and may be difficult to observe except in extreme cases (e.g., a total disruption like in Granvik et al. 2016).

4. Thermally induced degradation should be most effective where there is a large temperature change. If resurfacing is connected to thermal effects, then it should be focused in the equatorial regions of asteroids with obliquities near 0° or 180°. If observational geometries allow for an observation biased toward the polar region of one of these asteroids, our model would predict that the asteroid's spectrum would appear more weathered and have a higher spectral slope.

5. Finally, we expect any regolith that is present on asteroids with low perihelia ($q \lesssim 0.9$ AU) to be predominantly created by thermally induced degradation. Whether that regolith will look similar to the regolith on Itokawa is unclear (Tsuchiyama et al., 2011; Michikami et al., 2018; Hazeli et al., 2018), but asteroids at a lower perihelia would have a more pronounced effect.

5.6 Conclusion

The spectral slopes of S and Q-type asteroids are a strong indicator of the amount of space weathering that has accumulated on their surfaces. Asteroids with lower spectral slopes have most likely been resurfaced recently, and the distribution of these low slopes gives us a powerful constraint to determine which potential resurfacing processes are the most dominant. There are two primary trends in the distribution of spectral slopes: (1) a decrease in spectral slope with decreasing perihelion, and (2) a decrease in the spectral slope with decreasing size. In this study, we tested whether close encounters with the terrestrial planets or thermally induced surface degradation could match the observed spectral slope vs. perihelion distribution. We limited our investigation to only the spectral slope vs. perihelion trend, as the trends are most likely created by different resurfacing processes, and the spectral slope vs. size trend was used as a constraint in Chapter 4.

We found that resurfacing from close encounters could not reproduce the observed spectral slope vs. perihelion distribution for any reasonable combination of parameters. We also argued that previous results supporting close encounters as a viable resurfacing mechanism were due to confounding variables, as the correlation of Q-type asteroids' past orbits with the terrestrial planets are confounded by the higher fraction of Q-type asteroids at low perihelia, most likely created by another resurfacing mechanism.

We found that resurfacing from thermally induced degradation could accurately recreate the observed spectral slope vs. perihelion distribution. We found acceptable solutions with a space weathering timescale for a circular orbit at 1 AU of $\tau_{SW0} \lesssim 5$ Myr, a ratio of the resurfacing timescale to the space weathering timescale of $\tau_{R0}/\tau_{SW0} \gtrsim 2$, and a power law exponent controlling how strongly the resurfacing rate scales with solar distance of $k \gtrsim 5$.

Our acceptable solutions for the power law scaling factor are broadly consistent with the process of thermally induced surface degradation and thermal fatigue. Ad-

ditionally, other evidence, such as the unexpected brightening of asteroid (3200) Phaethon during its low perihelion passages (Jewitt, 2012) and the complete disruption of asteroids at very low perihelia (Granvik et al., 2016), can also be explained by thermally induced degradation followed by the removal of grains. While more work needs to be done to better constrain the process of thermal breakdown on the surface of asteroids, our work, and specifically Fig. 5.3, builds a functional relationship between the timescales of space weathering and thermally induced degradation, and the scaling law of thermal degradation which are required to resurface asteroids from thermal effects.

6 THE CREATION RATE OF ASTEROID PAIRS

6.1 Introduction

Two asteroids with similar heliocentric orbits, but not gravitationally bound together, were found throughout the main belt by Vokrouhlický and Nesvorný (2008). Even when considering the variation in the number density of asteroids due to resonances and large asteroid families, these "asteroid pairs" have orbits that are more similar than is expected by random chance (Vokrouhlický and Nesvorný, 2008; Pravec and Vokrouhlický, 2009). Using the orbits of 370,000 asteroids, Vokrouhlický and Nesvorný (2008) found ∼60 statistically significant pairs by measuring an orbital similarity distance between their osculating orbital elements and comparing them to the orbital similarity distribution generated by asteroids with randomly sampled orbits. Additionally, Rożek et al. (2011) compared ∼372,000 orbits using mean orbital elements and found ∼100 pairs, with a small dependence on the metric used to calculating the orbital similarity between two asteroids. Rożek et al. (2011) also found that by using the mean orbital elements, the orbital similarity distance between many pairs significantly decreased.

After backwards N-body integrations of asteroid pairs, many were found to have close approaches to one another with low separation velocities (Vokrouhlický and Nesvorný, 2008, 2009; Pravec et al., 2010). The common history of these asteroids strongly suggests that they formed from a single asteroid or from a disassociated binary. Vokrouhlický and Nesvorný (2008) proposed that the pairs may be formed by 1) collisional disruption, 2) the radiative torque due to the irregularities on the asteroid, known as the Yarkovsky-OKeefe-Radzievski-Paddack (YORP) effect (Rubincam, 2000; Bottke et al., 2006), causing the asteroid to spin up and fission, or 3) the disassociation of unstable asteroid binaries.

Pravec et al. (2010) conducted observations on 35 asteroid pairs and found that all observed pairs had a mass ratio below about 0.2. For binary asteroids formed by rotational fission, the free energy, defined as the potential plus kinetic energy, minus the self-potentials of both objects, can help determine the outcome of the system (Pravec et al., 2010). A system with a mass ratio of $\gtrsim 0.2$ has positive free energy and can therefore escape due to internal dynamics. However, systems with mass ratios $\lesssim 0.2$ have negative free energy and cannot become unbound. Additionally, Pravec et al. (2010) found that primary asteroids spin more slowly as the mass ratio of the pair increases. If an asteroid pair is formed by rotational fission, a larger mass ratio will cause the secondary to carry a greater fraction of the angular momentum away from the system, slowing the spin rate of the primary. They also showed that the relationship between the mass ratio of the system and the primary's spin rate agrees exceptionally well with formation by a rotational fission event. Both of these attributes of asteroid pairs give very compelling evidence that most are formed by YORP-induced rotational fission followed by a gravitational escape of the secondary.

Another characteristic of asteroid pairs is their relatively young lifetimes, as most pairs have separated less than one million years ago (Vokrouhlický and Nesvorný, 2008; Pravec et al., 2010). These short lifetimes suggest that processes such as chaos, resonances, and a thermal radiation force causing a semimajor axis drift, known as the Yarkovsky effect (e.g., Bottke et al. 2006), can quickly disassociate asteroid pairs. Furthermore, they suggest that asteroid pairs must be created relatively rapidly to replace those that are disassociated. Assuming that the population of asteroid pairs is in a steady state, an estimate of either the rate of disassociation or the rate of asteroid pair creation can aid in the prediction of the other.

In this study, we build a population of asteroid pairs in the inner main belt. We model the evolution rate of each member of the pair beginning at the same location and with slightly different velocities. From the end state of these simulations, we build an orbital similarity distribution of all modeled asteroids in the inner main belt and compare it to the observational distribution . By changing the rate of pair

creation, we alter the modeled orbital similarity distribution, and we find a range of pair creation rates which sufficiently match the observational distribution.

An estimation of the pair creation rate can give important insights in the process of YORP-induced rotational fission. We compare our results of the pair creation rate to those from previous theory-driven YORP evolution models (Jacobson and Scheeres, 2011; Jacobson et al., 2016). The relative difference between these timescales of the pair creation rate can place constraints on the process of YORP evolution and fission, which we can then also compare to previous YORP-evolution models (Marzari et al., 2011; Jacobson and Morbidelli, 2014; Bottke et al., 2015; Cotto-Figueroa et al., 2015; Graves et al., 2018), We can also directly calculate the effect of the rate of rotational fission on the size frequency distribution of the main belt, providing a separate estimate from the one in Jacobson and Morbidelli (2014). We discuss and compare our results with previous studies in §6.5.

The rest of the chapter is organized as follows. In §6.2, we build the orbital similarity distribution of inner main belt asteroids which serves as the primary constraint for modeling. We remove asteroid pairs from the distribution that could not be formed by YORP. In §6.3, we outline our model to generate the orbital similarity distribution of inner main belt asteroids given a pair creation rate. We use an N-body simulation to track the evolution and disassociation of asteroid pairs. In §6.4, we show the results of our model.

6.2 Inner Main Belt Asteroid Pairs Created by YORP Fission

In this study, we use the Drummond orbital similarity metric (D_D) to characterize and identify asteroid pairs (Drummond, 1981; Rożek et al., 2011):

$$D_D^2 = \left(\frac{e_B - e_A}{e_B + e_A}\right)^2 + \left(\frac{q_B - q_A}{q_B + q_A}\right)^2 + \left(\frac{I_{BA}}{180^\circ}\right)^2 + \left(\frac{e_B + e_A}{2}\right)\left(\frac{\theta_{BA}}{180^\circ}\right). \qquad (6.1)$$

The term I_{BA} is the angle between the angular momentum vectors ($\boldsymbol{h}$) and θ_{BA} is the angle between the eccentricity vectors ($\boldsymbol{e}$) of the two asteroids (Rożek et al., 2011):

$$\begin{aligned} I_{BA} &= cos^{-1}\left(\frac{\boldsymbol{h_B}\cdot\boldsymbol{h_A}}{h_B h_B}\right) \\ \theta_{BA} &= cos^{-1}\left(\frac{\boldsymbol{e_B}\cdot\boldsymbol{e_A}}{e_B e_B}\right) \end{aligned} \tag{6.2}$$

The Drummond orbital similarity distance which approaches zero as the orbits of two objects become more similar. It is a modified form of the metric created by Southworth and Hawkins (1963), and both metrics were created to compare meteor orbits and determine meteor stream membership. We chose the Drummond orbital similarity distance because Rożek et al. (2011) found it to show the best time stability in the main belt and it is relatively simple to calculate. However, these two metrics and the metrics created by Jopek (1993), Jopek et al. (2008), and Zappala et al. (1990) which was also later modified by Nesvorný and Vokrouhlický (2006) are all statistically equivalent when searching for asteroid pairs (Rożek et al., 2011). In fact, the metric created by Zappala et al. (1990) and modified by Nesvorný and Vokrouhlický (2006) was the one used in Vokrouhlický and Nesvorný (2008) to first identify asteroid pairs.

To build the distribution of D_D which we use as a constraint in our model, we retrieved all the asteroid orbits and absolute magnitudes from the Minor Planet Center (minorplanetcenter.net/iau/MPCORB/MPCORB.DAT) that fall within the inner main belt and have observations at multiple oppositions. We define the inner main belt as $a = [1.7, 2.5]$ AU, $q > 1.7$ AU, and $i < 15°$. We limit our selection to the Inner Main belt because there are a significant number of pairs found there due to the higher degree of observational completeness compared to other regions of the main belt (Vokrouhlický and Nesvorný, 2008). We can also simplify the Yarkovsky forces in our model due to the limited range of semi-major axes and eccentricities.

Rożek et al. (2011) found that when using the mean orbital elements, where the short periodic oscillations are removed, there are a greater number of asteroid pairs that can be picked out of the background population and the asteroid pairs tend to re-

side in more similar orbits. As both of those features essentially create a better signal to noise for the asteroid pairs in the orbital similarity distribution, we exclusively use the mean orbital elements in this study. To calculate the mean orbital elements we use the "prop9" tool in the OrbFit software suite (adams.dm.unipi.it/orbfit), which analytically calculates the mean and proper elements of an asteroid. We use the analytical tool instead of a numerical one due to the much faster execution speed.

We calculate D_D between each asteroid and its nearest neighbor that has a higher absolute magnitude using their mean orbital elements and Eq. (6.1). Finally, we remove all asteroid pairs from the distribution where $\Delta H < 1$ or $\Delta H > 3$, where ΔH is the difference between the magnitude of the secondary and primary asteroid in each pair. For an asteroid pair to be created by YORP, the mass ratio must be $q \lesssim 0.2$ which corresponds to $\Delta H \gtrsim 1$.

Fig. 6.1 shows the resulting D_D distribution of the inner main belt asteroids generated from mean orbital elements and restricted to $1 \leq \Delta H \leq 3$. We also show the D_D distribution generated from a pair-free population. We describe how we calculate this distribution in §6.2.1. As in previous studies, the observed orbital similarity distribution deviates from the pair-free distribution at low values of D_D (Vokrouhlický and Nesvorný, 2008; Rożek et al., 2011). The pair-free distribution shows that only $\approx 1 - 3$ asteroids with a $D_D \leq 10^{-3}$ are generated by random chance, but we find ≈ 55 asteroid pairs with a $D_D \leq 10^{-3}$.

6.2.1 Pair Free Orbital Similarity Distribution

In both Vokrouhlický and Nesvorný (2008) and Rożek et al. (2011), pair-free distributions were created by randomly sampling over the orbital elements of the asteroids in question. Vokrouhlický and Nesvorný (2008) considered the variation in the number density of asteroids to account for large-scale clumping from resonances and large families, and Rożek et al. (2011) randomly selecting each orbital element from the probability distribution of the real sample as if each element was an independent

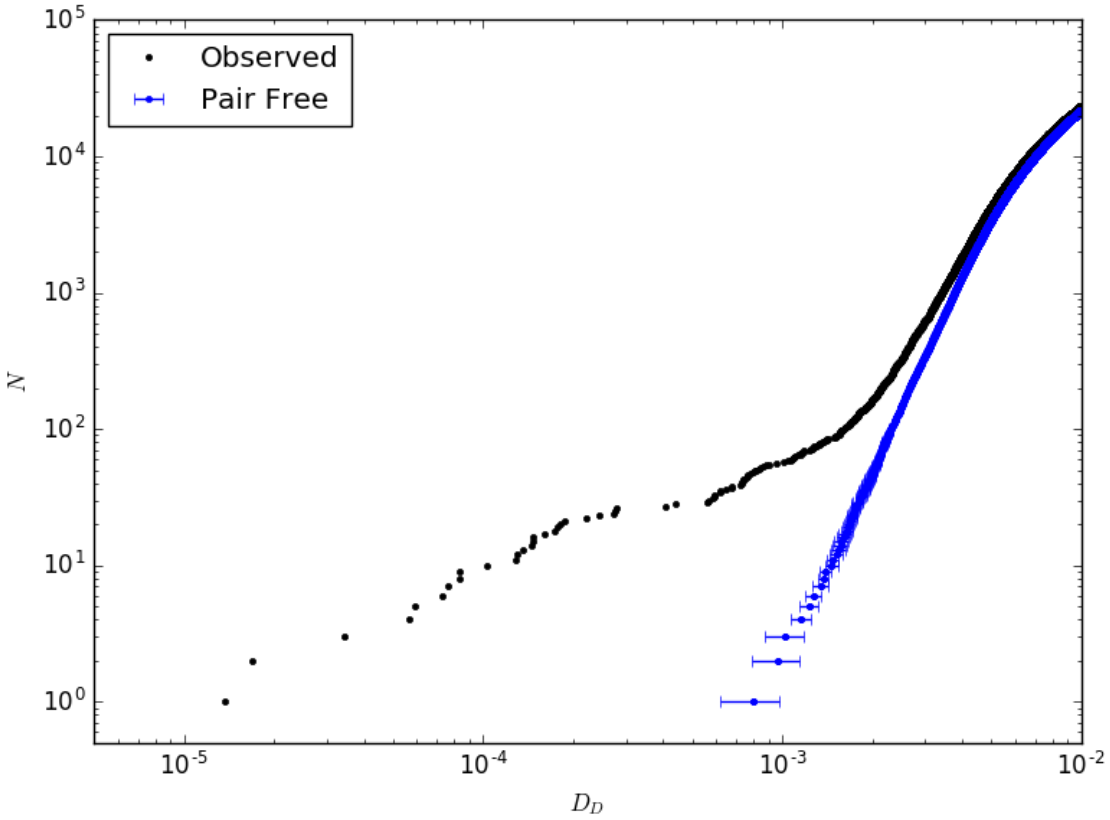

Figure 6.1. The cumulative distribution of the Drummond orbital similarity distance, D_D, between all inner main belt asteroids and their closest neighbor with a larger absolute magnitude. Each distance is calculated using the mean orbital elements of both asteroids, and we restricted the distribution to pairs of asteroids with $1 \leq \Delta H \leq 3$. A pair-free distribution is also shown, which is calculated from fuzzed mean orbital elements of all asteroids (see §6.2.1). The error bars of the pair-free distribution are generated from five instances of generating the fuzzed mean orbital elements.

variable. Both of these methods are useful in the discovery of asteroid pairs, but they do not take into account the clumping of asteroids on a smaller scale, such as less prominent or young asteroid families. By not accounting for small scale clustering, any generated pair-free distributions will continue to deviate from the observed distribution at larger orbital similarity distances. This deviation can be seen in Fig. 1 of Vokrouhlický and Nesvorný (2008) and more clearly in Fig. 1 of Rożek et al. (2011). For this study, we want to isolate the signal of the close orbital similarity distances of asteroid pairs from all other factors to provide the best modeling constraint.

To generate a pair-free distribution, we follow the method described in Section 2.4.1 of Schunová et al. (2012) with a few modifications. We slightly change, or "fuzz," the position of each asteroid in its 5-dimensional orbital element space (a, e, i, Ω, ω). For each asteroid, we find its two closest neighbors with higher magnitudes and calculate their Drummond orbital similarity distance with the current asteroid. Then, we randomly alter the asteroid's orbit such that the Drummond orbital similarity distance between the new orbit and the old is, at most, the average of the distances of its nearest neighbors, which we call $\bar{D}_{fuzz}$. To alter the orbit, we assume that $\bar{D}_{fuzz}$ is formed solely by a change in each orbital element independently. We then calculate the change in each orbital element (Δa, Δe, Δi, $\Delta\Omega$ and $\Delta\omega$) needed to independently generate $\bar{D}_{fuzz}$ by using the appropriate terms in Eq. (6.1). We calculate Δa by:

$$\Delta a = \frac{2aD_{fuzz}}{1 - D_{fuzz}}, \tag{6.3}$$

and can solve for Δe from:

$$D_{fuzz}^2 = \left(\frac{\Delta e}{\Delta e + 2e}\right)^2 + \left(\frac{\Delta e}{\Delta e - 2e + 2}\right)^2. \tag{6.4}$$

For Δi, $\Delta\Omega$, and $\Delta\omega$, we numerically calculate D_D via Eq. (6.1) for two sets of orbital elements that are identical except for the element in question and find the change in that orbital element (e.g., Δa) where $D_D = D_{fuzz}$. For asteroids that do not have a sufficiently close neighbor, the maximum differences $\Delta\Omega = \pm\pi$ or $\Delta\omega = \pm\pi$ may not create a large enough separation to generate $D_D = \bar{D}_{fuzz}$. In those cases we set $\Delta\Omega = \pi$ or $\Delta\omega = \pi$.

Then, we generate a fuzzed orbit (a_f, e_f, i_f, Ω_f, ω_f) where each element (x) is randomly generated within the range $\pm\Delta x$. We continue to randomly generate fuzzed orbits until $D_D \leq \bar{D}_{fuzz}$, where D_D is calculated between the fuzzed orbit and the original orbit. We also check that the asteroid still falls within the bounds of the inner main belt (as defined in previously in this section). We use the average similarity distance between the two closest neighbors, $\bar{D}_{fuzz}$, instead of only the closest neighbor (as in Schunová et al. 2012) because we want to remove any arbitrarily close asteroid pairs from the population. Using only the closest neighbor, the very small D_D of a very close asteroid pair can (and does) remain small. However, by taking the average of ≥ 2 of the asteroid's closest neighbors, a single very close pair does not keep its small D_D. Effectively, this method removes any statistically unusual pair of asteroids but keeps the small scale number density distribution of the population. We also calculated $\bar{D}_{fuzz}$ with the five closest neighbors and found a similar pair-free distribution.

After we generate fuzzed orbits for all asteroids in the inner main belt, we calculate D_D for each asteroid and its closest pair with a larger magnitude, using only the fuzzed orbits. After removing any asteroid that does not fall within $1 \leq \Delta H \leq 3$, we arrive at the distribution shown in Fig. 6.1. The pair-free distribution closely follows a power law with a slope of ≈ 4.7 (similar to Vokrouhlický and Nesvorný 2008), but, it has a smaller deviation from the observed distribution at larger values of D_D compared to both Vokrouhlický and Nesvorný (2008) and Rożek et al. (2011).

6.3 Model Construction

In this section, we build a model pipeline to estimate the distribution of orbital separation distances (D_D) in the inner main belt for a given pair creation rate. The model pipeline is visualized as a flow chart in Fig. (6.2). Each rectangular box describes a main step in the pipeline and the ovals describe assumptions and parameters

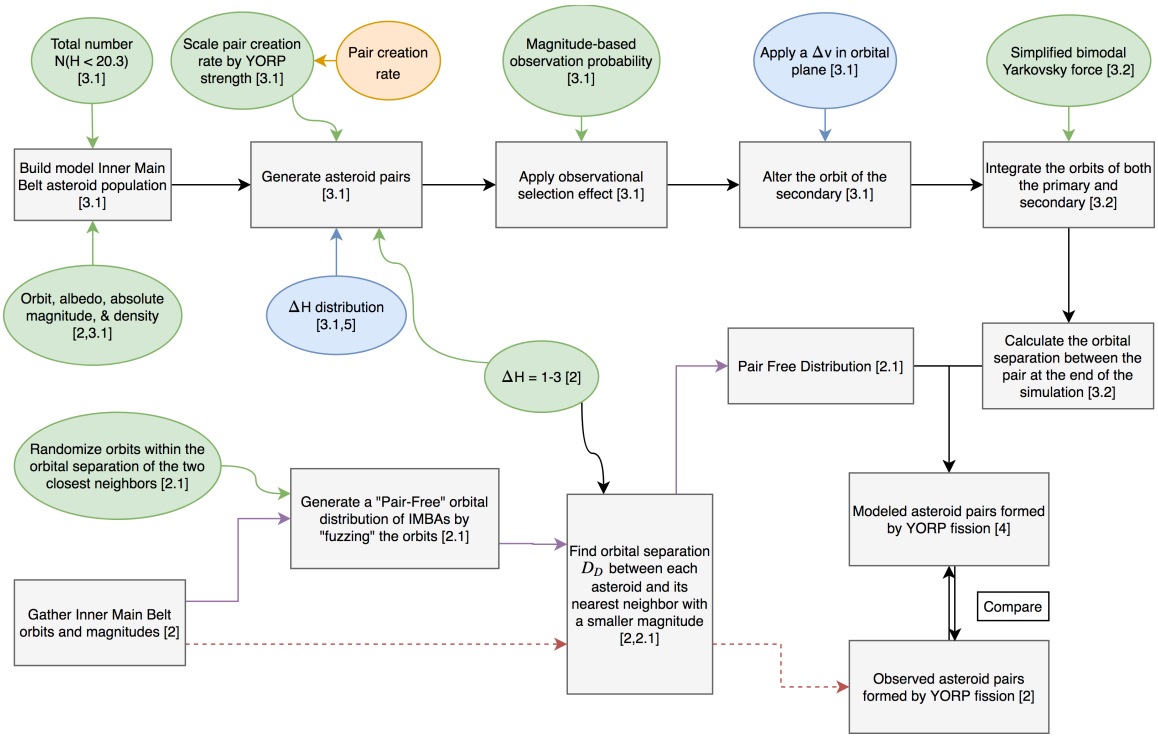

Figure 6.2. A flowchart describing the progression of our model and data analysis. The black rectangles denote the major steps in the pipeline. The green ovals describe the parameters and assumptions made at one particular step. The orange oval is our primary free parameter (the pair creation rate) and the blue ovals are additional parameters that we varied. Each shape also contains section number(s) referring to where we discuss it in the chapter.

that go into each step. We label each box with a section number to denote where we describe the details of each particular step.

6.3.1 Initial Conditions

We initialize each asteroid with an absolute magnitude, orbit, albedo, and density with each variable randomly selected from the appropriate distribution. We generate the absolute magnitude of each asteroid by estimating the size-frequency distribution of the inner main belt asteroids down to the observational limit ($H = 20.3$). We use a combination of the observed inner main belt asteroids retrieved from the Minor Planet Center, and the estimated power law slope, $\alpha = 0.23$, from Gladman et al. (2009) at smaller absolute magnitudes to extrapolate to small sizes. We assume that the Inner Belt is observationally complete up to a magnitude of H = 17.8.

We generated the albedo, p_v, of each asteroid from the bimodal distribution described in Masiero et al. (2011). First, we randomly selected whether the asteroid fell within the high or low albedo population. We applied an equal probability to fall within either population because the population sizes are approximately equal (see Fig. 8 and 10 in Masiero et al. 2011). Albedos for asteroids in the both populations were randomly selected from a Gaussian distribution of $log_{10}(p_v)$, with a mean albedo $\mu = 0.06$ and a standard deviation $\sigma = ^{+0.03}_{-0.02}$ for the low albedo population, and $\mu = 0.28$ and $\sigma = ^{+0.13}_{-0.09}$ for the low albedo population (Masiero et al., 2011). Then, we generate the initial asteroid orbits from a Gaussian multivariate kernel density estimator built from the semi-major axis, eccentricity, and inclination of the inner main belt asteroids retrieved from the Minor Planet Center, and we randomize the orbital angles.

We also choose a pair creation rate, defining the timescale that a particular asteroid will fission and create an asteroid pair. However, not all asteroids will fission into pairs at the same rate. Since YORP is the primary formation mechanism for creating pairs, we can assume that if YORP has a greater effect on an asteroid, then it will

split into a pair more quickly. The change in the spin rate of an asteroid due to the YORP effect is (Scheeres, 2007; Rossi et al., 2009):

$$\dot{\omega} = \frac{3BG_1}{4\pi\rho a^2\sqrt{1-e^2}}\frac{1}{R^2}\mathrm{C_y} \tag{6.5}$$

where B is the Lambertian scattering coefficient, G_1 is the solar radiation constant, ρ is the density of the asteroid, $\mathrm{C_y}$ is a non-dimensional YORP coefficient, R is the volumetric mean radius of the asteroid, and a and e are its semi-major axis and eccentricity. The relative strength of the YORP effect between two asteroids is a function of the density, semi-major axis, eccentricity, radius, and YORP coefficient of each asteroid. However, the YORP coefficient, which contains information about the asteroid's shape and moments of inertia, should not depend on other characteristics of the asteroid. Additionally, it is not necessarily consistent over long periods of time. Thus, we do not consider it when considering relative strength of the YORP effect.

In our model, we calculate the probability of an asteroid splitting into a pair during a timestep, dt, as a function of the relative strength of the YORP effect and a reference pair creation timescale (τ_{pair}):

$$P_{pair} = \frac{dt}{\tau_{\mathrm{pair}}}\left(\frac{\mathrm{km}}{R}\right)^2\left(\frac{2000\,\mathrm{kg/m^3}}{\rho}\right)\left(\frac{2.5\ \mathrm{AU}}{a}\right)^2\frac{1}{\sqrt{1-e^2}}. \tag{6.6}$$

Due to the dependence of Eq. (6.6) on ρ, we also give each model asteroid a density. We assign asteroids from the low albedo population a density of 1000 kg/m^3 and give a density of 2000 kg/m^3 to the asteroids from the high albedo population, corresponding to approximate densities of C and S-type asteroids that have diameters of $\sim 1-5$ km (Carry, 2012).

For each pair, we must determine the size of the primary and secondary members. In our nominal model, we assume that the absolute magnitude difference, ΔH, between the secondary and the primary of each pair follows a distribution with a linearly increasing probability density with increasing ΔH: $f(\Delta H) = 0.5\Delta H - 0.5$, . We also test two other initial distributions: (1) a uniform distribution in ΔH, and (2) a uniform distribution in the mass ratio distribution q. We restrict $1 \leq \Delta H \leq 3$

for all distributions. We use the distribution with a linearly increasing probability density with increasing ΔH as our nominal choice because the best fit results in §6.4 correspond to this distribution. We then determine the magnitude of each asteroid by applying a conservation of mass condition:

$$H_p = H_0 + \frac{5}{3}\log_{10}\left(1 + 10^{-3\Delta H/5}\right) \tag{6.7}$$

$$H_s = H_p + \Delta H, \tag{6.8}$$

where H_0, H_p, H_s are the pre-fissioned, primary, and secondary asteroids' magnitudes.

We generate 517,655 asteroids, which corresponds to the number of predicted asteroids in the inner main belt down to the observational limit of $H < 20.3$. We then choose a pair creation rate, or pair formation timescale τ_{pair}, and randomly generate the asteroid pairs throughout a period of 10 Myr, saving their formation times. Before we begin the time-consuming N-body simulation of each asteroid pair, we apply a simple observational selection effect to test if each pair would be observed. We assume that the relatively constrained region of the inner main belt will remove any strong dependence on orbit and that the fraction of observed to predicted asteroids at a specific absolute magnitude represents the probability of being observed. We then calculate the fraction of observed vs. predicted asteroids by dividing the slope of the observed cumulative size frequency distribution by the slope of the predicted cumulative size frequency distribution. Both the primary and secondary member of each pair must be observed in order to feed them into our N-body simulation.

The last initial condition needed for the N-body simulation is the initial orbital elements of the primary and secondary asteroids. We place both members at the orbit of the pre-fissioned asteroid and then apply a relative velocity kick to the secondary in the orbital plane of the pre-fissioned asteroid. We only apply the kick in the orbital plane because an asteroid that is highly evolved by YORP (i.e. one that has been spun up to fission), will also evolve its orbital pole to 0° or 180° (Čapek and Vokrouhlický, 2004; Vokrouhlický et al., 2015). An asteroid that has fissioned from another one will have a velocity that is primarily in the plane of rotation,

and, therefore, in the plane of the pre-fissioned asteroid's original orbit. From the backwards simulations of Vokrouhlický and Nesvorný (2008) and Pravec et al. (2010), asteroid pairs appear to separate with relative velocities that are less than the escape velocity of the asteroid. We assume that the separation velocity is $\Delta v = \beta v_{esc}$ for all asteroids, where v_{esc} is the escape velocity of the asteroid and β is a free parameter. In the supplementary material of Pravec et al. (2010), they show that many of the well characterized backwards simulations suggest that the relative separation velocities are $\sim 1/10$ of the escape velocity. We test three values: $\beta = 0.05, 0.2,$ and 0.5.

6.3.2 N-body Simulation

After building the initial conditions for all asteroid pairs, we evolve them with the Regularized Mixed Variable Symplectic (RMVS) integrator from the SWIFTER N-body code (Levison and Duncan, 1994). We include seven planets (Venus - Neptune), and run the simulation for 10 Myr with a 15 day timestep. A shorter timestep of 7.5 days does not produce statistically different results. We include a simplified Yarkovsky effect by applying a transverse acceleration to each asteroid, following Vokrouhlický and Nesvorný (2008):

$$a_T = \frac{n^2 a}{2v} \frac{da}{dt} \tag{6.9}$$

where n and v are the mean motion and current velocity of the asteroid, and da/dt is the average change in the semi-major axis of the asteroid from the Yarkovsky force. The value of da/dt has been estimated from previous studies (e.g., Bottke et al. 2006; Granvik et al. 2016), for asteroids at a given size and orbit. Here, we calculate da/dt as a function of the asteroid's density and diameter following Granvik et al. (2016):

$$\frac{da}{dt} = \pm \left(\frac{da}{dt}\right)_0 \left(\frac{1\,\mathrm{km}}{D}\right) \left(\frac{2000\,\mathrm{kg/m^3}}{\rho}\right) \tag{6.10}$$

where $(da/dt)_0 = 2 \times 10^{-4}$ AU/Myr. As in Granvik et al. (2016), we including only a maximum and minimum da/dt, because most small asteroids have obliquities near 0 or 180° (Hanuš et al., 2011), which is especially true for asteroids highly evolved by YORP. Because the diurnal component of the Yarkovsky effect usually dominates,

the bimodality of the asteroids' obliquities will create a bimodality in the resulting Yarkovsky force (Bottke et al., 2006). Additionally, since both members of each pair have the same rotational direction, they will evolve in the same direction, and have the same sign in Eq. (6.10).

At the end of the N-body simulations, we sample the orbital elements of each asteroid pair at the end of the 10 Myr period over which the asteroid pairs were generated. For example, if an asteroid pair was generated at 2 Myr, we extract the orbital elements after 8 Myr have passed in the N-body simulation. We also extract the orbital elements of the planets at the same times to calculate the mean orbital elements of each asteroid. From the mean orbital elements, we then calculate D_D between each asteroid and its pair.

Finally, we combine the D_D of all simulated asteroid pairs with the pair-free distribution generated in §6.2.1 to generate a model D_D distribution for the entire inner main belt, and compare it with the observed D_D distribution shown in Fig. (6.1). The primary free parameter for our model is the rate of pair creation, $1/\tau_{\rm pair}$, but we also vary β, the coefficient that describes the initial separation velocity of each asteroid pair as a function of the primary's escape velocity, and the initial distribution of the size difference between the secondary and primary asteroids. We also repeat the entire simulation including the creation of the asteroids in the inner main belt, forming the asteroid pairs, and integrating their orbits five times and use the average D_D distribution to compare with observations.

6.4 Results

Fig. (6.3) shows the observational D_D distribution from the inner main belt as well as distributions for three pair creation rates from our nominal model, with pair creation rates of 0.005, 0.011, and 0.022 $\rm Myr^{-1}$ for an asteroid with $D = 1$ km, $a = 2.5$ AU, $e = 0$, and $\rho = 2000$ $\rm kg/m^3$. We show a distribution created with a pair creation rate of 0.011 $\rm Myr^{-1}$ that matches the observed distribution extremely well, as

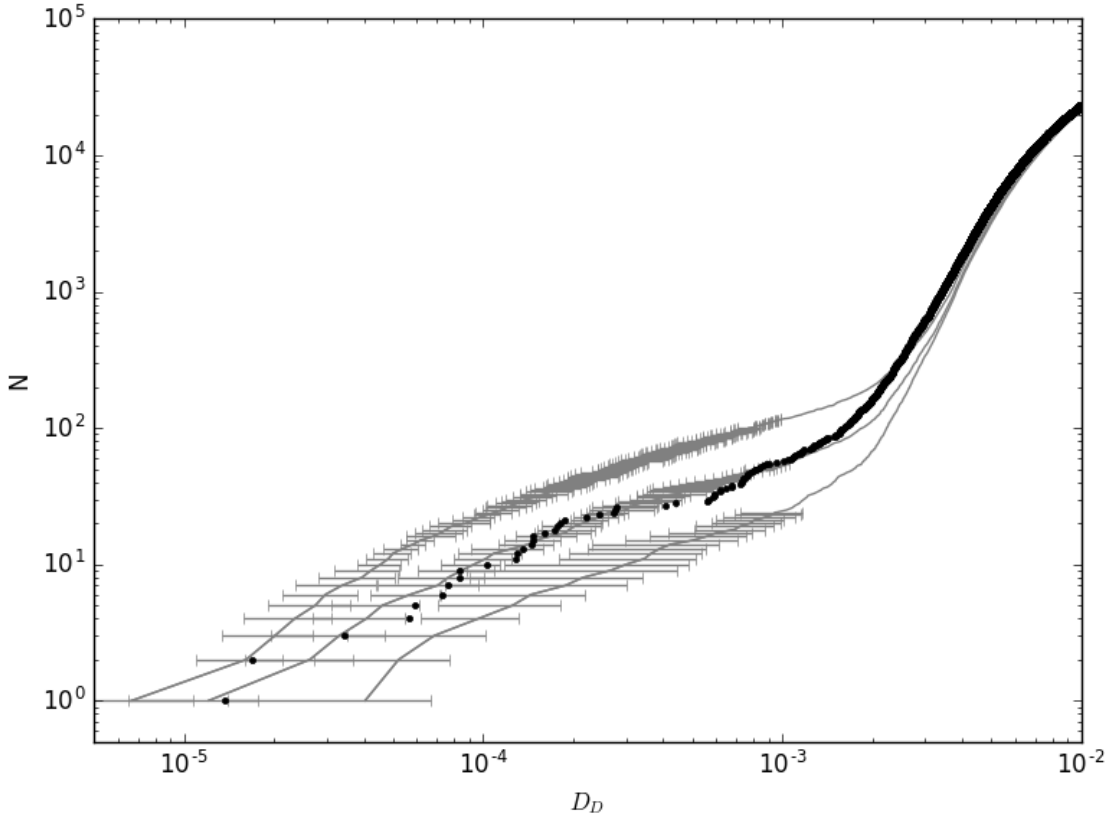

Figure 6.3. The cumulative distribution of the Drummond orbital similarity distance, D_D, between all observed inner main belt asteroids (black) and three different nominal model runs (gray) with varying pair creation rates. The observed D_D distribution is identical to that in Fig. 6.1. All model runs are generated using N-body simulations with an initial separation velocity of $\Delta v = 0.2 v_{esc}$, and the differential magnitude between the members of each pair are selected from linearly increasing probability density with increasing ΔH (see §6.3.1). The three model runs have pair creation rates of 0.005 Myr^{-1} (bottom), 0.011 Myr^{-1} (middle), and 0.022 Myr^{-1} (top). The middle model run generates a the best fit to observations of all tested parameters, while the other runs under- and over-predict the number of asteroid pairs.

well as two distributions created from pair creation rates 0.005, and 0.022 Myr^{-1} that under-estimate and over-estimate the number of asteroid pairs. Using a two-sample Kolmogorov-Smirnov test on the observed and modeled pairs with $D_D \leq 10^{-3}$, we find that for distributions generated with a pair creation rate of $0.008 - 0.013$ Myr^{-1}, the null hypothesis that the samples are drawn from the same distribution cannot be rejected at a 95 % confidence level. We choose $D_D \leq 10^{-3}$ as a reference point for determining asteroid pairs that are most likely not generated by random chance. Similar cutoffs do not generated different results.

We can also represent our results as a the number of YORP cycles needed to create an asteroid pair. We assume that a YORP cycle is twice the amount of time needed to change an asteroid's spin rate from zero to a fissioning spin rate, assuming a constant YORP acceleration. Assuming asteroids fission at a spin period of ≈ 2.5 hours, we can use Eq. (6.5) to estimate the average timescale of a YORP cycle, $\bar{\tau}_{\mathrm{YORP}}$, for an asteroid with $a = 2.5$ AU, $e = 0$, and $\rho = 2000$ $\mathrm{kg/m}^3$. We also assume an average value for $C_y = 0.01$ (e.g., (Jacobson and Morbidelli, 2014)), and we find $\bar{\tau}_{\mathrm{YORP}} = 9.7$ Myr. Thus, we predict that asteroids fission and create an asteroid pair every 8-13 YORP cycles.

An important result from the backwards simulations of asteroid pairs is that most pairs have ages less than 1 Myr (Pravec et al., 2010). In Fig. (6.4), we show the distribution of the ages of all asteroid pairs with $D_D \leq 10^{-3}$. The majority of pairs are very young, with $\approx 85\%$ of all pairs generated in the last 1 Myr, consistent with Pravec et al. (2010).

We show the three initial distributions of the size difference between the primary and secondary members of each pair in the upper plot of Fig. (6.5). In the lower plot, we show the final differential magnitude distribution resulting from the three different initial distributions. We only consider the pairs with $D_D \leq 10^{-3}$. We also show the differential magnitude distribution of observed asteroid pairs. Our nominal model with a linearly increasing probability density with increasing ΔH, matches

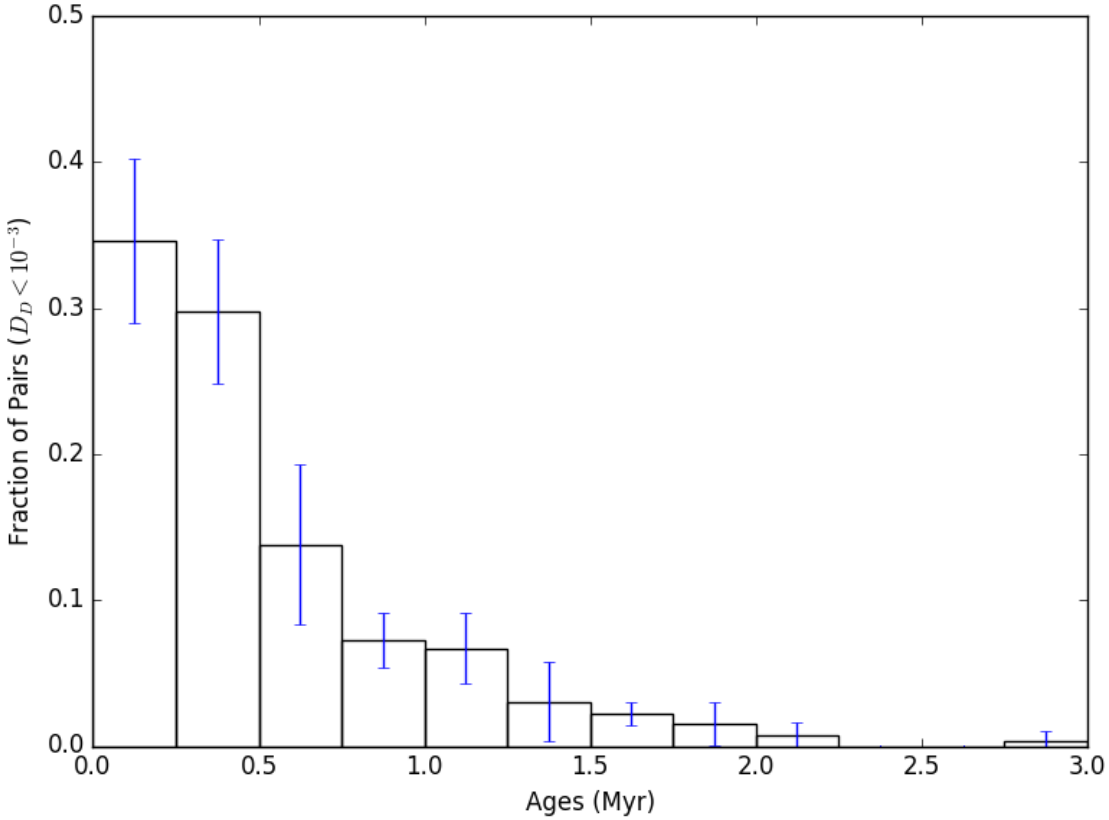

Figure 6.4. The age distribution of all asteroid pairs with $D_D \leq 10^{-3}$ at the end of our simulations. This distribution is generated from the best fit simulation parameters (see §6.4), and the error bars are the standard deviations from the five separate simulations. The ages of most pairs are very young with $\approx$ 85% having separated less than 1 Myr ago, qualitatively consistent with Pravec et al. (2010).

the observations well, but the other two initial initial distributions over-predict the number of higher mass ratio pairs.

We also varied the initial separation velocities between the secondary and primary of each asteroid pair. For $\beta = 0.05$ and $\beta = 0.05$, we find very similar best fit ranges for pair creation rates of $0.008 - 0.012$ Myr^{-1} and $0.009 - 0.012$ Myr^{-1}, respectively. However, the model with $\beta = 0.2$ best matches the power law slope at $D_D \lesssim 10^{-3}$, while a higher value of β steepens the slope and lower value of β shallows it.

6.5 Discussion

Our estimation that an asteroid creates an asteroid pair every 8-13 YORP cycles can provide important insight into the process of YORP-induced evolution and rotational fission. Previous models (Marzari et al., 2011; Jacobson and Scheeres, 2011; Jacobson and Morbidelli, 2014; Bottke et al., 2015; Jacobson et al., 2016; Graves et al., 2018) have calculated the rate of fission from YORP-induced spin-up by using theoretical calculations (e.g., using Eq. 6.5), and making a few critical assumptions. In particular, these models must decide how asteroids evolve at very low and very high spin rates. At very low spin rates, the process of YORP evolution can potentially become stagnant, and other processes such as impacts may play an important role in their evolution (Marzari et al., 2011). At very high spin rates, many of the models listed above assume that the asteroid will fission and then settle into a shape that allows the YORP effect to decrease its spin rate. However, the dynamics at high spin rates are poorly understood. It is unclear if asteroids will always fission when they reach very high spin rates, or if it is common for surface or internal failure to cause a significant change in the shape of the asteroid and change the direction of the YORP acceleration before fission occurs.

Another important assumption that previous YORP-evolution models had to make was the presence, or lack thereof, of Stochastic YORP. Stochastic YORP is the idea that an the YORP effect is highly dependent on the exact shape and iner-

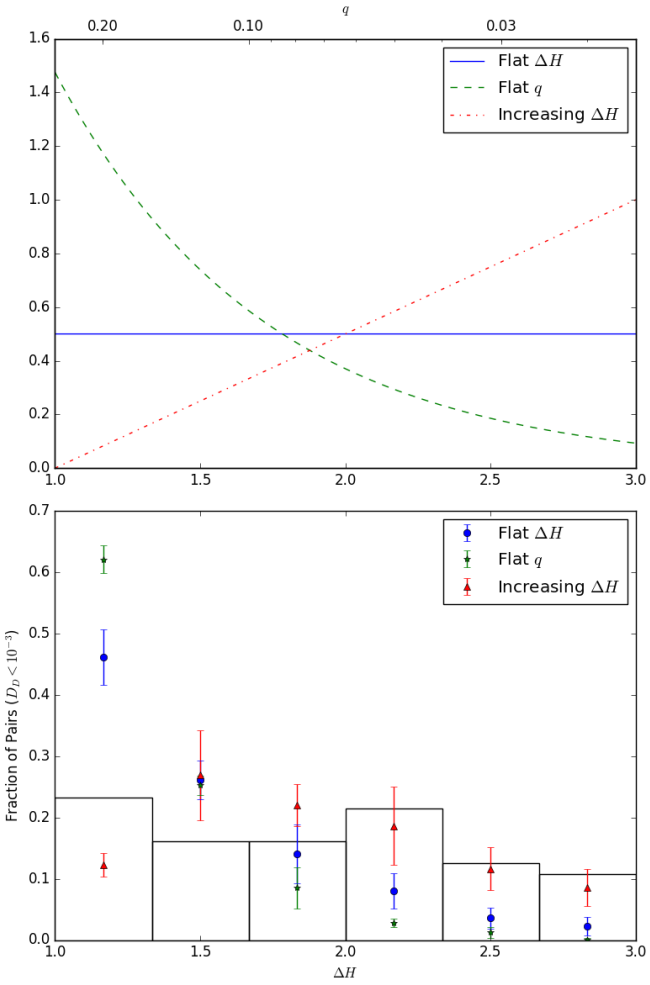

Figure 6.5. The three tested initial differential magnitude distributions and their resulting effect on the differential magnitude distribution of modeled asteroid pairs. In the top plot, we show the probability density functions of each initial differential magnitude distribution that we tested. In the bottom plot, we show the fraction of pairs in each differential magnitude bin for the three initial distributions. Only the initial distribution generated from a linearly increasing probability density with increasing ΔH generates a differential magnitude distribution of asteroid pairs that resembles observations. The initial distributions generated from a flat distribution in ΔH or q both over-predict the fraction of low differential magnitudes ($\Delta H \sim 1$) and under-predict the fraction of high differential magnitudes ($\Delta H \sim 2 - 3$).

tial distribution of the asteroid, and that by altering the shape of an asteroid from collisions, surface mass movement, or internal deformation can drastically change the strength - and possibly direction - of the YORP effect (Statler, 2009; Bottke et al., 2015; Cotto-Figueroa et al., 2015). Some models have accounted for Stochastic YORP through estimating the effects of collisions on each asteroid (e.g., Marzari et al. 2011; Jacobson and Morbidelli 2014; Bottke et al. 2015; Jacobson et al. 2016) and others have not considered any Stochastic YORP, allowing asteroids to steadily evolve from low to high spin rates, and vice versa (Rossi et al., 2009; Graves et al., 2018). Additionally, Cotto-Figueroa et al. (2015) accounted for Stochastic YORP by considering the change in the shape of asteroids as their potentials change due to YORP-induced evolution of their spin rates. Cotto-Figueroa et al. (2015) argued that Stochastic YORP could drastically decrease the rate of YORP-induced rotational fission by trapping asteroids in self-limiting cycles.

Our study does not rely on a YORP evolution model, and thus, we do not need to make any of the assumptions discussed above. However, by comparing our modeled pair creation rate with the pair creation rate determined from a theory-driven YORP evolution model, we can put constraints on the the efficiency of YORP at fissioning asteroids. The pair creation rate is effectively measuring three entangled components: (1) the rate an asteroid evolves to a high spin rate via YORP and subsequently fissions, (2) the probability that the fissioned asteroid produces a low mass ratio binary (with the mass ratio $q \lesssim 0.2$), and (3) the probability that a low mass ratio binary will quickly become gravitationally unbound. There is also a possibility that asteroid pairs are formed from a radiation effect acting on a tidally locked binary asteroid (known as the binary YORP effect; Ćuk and Burns 2005). The binary YORP effect can cause the expansion of a binary asteroid, eventually leading to the separation of the two bodies. However, this process should only play a minor role in creating asteroid pairs. The relationship between the spin rate of the primary and the mass ratio of most asteroid pairs from Pravec et al. (2010) means that most asteroid pairs were formed from an asteroid that was very near the critical spin rate. Binary asteroids

that evolve via the binary YORP effect require that the bodies are tidally locked (Ćuk and Burns, 2005). Thus, as they expand, the spin rate of the primary slows down and would not correspond to the relationship found in Pravec et al. (2010).

Using the results from Jacobson and Scheeres (2011) and Jacobson et al. (2016), we can estimate the pair creation rates from their theory-driven YORP evolution models. Jacobson and Scheeres (2011) found the probability that a low mass ratio binary will quickly become gravitationally unbound to be approximately 70%. Jacobson et al. (2016) used a YORP evolution model paired with a binary evolution model to estimate the ratio of high mass to low mass ratio binaries. Since they used a YORP evolution model, they needed to make many of the assumptions discussed above. They assumed that there is no YORP stagnation at low spin rates, that an asteroid will fission every time it reaches a very high spin rate, and that the only source of Stochastic YORP is due to collisions. Using those assumptions, they found that high mass ratio binaries form 4-8 times more often as low mass ratio binaries. Finally, we can roughly assume that the effect of impact-induced Stochastic YORP will not significantly alter the timescale to fission, since a collision will approximately have the same chance of increasing or decreasing the spin rate of the asteroid. Thus, we assume that the YORP cycle that we defined in §6.4 is equal to the timescale to fission from Jacobson et al. (2016). Putting these three components together, we find that the models of Jacobson and Scheeres (2011) and Jacobson et al. (2016) predict a pair creation timescale of $\sim 6 - 11$ YORP cycles.

The similarity between the estimated pair creation timescales between this study and those of Jacobson and Scheeres (2011) and Jacobson et al. (2016) supports many of the assumptions made in Jacobson et al. (2016). Most importantly, the average rate of YORP-induced fission must be very similar to that used in Jacobson et al. (2016). Specifically, there cannot be a significant amount of YORP stagnation at low spin rates and most asteroids must fission when they reach very high spin rates. Additionally, the effect of Stochastic YORP on the rate of YORP-induced rotational fission appears to be minor. The trapping of asteroids in self-limiting YORP cycles,

as suggested in Cotto-Figueroa et al. (2015), cannot occur for a significant number of asteroids or for large periods of time. If any of these assumptions were not true, then the pair creation rate would be lower than what we found in this study.

Another important result is that the distribution of asteroids which fission into low mass ratio ($q \lesssim 0.2$) binaries/pairs appears to skew towards lower mass ratios. Fig. (6.5) showed that a distribution with a linear increase in the probability density function from 0 at $\Delta H = 1$ to 1 at $\Delta H = 3$ creates much better observed differential magnitude (or mass ratio) distribution compared to initial distributions with more pairs formed at lower values of ΔH. The distributions that are uniform ΔH or q create more pairs with lower ΔH, due to a much larger population of pairs at smaller sizes. Smaller asteroid pairs, where the primary is closer to the observational limit, will most likely only be observed if ΔH is small. We also compared the sizes of the primary asteroids, and found that the nominal distribution of ΔH is a much better fit. The other two distributions over estimate the number of asteroid pairs at $H \gtrsim 17$. Our best fit initial ΔH distribution suggests a strong bimodality in the mass ratios of asteroids fissioned by YORP spin-up, where both high mass and low mass ratio fissioning can occur but we should find fewer asteroid pairs/binaries with $q \approx 0.1-0.2$.

If we use the pair creation rate, paired with the mass loss per fission and pair creation, we can also estimate the rotational disruption rate due to YORP spin-up and fission. By using our initial distribution of ΔH, we find the average mass ratio is $\bar{q} \approx 0.05$. In estimates of collisional disruption rates of asteroids, a common metric is the timescale to break apart an asteroid such that at most half of its original mass is in the largest fragment (e.g., Bottke et al. 2005). From our best estimate of the pair creation rate, 0.008-0.013 Myr^{-1}, we can roughly estimate the average timescale for an asteroid to lose half of its mass from rotational fission: 0.75–1.25 $\left(1\mathrm{km}^2/D^2\right)(1\mathrm{AU}/a^2)$ Gyr. For this quick estimate, we ignored the effect of the decrease in diameter of the primary after each fission. Regardless, this estimate suggests that rotational fission plays a less significant role than collisional disruption ($t_{\mathrm{coll}} \sim 100$ Myr; Bottke et al. 2005) on the size-frequency distribution of the main belt.

Finally, a measure of the pair creation rate can be used to make an estimate if, and at what sizes, we may observe asteroid pairs in the Near-Earth Asteroid (NEA) population. We have not yet observed any NEA pairs (Schunová et al., 2012). The chaotic nature of NEA orbits suggests that the detectability lifetimes of asteroid pairs would drastically reduced, but their small sizes and orbits that take them closer to the Sun should increase their rate of rotational fission from the YORP effect. A similar model as the one used in this study could make this estimate, but it is left for future work.

6.6 Conclusion

Most asteroid pairs are formed from YORP-induced rotational fission followed by a rapid escape of the secondary. By tracking the evolution of simulated asteroid pairs and comparing their distribution to the observed distribution, we can estimate the rate of pair creation, and gain insight into the process of YORP evolution and fission. In this study, we restricted our analysis to the inner main belt, and calculated the distribution of the Drummond orbital similarity distance, D_D between each asteroid and its nearest neighbor with a larger absolute magnitude. We only considered pairs where the differential magnitude between the secondary and the primary is $1 \leq \Delta H \leq 3$, to limit our population to the pairs that could only be formed by YORP fission, We calculated the values of D_D from the mean orbital elements due to their effectiveness at identifying asteroid pairs (Rożek et al., 2011). We also generated a pair-free distribution in the inner main belt by taking each asteroid and "fuzzing" its orbit to remove any pairs of asteroids with an anomalously low D_D.

We then built a model to simulate the creation and disassociation of asteroid pairs in the inner main belt. We estimated the population of asteroids in the inner main belt and simulated the creation of asteroid pairs over 10 Myr with a set pair creation rate. We also scaled the relative creation rate by the rate at which the YORP effect changes the spin rate of an asteroid. Each asteroid pair was given a differential magnitude,

ΔH, or mass ratio, q. We tested three different differential magnitude distributions in our model: (1) a linearly increasing probability density with increasing ΔH, (2) a uniform distribution in ΔH, and (3) a uniform distribution in q. The secondaries of each pair were also given a relative velocity kick in a random direction within their orbital plane. The size of the kick was set to a fraction of the escape velocity, and we tried three different values $\beta = 0.05, 0.2, \text{and } 0.5$, where $\Delta v = \beta v_{esc}$.

We applied an absolute magnitude-dependent observational selection to the model population and tracked the orbits of all generated asteroids for 10 Myr in an N-body simulation, which included a simplified Yarkovsky force. Then, we extracted the orbits of all asteroid pairs at the end of the 10 Myr model time, and generated their mean orbital elements. We calculated D_D of all of the asteroid pairs and combined them with the pair-free D_D distribution. By comparing the observed and modeled D_D distributions we found the best-fit pair creation rate to be $0.008 - 0.013$ Myr^{-1}. We also found that the initial differential magnitude distribution between the members of each pair with a linearly increasing probability density with increasing ΔH to best fit the differential magnitude distribution of the observed pairs. The other initial differential magnitude distributions over-predicted the number of higher mass ratio pairs. We also found that the choice of β did not greatly affect the best-fit pair creation rate. However, the solution with $\beta = 0.2$ best fit the observed power law slope at $D_D \leq 10^{-3}$, while $\beta = 0.05\text{and } 0.5$ under-predicted and over-predicted the observed slope, respectively.

The best fit pair creation rate corresponds to an asteroid pair forming every 8-13 YORP cycles. This pair creation rate is consistent with results from Jacobson and Scheeres (2011) and Jacobson et al. (2016), suggesting that our results support many of the assumptions in their models. Specifically, our results argue for a lack of any significant self-limitation or stagnation of YORP evolution. Finally, our results suggest a lack of importance of YORP-induced rotational disruption on the size frequency distribution of the main belt. Due to the steep skew towards asteroid pairs being formed with a larger ΔH (or a smaller mass ratio), the timescale for an aster-

oid to lose a significant fraction of its mass is much smaller than the timescale from catastrophic collisions.

7 CONCLUSION

Chapters 4, 5, and 6 all have their own conclusions that are contained within the context of each individual study. However, it is also important to consider the combined conclusions from all three. In particular, Chapters 2-5 are all focused on determining the major resurfacing mechanisms that are present on S and Q-type asteroids. Another important connection is between Chapters 4 and 6, since Chapter 6 directly addresses many of the assumptions used in the YORP-induced evolution model developed in Chapter 4, §4.1. I discuss those combined conclusions here, and leave with ideas for future work.

In Chapter 2, §2.2, I discuss six mechanisms that are expected to resurface asteroids:

1. Catastrophic collisions,
2. Impact gardening,
3. Non-catastrophic collisions followed by seismic shaking,
4. Tidal effects from close encounters with the terrestrial planets,
5. YORP-induced spin-up and failure or fission, and
6. Thermally-induced surface degradation.

All of these mechanisms can certainly resurface some asteroids, but it can be difficult to determine the relative effectiveness of each mechanism. As discussed in Chapter 2, §2.2, quick calculations and previous studies have suggested that all of these mechanisms could play a dominant role in the creation of less weathered asteroids, except for catastrophic collisions. Thus, a constraint is needed to quantitatively test the effectiveness of each mechanism.

In Chapter 3, I showed that the distribution of spectral slopes provided a powerful constraint to determine the most dominant resurfacing mechanisms. I showed that the distribution of spectral slopes has two primary trends, which can reasonably explain the presence of all Q and S-type asteroids with low spectral slopes. I show that the average spectral slope decreases with decreasing size for asteroids with $D \lesssim 5$ km and that the average spectral slope decreases with decreasing perihelion for $q \lesssim 0.9$ AU. From the simulations in Chapters 4 and 5, I found three primary results: (1) YORP-induced spin-up and failure or fission can explain the spectral slope vs. size trend, (2) tidal effects from close encounters with the terrestrial planets cannot explain the spectral slope vs. perihelion trend, and (3) thermally-induced surface degradation can explain the spectral slope vs. perihelion trend.

These results taken in this simplified form suggest the following interpretation: YORP-induced spin-up and failure and thermally-induced surface degradation are the dominant resurfacing mechanisms for S and Q-type asteroids. However, there are a few inconsistencies and caveats. First, in all of the resurfacing models in Chapters 4 and 5, I left the space weathering timescale as a free parameter. The YORP-induced spin-up and failure model required a space weathering parameter of $\tau_{SW} \gtrsim 4$ Myr, and the thermally-induced surface degradation model required a space weathering parameter of $\tau_{SW} \lesssim 5$ Myr (both timescales are for asteroids with $a = 1$ AU). While these timescales do overlap slightly, the thermally-induced degradation model had better solutions with a shorter timescale, and many laboratory experiments, and the solar flare particle tracks on asteroid (25143) Itokawa, also argue for a space weathering timescale of $\tau_{SW} \lesssim 1$ Myr (potentially significantly less). See Chapter 2, §2.2, for a discussion of these timescales.

To further illustrate the timescales of these resurfacing and space weathering processes, I compare the resurfacing processes of YORP-induced spin-up and failure and thermally induced surface degradation with space weathering due to the solar wind as a function of solar distance in Fig. 7.1. I show the relative timescales of all processes, and how they scale with solar distance for a 1 km asteroid with zero eccentricity.

The two space weathering functions have timescales of 10 kyr and 100 kyr at 1 AU. YORP-induced spin-up and failure has a timescale of 1 Myr at 1 AU, approximating a fast YORP resurfacing solution from the model in Chapter 4. Thermally induced surface degradation has a timescale of 150 kyr at 1 AU and $k = 8$, to show the best fit solution from the model in Chapter 5.

Due to solar irradiation controlling the scaling of the timescales of both space weathering and YORP, the difference between those timescales remains constant. As the resurfacing timescale due to YORP is always larger than the space weathering timescale, YORP can only slightly lower the average spectral slope of all 1 km asteroids (as seen in e.g., Fig. 3.1). However, a very short space weathering timescale may create too large of a difference, and YORP (as it is modeled in Chapter 4) cannot significantly alter the average spectral slope of 1 km asteroids. Thermally induced surface degradation scales much more strongly with solar distance and can have shorter timescales than space weathering for small solar distances, while becoming very slow at high solar distances. Fig. 7.1 qualitatively shows the two regimes of resurfacing mechanisms: (1) $q \gtrsim 1.3$, where YORP-induced surface degradation is the primary resurfacing mechanism, and (2) $q \lesssim 1$ AU where thermally induced surface degradation dominates the resurfacing of asteroids. Both mechanisms can potentially work in the other regime but are much less effective.

Due to the multiple arguments for a fast space weathering timescale ($\tau_{SW} \lesssim$ 1 Myr), it appears that the required space weathering timescale of $\tau_{SW} \gtrsim 4$ Myr for my YORP-induced spin-up and failure model is difficult to support. A possible solution is that the relatively unexplored mechanisms of impact gardening or non-catastrophic collisions followed by seismic shaking could be a more efficient resurfacing mechanism than YORP-induced spin-up and failure or fission. However, explaining the spectral slope vs. size trend that appears to be present in both the main belt, where collisions are likely, and the NEA region, where collisions may be less frequent, could be very difficult. A full analysis of the viability of a impact-induced resurfacing mechanism is a complex topic that I leave for a future study.

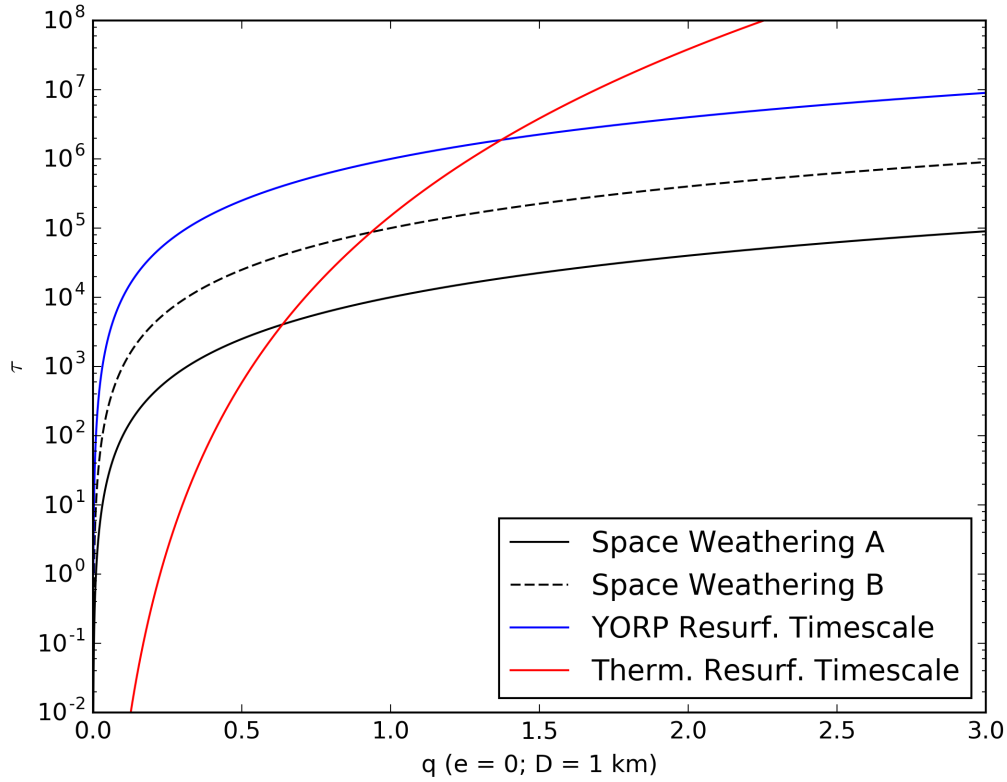

Figure 7.1. The relative timescales of resurfacing processing and space weathering due to the solar wind as a function of perihelia for a 1 km asteroid in a circular orbit. The two space weathering functions have timescales of 10 kyr (A) and 100 kyr (B) at 1 AU, and the resurfacing processes have timescales at 1 AU of 4 Myr for YORP-induced spin-up and failure and 150 kyr for thermally induced surface degradation. The thermally induced surface degradation function also uses $k = 8$ to control how the timescale scales with perihelion (or solar distance).

Another solution to shorten the timescale of resurfacing from YORP-induced spin-up and failure is that downslope motion and overturn may be occurring on the surfaces of asteroids as their spin rates are changed by the YORP effect. As the spin rate of an asteroid is changed from zero to a fissioning spin rate (or vice versa), the local slopes on the surface will drastically change. Most asteroids do not sustain these high local slopes, as Richardson et al. (2018) showed that $\approx 70\%$ of all asteroids exist in a region of "maximum surface stability," where the topographic variation the local slopes are very low. Thus, over the course of a YORP cycle, an asteroid's surface must fail, deform, and expose unweathered material multiple times. This more continuous and rapid resurfacing process should also require a faster space weathering timescale to match the observed spectral slope vs. perihelion trend. Additionally, the modeled spectral slopes of asteroids under the effect of space weathering and YORP spin-up and fission become bimodal at small sizes (Fig. 4.1), which is not seen in the observations (Fig. 3.2). A more continuous resurfacing process would also eliminate the bimodality of the spectral slopes.

Finally, the results of the pair creation rate in Chapter 6 directly support many of the assumptions in the YORP-evolution model in Chapter 4. Since the pair creation rate that is necessary to match the population of asteroid pairs is remarkably consistent with the calculated pair creation rate from the results of the YORP-evolution model of Jacobson et al. (2016), the assumption that the YORP effect consistently changes the spin rate of asteroids over time without any substantial self-limitation or stagnation must be valid. Any appreciable self-limitation or stagnation of the YORP evolution of small asteroids would also increase the time it takes for those asteroids to spin-up to a point of fission or failure. It would also increase the time needed to change the local slopes on the surface of an asteroid. Both of these effects would decrease the rate of resurfacing from a YORP-induced process, and argue for a different resurfacing process to explain the spectral slope vs. size trend. The lack of self-limitation or stagnation of the YORP effect supports it as a potentially rapid size-based resurfacing process.

7.1 Looking to the Future

As I worked on my third project on the asteroid pair creation rate, I finally felt like I had come into my own as a scientist. I now have plenty of new ideas for future projects and have continuously thought about different ways to model asteroids. However, after I finish my dissertation (and publish Chapters 5 and 6), I will be leaving the field. I am excited for the new direction my life is taking, but I wanted to use this section to build a wish list of questions that I hope will be answered. I also hope that some of the work here will help others in future studies to answer these questions.

The primary question that I hope to be answered is, what are the primary resurfacing mechanisms for S and Q-type asteroids? I believe I have helped to answer this question, but there is still work to be done. While it is certainly possible (and I would even go so far to say probable) that the primary resurfacing mechanisms are (1) YORP-induced spin up and failure created Q-type asteroids at small sizes, and (2) thermally induced degradation creating Q-types at low perihelia, it is far from a conclusive explanation. In particular, the very short space weathering timescales inferred from the solar flare particle tracks on asteroid (25143) Itokawa (1–10 kyr; Keller and Berger 2014) place a very tight constraint on resurfacing mechanisms. Any studies that address whether the YORP effect could resurface asteroids more rapidly than in Chapter 4 would be very interesting. Also, resurfacing from small impacts creating gardening or seismic effects would also need to be studied in detail to assess their viability of resurfacing small asteroids. As these processes can be very difficult to model, it may be worthwhile to investigate the differences in impact rates across the inner solar system (e.g. NEAs vs. main belt) and see if they have any effects on the weathering states of small asteroids.

Another question I hope to have answered is, how and when do the surfaces of OC-like asteroids breakdown due to thermal effects? I addressed this in Chapter 5, §5.5.3, but I will mention it again here for completeness. I believe there is a great

opportunity for laboratory testing of the thermal degradation timescale as a function of induced thermal stress. These results could help address the wide range of acceptable parameters used in Chapter 5. Most importantly, they could help constrain the observable space weathering timescale on the surface of S and Q-type asteroids, further allowing us to determine the most dominate resurfacing mechanisms.

Finally, I hope that the pair creation rate, calculated in Chapter 6, can be applied as a constraint in future work. As mentioned in Chapter 6, §6.5, the pair creation rate could be used to predict the number and size of asteroid pairs in the NEA region. Additionally, a full investigation of the rate of rotational disruption may be more useful than the order of magnitude arguments made in Chapter 6, §6.5. Also, I did not consider any asteroid pairs that were formed from high mass ratio binaries. While these asteroid pairs are only a small portion of the entire population, their larger mass ratios could have an important contribution to the rate of rotational disruption.

I have very much enjoyed my time studying, analyzing, and modeling asteroids these last few years. I know that many of the skills that I have learned here will serve me well in my future, and I plan to keep an eye on new and exciting studies and missions. To the asteroid and the entire planetary science communities, keep doing great work!

Bibliography

Auger, A.-T., Groussin, O., Jorda, L., El-Maarry, M. R., Bouley, S., Séjourné, A., Gaskell, R., Capanna, C., Davidsson, B., Marchi, S., Höfner, S., Lamy, P. L., Sierks, H., Barbieri, C., Rodrigo, R., Koschny, D., Rickman, H., Keller, H. U., Agarwal, J., A'Hearn, M. F., Barucci, M. A., Bertaux, J.-L., Bertini, I., Cremonese, G., Da Deppo, V., Debei, S., De Cecco, M., Fornasier, S., Fulle, M., Gutiérrez, P. J., Güttler, C., Hviid, S., Ip, W.-H., Knollenberg, J., Kramm, J.-R., Kührt, E., Küppers, M., Lara, L. M., Lazzarin, M., Lopez Moreno, J. J., Marzari, F., Massironi, M., Michalik, H., Naletto, G., Oklay, N., Pommerol, A., Sabau, L., Thomas, N., Tubiana, C., Vincent, J.-B., and Wenzel, K.-P. (2018). Meter-scale thermal contraction crack polygons on the nucleus of comet 67P/Churyumov-Gerasimenko. *Icarus*, 301:173–188.

Bell, J. F., Davis, D. R., Hartmann, W. K., and Gaffey, M. J. (1989). Asteroids - The big picture. *Asteroids II*, pages 921–945.

Bendjoya, P. and Zappalà, V. (2002). Asteroid family identification. *Asteroids III*, pages 613–618.

Binzel, R. P., Morbidelli, A., Merouane, S., DeMeo, F. E., Birlan, M., Vernazza, P., Thomas, C. A., Rivkin, A. S., Bus, S. J., and Tokunaga, A. T. (2010). Earth encounters as the origin of fresh surfaces on near-Earth asteroids. *Nature*, 463:331–334.

Binzel, R. P., Rivkin, A. S., Stuart, J. S., Harris, A. W., Bus, S. J., and Burbine, T. H. (2004). Observed spectral properties of near-Earth objects: Results for population distribution, source regions, and space weathering processes. *Icarus*, 170(2):259–294.

Bottke, W. F., Durda, D. D., Nesvorný, D., Jedicke, R., Morbidelli, A., Vokrouhlický, D., and Levison, H. (2005). The fossilized size distribution of the main asteroid belt. *Icarus*, 175(1):111–140.

Bottke, W. F., Morbidelli, A., Jedicke, R., Petit, J.-M., Levison, H. F., Michel, P., and Metcalfe, T. S. (2002). Debiased orbital and absolute magnitude sistribution of the near-Earth objects. *Icarus*, 156:399–433.

Bottke, W. F., Vokrouhlický, D., Rubincam, D. P., and Nesvorný, D. (2006). The Yarkovsky and YORP : Implications for asteroid dynamics. *Annual Review of Earth and Planetary Sciences*, 34(1):157–191.

Bottke, W. F., Vokrouhlický, D., Walsh, K. J., Delbo, M., Michel, P., Lauretta, D. S., Campins, H., Connolly, H. C., Scheeres, D. J., and Chelsey, S. R. (2015). In search of the source of asteroid (101955) Bennu: Applications of the stochastic YORP model. *Icarus*, 247:191–217.

Brunetto, R., Loeffler, M. J., Nesvorný, D., Sasaki, S., and Strazzulla, G. (2015). Asteroid surface alteration by space weathering processes. *Asteroids IV*, pages 597–616.

Brunetto, R. and Strazzulla, G. (2005). Elastic collisions in ion irradiation experiments: A mechanism for space weathering of silicates. *Icarus*, 179(1):265–273.

Brunetto, R., Vernazza, P., Marchi, S., Birlan, M., Fulchignoni, M., Orofino, V., and Strazzulla, G. (2006). Modeling asteroid surfaces from observations and irradiation experiments: The case of 832 Karin. *Icarus*, 184(2):327–337.

Burbine, T. H., McCoy, T. J., Meibom, A., Gladman, B., and Keil, K. (2002). Meteoritic Parent Bodies: Their Number and Identification. *Asteroids III*, pages 653–667.

Bus, S. J. (1999). Compositional structure in the asteroid belt: results of a spectroscopic survey. *PhD thesis. Massachussetts Institute of Technology, Cambridge, MA.*

Bus, S. J. and Binzel, R. (2002). Phase II of the Small Main-Belt Asteroid Spectroscopic Survey A Feature-Based Taxonomy. *Icarus*, 158(1):146–177.

Čapek, D. and Vokrouhlický, D. (2004). The YORP effect with finite thermal conductivity. *Icarus*, 172(2):526–536.

Carry, B. (2012). Density of asteroids. *Planetary and Space Science*, 73(1):98–118.

Carry, B., Solano, E., Eggl, S., and DeMeo, F. (2016). Spectral properties of near-Earth and Mars-crossing asteroids using Sloan photometry. *Icarus*, 268:340–354.

Carvano, J. M., Hasselmann, P. H., Lazzaro, D., and Mothé-Diniz, T. (2010). SDSS-based taxonomic classification and orbital distribution of main belt asteroids. *Astronomy and Astrophysics*, 510:A43.

Chapman, C. R. (2004). Space Weathering of Asteroid Surfaces. *Annual Review of Earth and Planetary Sciences*, 32(1):539–567.

Chapman, C. R., Johnson, T. V., and McCord, T. B. (1971). A Review of Spectrophotometric Studies of Asteroids. *In: Gehrels, T. (Ed.), Physical Studies of Minor Planets. IAU Colloq.*, 267:51–65.

Chapman, R. (1996). S-type asteroids, ordinary chondrites, and space weathering: The evidence from Galileo's fly-bys of Gaspra and Ida. *Meteoritics and Planetary Science*, 31:699–725.

Clark, B. E., Hapke, B., Pieters, C., and Britt, D. (2002). Asteroid space weathering and regolith evolution. *Asteroids III*, pages 585–599.

Cotto-Figueroa, D., Statler, T. S., Richardson, D. C., and Tanga, P. (2015). Coupled spin and shape evolution of small rubble-pile asteroids: Self-limitation of the YORP effect. *The Astrophysical Journal*, 803(1):25.

Ćuk, M. and Burns, J. A. (2005). Effects of thermal radiation on the dynamics of binary NEAs. *Icarus*, 176:418–431.

Delbo, M., Libourel, G., Wilkerson, J., Murdoch, N., Michel, P., Ramesh, K. T., Ganino, C., Verati, C., and Marchi, S. (2014). Thermal fatigue as the origin of regolith on small asteroids. *Nature*, 508(7495):233–6.

DeMeo, F. and Carry, B. (2013). The taxonomic distribution of asteroids from multi-filter all-sky photometric surveys. *Icarus*, 226(1):723–741.

DeMeo, F. E., Binzel, R. P., and Lockhart, M. (2014). Mars encounters cause fresh surfaces on some near-Earth asteroids. *Icarus*, 227:112–122.

DeMeo, F. E., Binzel, R. P., Slivan, S. M., and Bus, S. J. (2009). An extension of the Bus asteroid taxonomy into the near-infrared. *Icarus*, 202(1):160–180.

Dohnanyi, J. S. (1969). Collisional Model of Asteroids and Their Debris. *J. Geophys. Res.*, 74:2531–2554.

Dombard, A. J., Barnouin, O. S., Prockter, L. M., and Thomas, P. C. (2010). Boulders and ponds on the asteroid 433 Eros. *Icarus*, 210(2):713–721.

Drummond, J. D. (1981). A test of comet and meteor shower associations. *Icarus*, 45:545–553.

Dykhuis, M. J., Molnar, L., Van Kooten, S. J., and Greenberg, R. (2014). Defining the Flora Family: Orbital properties, reflectance properties and age. *Icarus*, 243:111–128.

Eppes, M. C., Magi, B., Hallet, B., Delmelle, E., Mackenzie-Helnwein, P., Warren, K., and Swami, S. (2016). Deciphering the role of solar-induced thermal stresses in rock weathering. *Geological Society of America Bulletin*, 128(9-10):1315–1338.

Gaffey, M. (1993). Mineralogical variations within the S-type asteroid class. *Icarus*, 106(2):573–602.

Gaffey, M. J. (1976). Spectral reflectance characteristics of the meteorite classes. *Journal of Geophysical Research*, 81:905–920.

Gladman, B. (2000). The Near-Earth Object Population. *Icarus*, 146(1):176–189.

Gladman, B. J., Davis, D. R., Neese, C., Jedicke, R., Williams, G., Kavelaars, J. J., Petit, J.-M., Scholl, H., Holman, M., Warrington, B., Esquerdo, G., and Tricarico, P. (2009). On the asteroid belt's orbital and size distribution. *Icarus*, 202:104–118.

Golubov, O. and Krugly, Y. N. (2012). Tangential Component of the YORP Effect. *The Astrophysical Journal*, 752(1):L11.

Granvik, M., Morbidelli, A., Jedicke, R., Bolin, B., Bottke, W. F., Beshore, E., Vokrouhlický, D., Delbò, M., and Michel, P. (2016). Super-catastrophic disruption of asteroids at small perihelion distances. *Nature*, 530(7590):303–306.

Granvik, M., Morbidelli, A., Jedicke, R., Bolin, B., Bottke, W. F., Beshore, E., Vokrouhlický, D., Nesvorný, D., and Michel, P. (2018). Debiased orbit and absolute-magnitude distributions for near-Earth objects. *Icarus*, 312:181–207.

Graves, K. J., Minton, D. A., Hirabayashi, M., DeMeo, F. E., and Carry, B. (2018). Resurfacing asteroids from YORP spin-up and failure. *Icarus*, 304:162–171.

Hanuš, J., Ďurech, J., Brož, M., Warner, B. D., Pilcher, F., Stephens, R., Oey, J., Bernasconi, L., Casulli, S., Behrend, R., Polishook, D., Henych, T., Lehký, M., Yoshida, F., and Ito, T. (2011). A study of asteroid pole-latitude distribution based on an extended set of shape models derived by the lightcurve inversion method. *Astronomy & Astrophysics*, 530:A134.

Hapke, B. (2001). Space weathering from Mercury to the asteroid belt. *Journal of Geophysical Research*, 106:10039–10074.

Hapke, B., Cassidy, W., and Wells, E. (1975). Effects of vapor-phase deposition processes on the optical, chemical, and magnetic properties of the lunar regolith. *Moon*, 13:339–353.

Hazeli, K., El Mir, C., Papanikolaou, S., Delbo, M., and Ramesh, K. T. (2018). The origins of Asteroidal rock disaggregation: Interplay of thermal fatigue and microstructure. *Icarus*, 304:172–182.

Hirabayashi, M. (2015). Failure modes and conditions of a cohesive, spherical body due to YORP spin-up. *Monthly Notices of the Royal Astronomical Society*, 454(2):2249–2257.

Hirabayashi, M. and Scheeres, D. J. (2015). Stress and Failure Analysis of Rapidly Rotating Asteroid (29075) 1950 DA. *Astrophys. J. Letters*, 798:L8.

Hirayama, K. (1918). Groups of asteroids probably of common origin. *Astronomical Journal*, 31:185–188.

Ishiguro, M., Hiroi, T., Tholen, D. J., Sasaki, S., Ueda, Y., Nimura, T., Abe, M., Clark, B. E., Yamamoto, A., Yoshida, F., Nakamura, R., Hirata, N., Miyamoto, H., Yokota, Y., Hashimoto, T., Kubota, T., Nakamura, A. M., Gaskell, R. W., and Saito, J. (2007). Global mapping of the degree of space weathering on asteroid 25143 Itokawa by Hayabusa/AMICA observations. *Meteoritics & Planetary Science*, 42(10):1791–1800.

Ivezić, Ž., Tabachnik, S., Rafikov, R., Lupton, R. H., Quinn, T., Hammergren, M., Eyer, L., Chu, J., Armstrong, J. C., Fan, X., Finlator, K., Geballe, T. R., Gunn, J. E., Hennessy, G. S., Knapp, G. R., Leggett, S. K., Munn, J. A., Pier, J. R., Rockosi, C. M., Schneider, D. P., Strauss, M. A., Yanny, B., Brinkmann, J., Csabai, I., Hindsley, R. B., Kent, S., Lamb, D. Q., Margon, B., McKay, T. A., Smith, J. A.,

Waddell, P., and York, D. G. (2001). Solar system objects observed in the Sloan Digital Sky Survey commissioning data. *The Astronomical Journal*, 122(5):2749–2784.

Jacobson, S. A., Marzari, F., Rossi, A., and Scheeres, D. J. (2016). Matching asteroid population characteristics with a model constructed from the YORP-induced rotational fission hypothesis. *Icarus*, 277:381–394.

Jacobson, S. A., Marzari, F., Rossi, A., Scheeres, D. J., and Davis, D. R. (2014). Effect of rotational disruption on the size-frequency distribution of the Main Belt asteroid population. *Monthly Notices of the Royal Astronomical Society: Letters*, 439(1):L95–L99.

Jacobson, S. a. and Morbidelli, A. (2014). Lunar and Terrestrial Planet Formation in the Grand Tack Scenario. *Proceedings of the Royal Society*.

Jacobson, S. a. and Scheeres, D. J. (2011). Dynamics of rotationally fissioned asteroids: Source of observed small asteroid systems. *Icarus*, 214(1):161–178.

Janssen, M., Zuidema, J., and Wanhill, R. J. H. (2002). *Fracture Mechanics*. Delft University Press.

Jewitt, D. (2012). The Active Asteroids. *The Astronomical Journal*, 143:66.

Jewitt, D. (2013). Properties of Near-Sun Asteroids. *The Astronomical Journal*, 145:133.

Jewitt, D., Hsieh, H., and Agarwal, J. (2015). The active asteroids. *Asteroids IV*, pages 221–241.

Jewitt, D. and Li, J. (2010). Activity in Geminid Parent (3200) Phaethon. *The Astronomical Journal*, 140:1519–1527.

Jopek, T. J. (1993). Remarks on the meteor orbital similarity D-criterion. *Icarus*, 106:603.

Jopek, T. J., Rudawska, R., and Bartczak, P. (2008). Meteoroid Stream Searching: The Use of the Vectorial Elements. *Earth Moon and Planets*, 102:73–78.

Kaasalainen, M., urech, J., Warner, B. D., Krugly, Y. N., and Gaftonyuk, N. M. (2007). Acceleration of the rotation of asteroid 1862 Apollo by radiation torques. *Nature*, 446(7134):420–422.

Keil, K. (2000). Thermal alteration of asteroids: evidence from meteorites. *Planetary and Space Science*, 48:887–903.

Keller, L. P. and Berger, E. L. (2014). A transmission electron microscope study of Itokawa regolith grains. *Earth, Planets, and Space*, 66:71.

Kitamura, M. (1959). Photoelectric Study of Colors of Asteroids and Meteorites. *Publications of the Astronomical Society of Japan*, 11:79.

Lazzarin, M., Marchi, S., Barucci, M., Di Martino, M., and Barbieri, C. (2004). Visible and near-infrared spectroscopic investigation of near-Earth objects at ESO: first results. *Icarus*, 169(2):373–384.

Lazzarin, M., Marchi, S., Magrin, S., and Licandro, J. (2005). Spectroscopic investigation of near-Earth objects at Telescopio Nazionale Galileo. *Monthly Notices of the Royal Astronomical Society*, 359(4):1575–1582.

Le, J., Manning, J., and Labuz, J. F. (2014). Scaling of fatigue crack growth in rock. *International Journal of Rock Mechanics and Mining Sciences*, 72:71–79.

Levison, H. F. and Duncan, M. J. (1994). The long-term dynamical behavior of short-period comets. *Icarus*, 108:18–36.

Li, J. and Jewitt, D. (2013). Recurrent Perihelion Activity in (3200) Phaethon. *The Astronomical Journal*, 145:154.

Lin, H., Yoshida, F., Chen, Y., Ip, W., and Chang, C. (2015). A search for subkilometer-sized ordinary chondrite like asteroids in the main-belt. *Icarus*, 254:202–212.

Loeffler, M. J., Dukes, C. A., and Baragiola, R. A. (2009). Irradiation of olivine by 4 keV He + : Simulation of space weathering by the solar wind. *Journal of Geophysical Research*, 114(E3).

Lowry, S. C., Fitzsimmons, A., Pravec, P., Vokrouhlický, D., Boehnhardt, H., Taylor, P. A., Margot, J.-L., Galád, A., Irwin, M., Irwin, J., and Kusnirák, P. (2007). Direct Detection of the Asteroidal YORP Effect. *Science*, 316(5822).

Marchi, S., Brunetto, R., Magrin, S., Lazzarin, M., and Gandolfi, D. (2005). Space weathering of near-Earth and main belt silicate-rich asteroids: observations and ion irradiation experiments. *Astronomy and Astrophysics*, 443(3):769–775.

Marchi, S., Delbo, M., Morbidelli, A., Paolicchi, P., and Lazzarin, M. (2009). Heating of near-Earth objects and meteoroids due to close approaches to the Sun. *Monthly Notices of the Royal Astronomical Society*, 400:147–153.

Marchi, S., Magrin, S., Nesvorny, D., Paolicchi, P., and Lazzarin, M. (2006a). A spectral slope versus perihelion distance correlation for planet-crossing asteroids. *Monthly Notices of the Royal Astronomical Society: Letters*, 368(1):L39–L42.

Marchi, S., Paolicchi, P., Lazzarin, M., and Magrin, S. (2006b). A General Spectral Slope-Exposure Relation for S-Type Main Belt and Near-Earth Asteroids. *The Astronomical Journal*, 131(2):1138–1141.

Marchi, S., Paolicchi, P., and Richardson, D. C. (2012). Collisional evolution and reddening of asteroid surfaces - I. The problem of conflicting time-scales and the role of size-dependent effects. *Monthly Notices of the Royal Astronomical Society*, 421(1).

Marzari, F., Rossi, A., and Scheeres, D. (2011). Combined effect of YORP and collisions on the rotation rate of small Main Belt asteroids. *Icarus*, 214(2):622–631.

Masiero, J. R., Mainzer, A. K., Grav, T., Bauer, J. M., Cutri, R. M., Dailey, J., Eisenhardt, P. R. M., McMillan, R. S., Spahr, T. B., Skrutskie, M. F., Tholen, D., Walker, R. G., Wright, E. L., DeBaun, E., Elsbury, D., Gautier, IV, T., Gomillion, S., and Wilkins, A. (2011). Main Belt Asteroids with WISE/NEOWISE. I. Preliminary Albedos and Diameters. *The Astrophysical Journal*, 741:68.

Michikami, T., Kadokawa, T., Tsuchiyama, A., Hagermann, A., Nakano, T., Uesugi, K., and Hasegawa, S. (2018). Influence of petrographic textures on the shapes of impact experiment fine fragments measuring several tens of microns: Comparison with Itokawa regolith particles. *Icarus*, 302:109–125.

Michikami, T., Nakamura, A. M., and Hirata, N. (2010). The shape distribution of boulders on Asteroid 25143 Itokawa: Comparison with fragments from impact experiments. *Icarus*, 207:277–284.

Migliazza, M., Ferrero, A. M., and Spagnoli, A. (2011). Experimental investigation on crack propagation in carrara marble subjected to cyclic loads. *International Journal of Rock Mechanics and Mining Sciences*, 48(6):1038–1044.

Molaro, J. L., Byrne, S., and Langer, S. A. (2015). Grain-scale thermoelastic stresses and spatiotemporal temperature gradients on airless bodies, implications for rock breakdown. *Journal of Geophysical Research: Planets*, 120(2):255–277.

Molaro, J. L., Byrne, S., and Le, J.-L. (2017). Thermally induced stresses in boulders on airless body surfaces, and implications for rock breakdown. *Icarus*, 294:247–261.

Morbidelli, A. and Gladman, B. (1998). Orbital and temporal distributions of meteorites originating in the asteroid belt. *Meteoritics and Planetary Science*, 33:999–1016.

Morbidelli, A. and Nesvorný, D. (1999). Numerous Weak Resonances Drive Asteroids toward Terrestrial Planets Orbits. *Icarus*, 308:295–308.

Mothé-Diniz, T., Jasmin, F. L., Carvano, J. M., Lazzaro, D., Nesvorný, D., and Ramirez, a. C. (2010). Re-assessing the ordinary chondrites paradox. *Astronomy and Astrophysics*, 514:A86.

Mothé-Diniz, T. and Nesvorný, D. (2008). Visible spectroscopy of extremely young asteroid families. *Astronomy and Astrophysics*, 486(2):L9–L12.

Nakamura, T., Noguchi, T., Tanaka, M., Zolensky, M. E., Kimura, M., Tsuchiyama, A., Nakato, A., Ogami, T., Ishida, H., Uesugi, M., Yada, T., Shirai, K., Fujimura, A., Okazaki, R., Sandford, S. A., Ishibashi, Y., Abe, M., Okada, T., Ueno, M., Mukai, T., Yoshikawa, M., and Kawaguchi, J. (2011). Itokawa Dust Particles: A Direct Link Between S-Type Asteroids and Ordinary Chondrites. *Science*, 333:1113.

Nesvorný, D., Bottke, W. F., Vokrouhlický, D., Chapman, C. R., and Rafkin, S. (2010). Do planetary encounters reset surfaces of near Earth asteroids? *Icarus*, 209(2):510–519.

Nesvorný, D., Brož, M., and Carruba, V. (2015). Identification and Dynamical Properties of Asteroid Families. *Asteroids IV*, pages 297–321.

Nesvorný, D., Jedicke, R., Whiteley, R. J., and Ivezić, Ž. (2005). Evidence for asteroid space weathering from the Sloan Digital Sky Survey. *Icarus*, 173(1):132–152.

Nesvorný, D. and Vokrouhlický, D. (2006). New Candidates for Recent Asteroid Breakups. *The Astrophysical Journal*, 132:1950–1958.

Noguchi, T., Nakamura, T., Kimura, M., Zolensky, M. E., Tanaka, M., Hashimoto, T., Konno, M., Nakato, A., Ogami, T., Fujimura, A., Abe, M., Yada, T., Mukai, T., Ueno, M., Okada, T., Shirai, K., Ishibashi, Y., and Okazaki, R. (2011). Incipient space weathering observed on the surface of Itokawa dust particles. *Science*, 333:1121.

Paolicchi, P., Marchi, S., Lazzarin, M., and Magrin, S. (2009). Collisional timing of asteroids space weathering: A first approach. *Planetary and Space Science*, 57:216–220.

Paris, P. and Erdogan, F. (1963). A critical analysis of crack propagation laws. *Journal of Basic Engineering*, 85(4):528–533.

Polishook, D. and Brosch, N. (2009). Photometry and spin rate distribution of small-sized main belt asteroids. *Icarus*, 199:319–332.

Polishook, D., Moskovitz, N., Binzel, R. P., DeMeo, F. E., Vokrouhlický, D., Žižka, J., and Oszkiewicz, D. (2014). Observations of "fresh" and weathered surfaces on asteroid pairs and their implications on the rotational-fission mechanism. *Icarus*, 233:9–26.

Polishook, D., Moskovitz, N., DeMeo, F. E., and Binzel, R. P. (2014). Rotationally resolved spectroscopy of asteroid pairs: No spectral variation suggests fission is followed by settling of dust. *Icarus*, 243:222–235.

Pravec, P. and Harris, A. (2007). Binary asteroid population. *Icarus*, 190(1):250–259.

Pravec, P. and Vokrouhlický, D. (2009). Significance analysis of asteroid pairs. *Icarus*, 204:580–588.

Pravec, P., Vokrouhlický, D., Polishook, D., Scheeres, D. J., Harris, A. W., Galád, A., Vaduvescu, O., Pozo, F., Barr, A., Longa, P., Vachier, F., Colas, F., Pray, D. P., Pollock, J., Reichart, D., Ivarsen, K., Haislip, J., Lacluyze, A., Kusnirák, P., Henych, T., Marchis, F., Macomber, B., Jacobson, S. A., Krugly, Y. N., Sergeev, A. V., and Leroy, A. (2010). Formation of asteroid pairs by rotational fission. *Nature*, 466(7310):1085–8.

Pravec, P. and W., H. A. (2000). Fast and Slow Rotation of Asteroids. *Icarus*, 148(1):12–20.

Rabinowitz, D. L. (1994). The size and shape of the near-Earth asteroid belt. *Icarus*, 111:364–377.

Reddy, V., Dunn, T. L., Thomas, C. A., Moskovitz, N. A., and Burbine, T. H. (2015). Mineralogy and surface composition of asteroids. *Asteroids IV*, pages 43–63.

Richardson, D. (1998). Tidal Distortion and Disruption of Earth-Crossing Asteroids. *Icarus*, 134(1):47–76.

Richardson, J. E., Graves, K. J., and Bowling, T. J. (2018). Small body shapes and spins reveal a prevailing state of maximum surface stability. *Icarus (submitted for publication.*

Richardson, J. E., Melosh, H. J., Greenberg, R. J., and O'Brien, D. P. (2005). The global effects of impact-induced seismic activity on fractured asteroid surface morphology. *Icarus*, 179(2):325–349.

Ritchie, R. (2005). Incomplete self-similarity and fatigue-crack growth. *International Journal of Fracture*, 132(3):197–203.

Rivkin, A. S., Thomas, C. A., Trilling, D. E., Enga, M.-t., and Grier, J. A. (2011). Ordinary chondrite-like colors in small Koronis family members. *Icarus*, 211:1294–1297.

Rossi, a., Marzari, F., and Scheeres, D. J. (2009). Computing the effects of YORP on the spin rate distribution of the NEO population. *Icarus*, 202(1):95–103.

Rożek, A., Breiter, S., and Jopek, T. J. (2011). Orbital similarity functions - application to asteroid pairs. *Monthly Notices of the Royal Astronomical Society*, 412:987–994.

Rubincam, D. P. (2000). Radiative Spin-up and Spin-down of Small Asteroids. *Icarus*, 148(1):2–11.

Sasaki, S., Hiroi, T., Nakamura, K., Hamabe, Y., Kurahashi, E., and Yamada, M. (2002). Simulation Of Space Weathering By Nanosecond Pulse Laser Heating: Dependence On Mineral Composition, Weathering Trend Of Asteroids And Discovery Of Nanophase Iron Particles. *Adv. Space Res.*, 29(5):7–3.

Sasaki, S., Nakamura, K., Hamabe, Y., Kurahashi, E., and Hiroi, T. (2001). Production of iron nanoparticles by laser irradiation in a simulation of lunar-like space weathering. *Nature*, 410(6828):555–7.

Scheeres, D. (2007). The dynamical evolution of uniformly rotating asteroids subject to YORP. *Icarus*, 188(2):430–450.

Schunová, E., Granvik, M., Jedicke, R., Gronchi, G., Wainscoat, R., and Abe, S. (2012). Searching for the first near-Earth object family. *Icarus*, 220:1050–1063.

Shestopalov, D., Golubeva, L., and Cloutis, E. (2013). Optical maturation of asteroid surfaces. *Icarus*, 225(1):781–793.

Southworth, R. B. and Hawkins, G. S. (1963). Statistics of meteor streams. *Smithsonian Contributions to Astrophysics*, 7:261.

Statler, T. S. (2009). Extreme sensitivity of the YORP effect to small-scale topography. *Icarus*, 202(2):502–513.

Steckloff, J. K. and Jacobson, S. A. (2016). The formation of striae within cometary dust tails by a sublimation-driven YORP-like effect. *Icarus*, 264:160–171.

Strazzulla, G., Dotto, E., Binzel, R., Brunetto, R., Barucci, M. A., Blanco, A., and Orofino, V. (2005). Spectral alteration of the Meteorite Epinal (H5) induced by heavy ion irradiation: a simulation of space weathering effects on near-Earth asteroids. *Icarus*, 174(1):31–35.

Taylor, P. A., Margot, J.-L., Vokrouhlicky, D., Scheeres, D. J., Pravec, P., Lowry, S. C., Fitzsimmons, A., Nolan, M. C., Ostro, S. J., Benner, L. A. M., Giorgini,

J. D., and Magri, C. (2007). Spin rate of asteroid (54509) 2000 PH5 increasing due to the YORP effect. *Science (New York, N.Y.)*, 316(5822):274–277.

Thirumalai, K. and Demou, S. G. (1970). Effect of Reduced Pressure on ThermalExpansion Behavior of Rocks and Its Significance to Thermal Fragmentation. *Journal of Applied Physics*, 41(13):5147–5151.

Tholen, D. J. (1984). Asteroid Taxonomy From Cluster Analysis of Photometry. *The University of Arizona.*

Thomas, C. A., Rivkin, A. S., Trilling, D. E., and Grier, J. A. (2011). Space weathering of small Koronis family members. *Icarus*, 212(1):158–166.

Thomas, C. A., Trilling, D. E., and Rivkin, A. S. (2012). Space weathering of small Koronis family asteroids in the SDSS Moving Object Catalog. *Icarus*, 219(1):505–507.

Tsuchiyama, A., Uesugi, M., Matsushima, T., Michikami, T., Kadono, T., Nakamura, T., Uesugi, K., Nakano, T., Sandford, S. a., Noguchi, R., Matsumoto, T., Matsuno, J., Nagano, T., Imai, Y., Takeuchi, A., Suzuki, Y., Ogami, T., Katagiri, J., Ebihara, M., Ireland, T. R., Kitajima, F., Nagao, K., Naraoka, H., Noguchi, T., Okazaki, R., Yurimoto, H., Zolensky, M. E., Mukai, T., Abe, M., Yada, T., Fujimura, A., Yoshikawa, M., and Kawaguchi, J. (2011). Three-dimensional structure of Hayabusa samples: origin and evolution of Itokawa regolith. *Science (New York, N.Y.)*, 333(6046):1125–1128.

Vernazza, P., Binzel, R. P., Rossi, A., Fulchignoni, M., and Birlan, M. (2009). Solar wind as the origin of rapid reddening of asteroid surfaces. *Nature*, 458(7241):993–5.

Viles, H., Ehlmann, B., Wilson, C. F., Cebula, T., Page, M., and Bourke, M. (2010). Simulating weathering of basalt on Mars and Earth by thermal cycling. *Geophysical Research Letters*, 37:L18201.

Vokrouhlický, D., Bottke, W. F., Chesley, S. R., Scheeres, D. J., and Statler, T. S. (2015). The yarkovsky and yorp effects. *Asteroids IV*, pages 509–531.

Vokrouhlický, D., Breiter, S., Nesvorný, D., and Bottke, W. F. (2007). Generalized YORP evolution: Onset of tumbling and new asymptotic states. *Icarus*, 191:636–650.

Vokrouhlický, D. and Nesvorný, D. (2008). Pairs of Asteroids Probably of a Common Origin. *The Astronomical Journal*, 136:280–290.

Vokrouhlický, D. and Nesvorný, D. (2009). The Common Roots of Asteroids (6070) Rheinland and (54827) 2001 NQ8. *The Astronomical Journal*, 137:111–117.

Vokrouhlický, D. and Čapek, D. (2002). YORP-Induced Long-Term Evolution of the Spin State of Small Asteroids and Meteoroids: Rubincam's Approximation. *Icarus*, 159:449–467.

Walsh, K. J. and Jacobson, S. A. (2015). Formation and Evolution of Binary Asteroids. *Asteroids IV*, pages 375–393.

Walsh, K. J. and Richardson, D. C. (2008). A steady-state model of NEA binaries formed by tidal disruption of gravitational aggregates. *Icarus*, 193(2):553–566.

Walsh, K. J., Richardson, D. C., and Michel, P. (2008). Rotational breakup as the origin of small binary asteroids. *Nature*, 454:188–191.

Walsh, K. J., Richardson, D. C., and Michel, P. (2008). Rotational breakup as the origin of small binary asteroids. *Nature*, 454(7201):188–91.

Watson, F. G. (1938). Reflectivity and color of meteorites. *Proceedings of the National Academy of Sciences*, 24(12):532–537.

Willman, M. and Jedicke, R. (2011). Asteroid age distributions determined by space weathering and collisional evolution models. *Icarus*, 211(1):504–510.

Willman, M., Jedicke, R., Moskovitz, N., Nesvorný, D., Vokrouhlický, D., and Mothé-Diniz, T. (2010). Using the youngest asteroid clusters to constrain the space weathering and gardening rate on S-complex asteroids. *Icarus*, 208:758–772.

Willman, M., Jedicke, R., Nesvorný, D., Moskovitz, N., Ivezić, Ž., and Fevig, R. (2008). Redetermination of the space weathering rate using spectra of Iannini asteroid family members. *Icarus*, 195(2):663–673.

Wood, X. H. J. and Kuiper, G. P. (1963). Photometric Studies of Asteroids. *The Astrophysical Journal*, 137:1279.

Xu, S., Binzel, R. P., Burbine, T. H., and Bus, S. J. (1995). Small main-belt asteroid spectroscopic survey: Initial results. *Icarus*, 115:1–35.

York, D. G., Adelman, J., Anderson, Jr., J. E., Anderson, S. F., Annis, J., Bahcall, N. A., Bakken, J. A., Barkhouser, R., Bastian, S., Berman, E., Boroski, W. N., Bracker, S., Briegel, C., Briggs, J. W., Brinkmann, J., Brunner, R., Burles, S., Carey, L., Carr, M. A., Castander, F. J., Chen, B., Colestock, P. L., Connolly, A. J., Crocker, J. H., Csabai, I., Czarapata, P. C., Davis, J. E., Doi, M., Dombeck, T., Eisenstein, D., Ellman, N., Elms, B. R., Evans, M. L., Fan, X., Federwitz, G. R., Fiscelli, L., Friedman, S., Frieman, J. A., Fukugita, M., Gillespie, B., Gunn, J. E., Gurbani, V. K., de Haas, E., Haldeman, M., Harris, F. H., Hayes, J., Heckman, T. M., Hennessy, G. S., Hindsley, R. B., Holm, S., Holmgren, D. J., Huang, C.-h., Hull, C., Husby, D., Ichikawa, S.-I., Ichikawa, T., Ivezić, Ž., Kent, S., Kim, R. S. J., Kinney, E., Klaene, M., Kleinman, A. N., Kleinman, S., Knapp, G. R., Korienek, J., Kron, R. G., Kunszt, P. Z., Lamb, D. Q., Lee, B., Leger, R. F., Limmongkol, S., Lindenmeyer, C., Long, D. C., Loomis, C., Loveday, J., Lucinio, R., Lupton, R. H., MacKinnon, B., Mannery, E. J., Mantsch, P. M., Margon, B., McGehee, P., McKay, T. A., Meiksin, A., Merelli, A., Monet, D. G., Munn, J. A., Narayanan, V. K., Nash, T., Neilsen, E., Neswold, R., Newberg, H. J., Nichol, R. C., Nicinski, T., Nonino, M., Okada, N., Okamura, S., Ostriker, J. P., Owen,

R., Pauls, A. G., Peoples, J., Peterson, R. L., Petravick, D., Pier, J. R., Pope, A., Pordes, R., Prosapio, A., Rechenmacher, R., Quinn, T. R., Richards, G. T., Richmond, M. W., Rivetta, C. H., Rockosi, C. M., Ruthmansdorfer, K., Sandford, D., Schlegel, D. J., Schneider, D. P., Sekiguchi, M., Sergey, G., Shimasaku, K., Siegmund, W. A., Smee, S., Smith, J. A., Snedden, S., Stone, R., Stoughton, C., Strauss, M. A., Stubbs, C., SubbaRao, M., Szalay, A. S., Szapudi, I., Szokoly, G. P., Thakar, A. R., Tremonti, C., Tucker, D. L., Uomoto, A., Vanden Berk, D., Vogeley, M. S., Waddell, P., Wang, S.-i., Watanabe, M., Weinberg, D. H., Yanny, B., and Yasuda, N. (2000). The Sloan Digital Sky Survey: Technical Summary. *The Astronomical Journal*, 120(3):1579–1587.

Zappala, V., Cellino, A., Farinella, P., and Knezevic, Z. (1990). Asteroid families. I - Identification by hierarchical clustering and reliability assessment. *The Astrophysical Journal*, 100:2030–2046.

Zellner, B., Tholen, D. J., and Tedesco, E. F. (1985). The eight-color asteroid survey - Results for 589 minor planets. *Icarus*, 61:355–416.